THE PURSUIT OF AN IDEAL COORDINATION ENVIRONMENT OF THE CATALYTIC SITE FOR WATER SPLITTING

A THESIS SUBMITTED TO

THE GRADUATE SCHOOL OF ENGINEERING AND SCIENCE OF

BILKENT UNIVERSITY

IN PARTIAL FULFILLMENT OF THE REQUIREMENTS FOR THE

DEGREE OF

MASTER OF SCIENCE IN

CHEMISTRY

By

Aliyu Aremu AHMAD

July 2022

THE PURSUIT OF AN IDEAL COORDINATION ENVIRONMENT OF THE CATALYTIC SITE FOR WATER SPLITTING

By Aliyu Aremu AHMAD

July 2022

We certify that we have read this thesis and that in our opinion it is fully adequate, in scope and in quality, as a thesis for the degree of Master of Science.

_____

Ferdi Karadaş (Advisor)

_____

Ömer Dağ

_____

Murielle Chavarot-Kerlidou

Approved for the Graduate School of Engineering and Science:

_____

Orhan Arıkan

Director of the Graduate School

ABSTRACT

THE PURSUIT OF AN IDEAL COORDINATION ENVIRONMENT OF THE CATALYTIC SITE FOR WATER SPLITTING

Aliyu Aremu AHMAD

M.S. in Chemistry

Advisor: Ferdi Karadaş

July 2022

The construction of catalysts from cheap materials and exquisite tuning of the coordination environment of the active site is pivotal to the development of a highly active sustainable water-splitting catalyst. Although recent years have seen tremendous growth in the application of Prussian Blue Analogues (PBAs) as non-noble catalysts for water splitting, the effect of the structural coordination of the active sites on the activity of a Prussian blue (PB) catalyst is yet to be explored. Herein, using two simple synthetic strategies, we show that manipulating the coordination environment of the catalytic sites affects the morphology, electronic properties, and eventually the catalytic activity of PBAs. Moreover, this study mimics natural photosynthesis by using solar light as an energy source.

First, we demonstrate that the water oxidation activity and stability of a Co–Fe PBA can be tuned by coordinating bidentate capping ligands to the catalytic cobalt sites. Structural characterization studies reveal that the ligand decorated structures are of relatively lower dimensionality and they retained their network structures even after photocatalysis. Photocatalytic water oxidation studies indicate that coordination of one equivalent ligand group to the catalytic cobalt sites (CoL–Fe) results in an enhancement of about 50 times in upper-bound turnover frequency (TOF), while coordination of two equivalent ligand groups to the catalytic cobalt sites (CoL2–Fe) lead to an inactivity, which is attributed to the lack of coordination of water molecules to the catalytic sites. In addition, computational studies support experimental observation by showing that bidentate pyridyl groups enhance the susceptibility of the rate-determining Co(IV)-oxo species to the nucleophilic water attack during the critical O−O bond formation.

We found in the second study that the replacement of $[Fe(CN)_6]^{3-}$ unit with a square planar $[Ni(CN)_4]^{2-}$ building block drastically changes the electronic environment and catalytic properties

by converting the PB structure from 3D to a 2D layered structure, and we utilized it for the first time for photocatalytic hydrogen evolution reaction. We synthesized a 2D cyanide-coordination compound **[Co–Ni]** and performed a complete structural and morphological characterization that fully supports our synthetic claim. Relying on its exposed facets, layered morphology, and abundant surface-active sites, **[Co–Ni]** can efficiently convert water and sunlight to H_2 in the presence of a ruthenium photosensitizer with an optimal evolution rate of 30,029 μmol g^{-1} h^{-1}, greatly exceeding that of 3D PBA frameworks and top-ranked catalysts operating under the same condition. Furthermore, **[Co–Ni]** retains its structural integrity throughout a 6-hour photocatalytic cycle, which is confirmed by XPS, XRD and Infrared analysis.

Overall, these two strategies signify the importance of the coordination environment of the active sites in exploiting structure/morphology and optimizing the activity of the catalyst.

Keywords: water oxidation, hydrogen evolution, Prussian blue analogues, ligand-engineered, photocatalysis, catalysis, 2-dimensional cyanide compounds, coordination, bidentate pyridyl ligand, active site.

ÖZET

SU AYRIMI IÇIN KATALITIK SAHANIN IDEAL BIR KOORDINASYON ORTAMININ ARIŞI

Aliyu Aremu AHMAD

Kimya, Yüksek Lisans

Tez Danışmanı: Ferdi Karadaş

Temmuz 2022

Katalizörlerin ucuz malzemelerden yapımı ve aktif metal merkezinin koordinasyon ortamının tasarımı, oldukça aktif ve sürdürülebilir bir katalizörün geliştirilmesi suyun ayrıştırılması işlemi için çok önemlidir. Son yıllarda, Prusya Mavisi Analoglarının (PBA) suyun ayrıştırılmasında kullanan doğada bol bulunan yapıtaşlarından oluşan katalizörler olarak kullanılmasında muazzam bir yol katedilmiş olsa da, aktif bölgelerin yapısal koordinasyonunun bir Prusya mavisi (PB) katalizörünün aktivitesi üzerindeki etkisi henüz araştırılmamıştır. Bu tez çalışmasında, iki basit sentetik strateji kullanarak, katalitik bölgelerin koordinasyon ortamını manipüle etmenin morfolojiyi, elektronik özellikleri ve nihayetinde PBA'ların katalitik aktivitesini etkilediğini gösteriyoruz. Dahası, bu çalışma güneş ışığını bir enerji kaynağı olarak kullanarak doğal fotosentezi taklit etmektedir.

İlk olarak, bir Co-Fe PBA'nın suyun yükseltgenmesi işlemindeki aktivitesinin ve stabilitesinin, iki dişli ligandları katalitik kobalt bölgelerine koordine ederek ayarlanabileceğini gösteriyoruz. Yapısal karakterizasyon çalışmaları, ligand süslü yapıların nispeten daha düşük boyutluluğa sahip olduğunu ve fotokatalizden sonra bile ağ yapılarını koruduklarını ortaya koymaktadır. Fotokatalitik çalışmalar, bir eşdeğer ligand grubunun katalitik kobalt bölgelerine (CoL-Fe) koordinasyonunun, üst sınır devir döngüsü katsayısında (TOF) yaklaşık 50 kat artışla sonuçlandığını, iki eşdeğer ligand grubunun katalitik kobalt bölgelerine (CoL2-Fe) koordinasyonunun, su moleküllerinin katalitik bölgelere koordinasyon eksikliğinden kaynaklanan bir aktivasyon yoksunluğuna yol açtığını göstermektedir. Ek olarak, hesaplamalı çalışmalar, iki dişli piridil gruplarının, kritik O-O bağ oluşumu sırasında hız belirleyici Co (IV)-okso türlerinin nükleofilik su saldırısına duyarlılığını arttırdığını göstererek deneysel gözlemi desteklemektedir.

İkinci çalışmada, $[Fe(CN)_6]^{3-}$ yapı taşının kare düzlemsel $[Ni(CN)_4]^{2-}$ yapı taşı ile değiştirilmesinin, PB yapısını 3D'den 2D katmanlı bir yapıya dönüştürerek elektronik ortamı ve katalitik özellikleri büyük ölçüde değiştirdiğini ve ilk kez fotokatalitik hidrojen oluşum tepkimesi için kullanılabileceğini gösterdik. İki boyutlu bir siyanür koordinasyon bileşiği [Co-Ni] sentezledik ve sentetik iddiamızı tam olarak destekleyen eksiksiz bir yapısal ve morfolojik karakterizasyon gerçekleştirdik. Maruz kalan boyutlarına, katmanlı morfolojisine ve bol miktarda yüzey aktif bölgelerine dayanarak, [Co-Ni], 3D PBA malzemelerini büyük ölçüde aşan, 30.029 $\mu mol\ g^{-1}\ h^{-1}$ optimal evrim hızına sahip bir rutenyum boyar madde varlığında suyu ve güneş ışığını verimli bir şekilde H_2'ye dönüştürebilir ve aynı koşulda çalışan en üst düzey katalizörlerle yarışabailecek performansa sahiptir. Ayrıca, [Co-Ni], XPS, XRD ve Infrared analizleri ile doğrulanan 6 saatlik bir fotokatalitik döngü boyunca yapısal bütünlüğünü korumaktadır.

Genel olarak, bu iki strateji, aktif bölgelerin koordinasyon ortamının yapı / morfolojiden yararlanma ve katalizörün aktivitesini optimize etmedeki önemini göstermektedir.

Anahtar Kelimeler: su oksidasyonu, hidrojen evrimi, Prusya mavisi analogları, ligand-mühendisliği, fotokataliz, kataliz, 2 boyutlu siyanür bileşikleri, koordinasyon, bidentat piridil ligand, aktif bölge.

"The superiority of the learned man

over the devout is like that of the moon,

on the night when it is full, over the rest of the stars."

Prophet Muhammad, PBUH.

ACKNOWLEDGEMENTS

My first gratitude goes to Almighty Allah, the Creator of the universe and the most Exalted, for guiding my path to Karadaş Lab at Bilkent University and bestowing me with the ability to carry out this research work. I reflect upon my life and realise how completely I am dependent on Allah for his immense favours on me, he is the most deserving of all my appreciation and praise.

I would like to express my great satisfaction and appreciation to my advisor, Professor Ferdi Karadaş. He guided and encouraged me through the completion of this research work and, at the same time, gave me the freedom to make my own decisions about the research progress. He is always there to help whenever I am stuck, improved my logical reasoning with his questions, and corrected my mistakes elegantly without destroying my confidence. He is positive, approachable, compassionate, and always available to discuss the progress of the research work, even after working hours. He provided timely feedback on my writings and presentations and great suggestions for improving myself. He is genuinely interested in seeing me succeed, and I have developed and learned a lot under his guidance. His qualities are rare to find, and I am deeply honoured that our paths crossed and will forever remember the time I have spent with you.

I thank my thesis committee members, Prof. Ömer Dağ and Dr. Murielle Chavarot-Kerlidou, for examining this thesis and providing valuable inputs to improve the quality. I would like to thank the Department of Chemistry at Bilkent University for finding me worthy of the graduate scholarship and other institutions that funded my research at Bilkent University. I am grateful to Dr. Burak Ülgüt for his support and help in writing recommendation letters for my PhD applications.

I am grateful to Muhammed Buyuktemiz and Prof. Yavuz Dede for collaborating with us and providing computations to support our experimental observations in one of the projects.

I thank Dr. Gamze Ulusoy Ghobadi for teaching me many aspects of research and providing support whenever I needed it. Her guidance and contribution to this work are greatly appreciated. I am grateful to Ramadan Chalil Oglou for being more than just a lab mate to me, being a friend, motivating me, and making the lab a lively environment for everyone. I thank Sina Sadigh Akbari and Dr. Sara Samuel for their indirect inputs to this work and for creating a positive working environment.

I sincerely appreciate my Parents, whom Allah has confined with a promise of guiding me to the right path, which they never failed. They have sacrificed a lot for me, supported me throughout my stay at Bilkent University and checked on me at all times. I thank you a lot, and I am indebted to fulfilling the assignment Allah has given me towards you. I also acknowledge Late Dr. Okeowo for supporting and sponsoring my foundational education.

I am thankful to Kamil Mohammed and Zakariah Musa for making it easy for me to transition into the new environment and helping me countless times throughout my time in Turkey. I am grateful to Arma Yau Musa, Abdus-Salam, Kayode Kate, Benjamin and for their assistance. I am grateful to my friends in Nigeria. I would like to thank Mr. Sulaimon Ajao, Mr. AbdulAzeez, and Sheikh Thakib for supporting my journey to Bilkent and for their continued guidance. I thank Dr. Abdullah Rajee and Dr. O.K. Yusuff for their advice, support and encouragement. I appreciate everyone who has supported me and this work in any way. Thank you all.

TABLE OF CONTENTS

CHAPTER 1

1.0 INTRODUCTION ……. 1

1.1 Photocatalytic (Solar) Water Splitting ……..... 1

1.2 Inspiration from Nature …… 3

1.2.1 Oxygen Evolving Complex (OEC) …… 4

1.3 Artificial Photosynthesis (Mimicking Natural Photosynthesis) …… 5

1.3.1 The Light Absorbing Component (Photosensitizer) …… 6

1.3.1.1 Ru(II) Photosensitizers …… 7

1.3.2 The Catalyst …… 8

1.3.2.1 The Water Oxidation Catalyst (WOC) …… 9

1.3.2.2 The Reduction or The Hydrogen Evolution Catalyst …… 11

1.4 Prussian Blue Analogues as Water Splitting Catalysts …… 12

1.4.1 Coordination Environment of PBAs for Water Splitting …… 14

1.4.2 PBAs for Photocatalytic Water Oxidation …… 14

1.4.3 PBAs for Photocatalytic Hydrogen Evolution …… 17

1.5 Thesis Objectives …… 18

CHAPTER 2

2.0 EXPERIMENTAL ……. 20

2.1 Chemicals and Reagents ……. 20

2.2 Synthesis of PBAs ……. 20

2.3 Synthesis of Cobalt Precursors ……. 21

2.4 Synthesis of Ligand-Engineered PBAs ……. 22

2.5 Instrumentation …….……. 23

2.5.1 Fourier Transform Infrared Spectroscopy (FTIR) ……. 23

2.5.2 UV-Vis Spectroscopy ……. 23

2.5.3 Diffuse-reflectance UV-Vis Spectroscopy ……. 23

2.5.4 Thermogravimetric Analysis (TGA) ……. 23

2.5.5 CHN Elemental Analysis ……. 23

2.5.6 X-ray Photoelectron Spectroscopy (XPS) …….…. 24

2.5.7 Powder X-ray Diffraction (PXRD) …… 24

2.5.8 Transmission Electron Microscopy (TEM) …… 24

2.5.9 Scanning Electron Microscopy (SEM) and Energy Dispersive X-ray (EDX) .. 24

2.6 Electrochemistry ……... 24

2.6.1 Electrochemical measurements ……..... 24

2.6.2 Working Electrode Preparation ……... 25

2.7 Photocatalysis …… 25

2.7.1 Photocatalytic OER experiment …… 25

2.7.2 Photocatalytic HER experiment …… 26

2.7.2.1 Cycle HER experiments …… 26

CHAPTER 3

3.0 LIGAND-ENGINEERED PRUSSIAN BLUE ANALOGUES FOR PHOTOCATALYTIC WATER OXIDATION ……..… 27

3.1 Preface ……..… 27

3.2 Introduction ……..… 28

3.3 Results and Discussions ……..… 28

3.3.1 Synthesis ……..…… 28

3.3.2 Catalysts Characterization ……..… 31

3.3.2.1 SEM-EDX ……. 31

3.3.2.2 TGA ……. 32

3.3.2.3 CHN elemental analysis ……. 33

3.3.2.4 FTIR ……..……. 34

3.3.2.5 XRD ……..…. 35

3.3.2.6 XPS ……..…. 37

3.3.3 Photocatalytic Water Oxidation ……..…. 38

3.3.4 Electrochemistry and Surface Area Analysis ……..……. 40

3.3.5 Post-Catalytic Characterization ……..…. 43

3.3.6 Electronic Structure Calculations ……..…. 46

CHAPTER 4

4.0 2D CYANIDE-BASED COORDINATION COMPOUND FOR PHOTOCATALYTIC HYDROGEN EVOLUTION …… 49

4.1 Preface ……. 49

4.2 Introduction ……. 50

4.3 Results and Discussions ……. 50

4.3.1 Synthesis ……..…… 50

4.3.2 Catalysts Characterization ……. 51

4.3.2.1 TEM ……. 51

4.3.2.2 SEM-EDX ……. 52

4.3.2.3 TGA ……. 54

4.3.2.4 CHN elemental analysis ……. 54

4.3.2.5 FTIR ……. 55

4.3.2.6 DR UV-vis …… 57

4.3.2.7 XRD …… 57

4.3.2.8 XPS …… 59

4.3.3 Photocatalytic HER …… 63

4.3.4 Surface Area Analysis …… 64

4.3.5 Effect of Catalyst and Photosensitizer amount on Photocatalytic HER …… 65

4.3.6 Effect of pH on Photocatalytic HER ……..…… 68

4.3.7 Band Alignment between $[Ru(bpy)_3]^{2+}$ and the Catalyst ……..... 68

4.3.8 Control Experiment ……. 69

4.3.9 Post-Catalytic Characterization ……..… 71

4.3.10 Electrocatalytic HER ……..… 73

CHAPTER 5

5.0 CONCLUSIONS …… 74

5.1 Summary ……. 74

5.2 Remarks ……. 76

CHAPTER 6

6.0 BIBLIOGRAPHY …… 78

CHAPTER 7

7.0 APPENDIX ……. 95

7.1 Turn Over Frequency (TOF) Calculations ……. 95

7.1.1 Lower bound TOF (TOF_{lb}) ……. 95

7.1.2 Upper bound TOF (TOF_{ub}) ……. 95

LIST OF FIGURES

Figure 1.1: Schematic of solar water splitting using a suspended photocatalyst…… 2

Figure 1.2: Electron transfer pathway in natural photosynthesis. All processes from PS I that lead to the Calvin-Benson cycle where CO_2 is reduced are omitted and replaced with a dash line… 3

Figure 1.3: (a) Chemical structure of the OEC of photosystem II obtained at 1.9 A resolution. Colours: Mn, purple; Ca, yellow; bridging oxo groups, red; bound water molecules, orange. Reprinted with permission from ref [15]. Copyright 2011 Elsevier B. V. (b) Catalytic (Kok) cycle of the OEC from S_0 to S_4…… 4

Figure 1.4: Diagram showing the key components of natural photosynthesis and a comparison with an artificial design that mimics the natural functional components……. 6

Figure 1.5: Electronic transition (excitation and emission) in an inorganic metal complex, ML_6, in an O_h symmetry. LMCT: ligand to metal charge transfer; LC: ligand centered transition; MC: metal centered transition; MLCT: metal to ligand charge transfer…… 7

Figure 1.6: Potential energy surface diagram for $[Ru(bpy)_3]^{2+}$showing the relevant electronic states, transitions, and lifetimes……. 8

Figure 1.7: Scheme of photocatalytic water oxidation cycle of a catalyst in the presence of persulfate and a photosensitizer……. 10

Figure 1.8: (a) reductive quenching and (b) oxidative quenching pathway scheme of photocatalytic hydrogen evolution cycle of a catalyst in the presence of sacrificial reductants and a photosensitizer…….……. 12

Figure 1.9: A simplified crystal structure PBA ($A_xT_y[M(CN)_6]\cdot zH_2O$) in the *Fm3m* space group. The T site, M site, C, and N are represented by the green, violet, blue, grey, and blue spheres, respectively. The A in the vacant interstitial sites are shown by the pink balls. The water molecules also present in the interstitial sites are omitted due to clarity…… 13

Figure 1.10: The octahedral coordination environment of the metal sites in Co–M PBA……. 14

Figure 1.11: Schematic drawing showing (i) the coordination tuning of the metal sites to achieve an ideal catalytic cobalt environment for water oxidation and hydrogen evolution reaction. (ii) electron transfer pathway between $[Ru(bpy)_3]^{2+}$ and the catalytic cobalt site……. 19

Figure 3.1: (a) UV-Vis absorption spectra of an aqueous solution of $CobpyCl_2$, $Cobpy_2Cl_2$, $CophenCl_2$, and $Cobpy_2Cl_2$. Inset: absorption bands in the visible region of the spectra (400 – 600 nm). (b) FTIR spectra of bipyridine (bpy) and their corresponding cobalt bipyridine precursors. (c) FTIR spectra of phenanthroline (phen) and their corresponding cobalt phenanthroline precursors…… 29

Figure 3.2: Schematic illustration for the synthesis and structural units of compounds: All five compounds are derived from the same precursor, $K_3Fe(CN)_6$. The resulting cyanide coordination compounds differ in their Co precursors; (top) 3D crystalline **[Co–Fe]**, (middle) low-dimensional **[Cobpy–Fe]** and **[Cophen–Fe]**, and (bottom) molecular **[Cobpy2–Fe]** and **[Cophen2–Fe]** compounds. The curved lines represent bpy and phen ligands framed by the blue circles. Reprinted with permission from Ref. [70]. Copyright 2022. American Chemical Society……. 30

Figure 3.3: SEM micrographs of (a) **[Co–Fe]**, (b) **[Cobpy–Fe]**, (c) **[Cobpy2–Fe]**, (d) **[Cophen–Fe]**, and (e) **[Cophen2–Fe].** Scale bar: 10µm. Reprinted with permission from Ref. [70]. Copyright 2022. American Chemical Society……. 31

Figure 3.4: Thermogravimetric curves of CoFe compounds. Reprinted with permission from Ref. [70]. Copyright 2022. American Chemical Society…… 33

Figure 3.5: ATR-FTIR spectra of CoFe compounds at room temperature showing (a) the full spectrum from 4,000–400 cm^{-1} region. (b) the cyanide stretching region of the compounds with four different assignments: (I) terminal Fe^{2+}–CN, (II) terminal Fe^{3+}–CN & bridging Fe^{2+}–CN–Co^{2+}, (III) bridging Fe^{2+}–CN–Co^{3+}, and (IV) bridging Fe^{3+}–CN–Co^{2+} coordination mode. (b) PXRD patterns of compounds. Reprinted with permission from Ref. [70]. Copyright 2022. American Chemical Society…… 34

Figure 3.6: (a) PXRD patterns of **[Co–Fe]**, **[Cobpy–Fe]**, and **[Cophen–Fe]**. (b) PXRD patterns of **[Cobpy2–Fe]** and **[Cophen2–Fe]** matched with a reference compound. The reference is a previously synthesized molecular trigonal bipyramidal Co_3Fe_2 cluster $\{[Co(bpy)_2]_3[Fe(C.N.)_6]_2\}[Fe(C.N.)_6]_{1/3}$.[96] (c) Trigonal bipyramidal molecular structures of

[Cophen2–Fe] and **[Cobpy2–Fe]**. Reprinted with permission from Ref. [70]. Copyright 2022. American Chemical Society……. 36

Figure 3.7: High-resolution XPS spectra of (a) C1s, (b) N1s, (c) O1s, (d) Fe2p, and (d) Co2p peaks for the obtained samples. Reprinted with permission from Ref. [70]. Copyright 2022. American Chemical Society…… 38

Figure 3.8: Photocatalytic oxygen evolution activities of the compounds in a 0.1 M PBS (pH 7) containing 10 mg catalyst, (7.5 mg) 1 mM $[Ru(bpy)_3]^{2+}$ photosensitizer, and 5 mM $Na_2S_2O_8$ as the sacrificial electron scavenger with a white light source, 100 mW cm^{-2}. Reprinted with permission from Ref. [70]. Copyright 2022. American Chemical Society……. 39

Figure 3.9: Cyclic voltammogram of (a) **[Co–Fe]**, (b) **[Cobpy–Fe]** and (c) **[Cophen–Fe]** recorded at different scan rate ranging from 50 – 300 mV s^{-1}. Conditions: FTO (WE), Pt mesh (CE), Ag/AgCl (RE) in 0.1 M PBS (pH 7) containing 1 M KNO_3 as the supporting electrolyte. Inset: linear plot of the peak current (I) of Co^{3+}/Co^{2+} reduction wave versus scan rate (ν). Reprinted with permission from Ref. [70]. Copyright 2022. American Chemical Society…….……. 41

Figure 3.10: TOF_{ub} obtained by the compounds in the first 15 min. of photocatalysis. Reprinted with permission from Ref. [70]. Copyright 2022. American Chemical Society……. 42

Figure 3.11: (a) O1s and (b) N1s pristine and post-catalytic high-resolution XPS spectra for **[Cobpy–Fe]**. (c) O1s and (d) N1s pristine and post-catalytic high-resolution XPS spectra for **[Cophen–Fe]**. Reprinted with permission from Ref. [70]. Copyright 2022. American Chemical Society……. 44

Figure 3.12: High resolution XPS spectra of (a,c) Fe2p and (b,d) Co2p from the pristine and post-catalytic samples of **[Cobpy–Fe]** and **[Cophen–Fe]**, respectively. Reprinted with permission from Ref. [70]. Copyright 2022. American Chemical Society…… 45

Figure 3.13: FTIR spectra of the pristine and post-catalytic samples of **[Cobpy–Fe]** and **[Cophen–Fe]** showing (a) the full spectrum ranging from 4,000–400 cm^{-1} (the encircled region from 900–1,100 cm^{-1} indicates the coordination of bipyridyl ligands to the Co–Fe structures) and (b) the

cyanide stretching region ranging from 2,400–1,800 cm^{-1} (the asterisk point at ~ 2,100 cm^{-1} is ascribed to structural changes in the cyanide environment due to the coordination of bipyridyl groups to cobalt sites). Reprinted with permission from Ref. [70]. Copyright 2022. American Chemical Society……. 46

Figure 3.14: (a) PBAs proceeding through PCET steps to afford catalytically active Co(IV)–oxo/Co(III)–oxyl moiety, with incoming water attacking on Co–Oxygen moiety. (b) Electronic structure of Co–Oxygen moiety. (c) LUMO energies and orbital distributions for **[Co–Fe]**, **[Cophen–Fe]** and **[Cobpy–Fe]**. Reprinted with permission from Ref. [70]. Copyright 2022. American Chemical Society……. 47

Figure 4.1: Schematic illustration for the synthesis of 3D **[Co–M'']** and 2D **[Co–Ni]** coordination compounds and the coordination spheres of catalytic units……. 51

Figure 4.2: TEM micrographs of (a,b) **[Co–Fe]**, (c,d) **[Co–Co]**, (e,f) **[Co–Ni]** and (g,h) **[Zn–Ni]**. Scale bar: yellow (0.2 µm); red (50 nm); blue (20 nm); green (0.1 µm)……..... 52

Figure 4.3: SEM micrographs of (a) **[Co–Fe]**, (b) **[Co–Co]**, (c) **[Co–Ni]** and (d) **[Zn–Ni]**. Scale bar: yellow (10 µm)…… 53

Figure 4.4: Thermogravimetric weight loss analysis…… 54

Figure 4.5: ATR-FTIR spectra showing (i) the precursor and the synthesized PBA compounds ranging from 4,000–400 cm^{-1} (ii) showing the υ(CN) region ranging from 2,300–2,000 cm^{-1}. 56

Figure 4.6: Diffuse reflectance UV-Vis spectra of **[Co–Ni]**, **[Co–Fe]** and **[Co–Co]**……..… 57

Figure 4.7: (a) PXRD patterns of the compounds (b) PXRD of the as-synthesized **[Co–Ni]** matched perfectly with a reference compound. (c) Side view showing the interlayer distance of the crystal structure of **[Co–Ni]**. Colour code: Co, orange; Ni, white; C, grey; N, blue; O, red. H atoms of H_2O are omitted for clarity. The reference compound is a standard L_1 phase layered $Co(H_2O)_2[NiCN_4]\cdot xH_2O$ in an *Imma* space group, and the crystal structures were created from cif. files deposited at CCDC.[111] ……..... 58

Figure 4.8: High-resolution XPS spectra of (a,b) Co2p, (c,d) Ni2p, (e,f) O1s, and (g,h) N1s from the pristine and post-catalytic samples **[Co–Ni]**……. 60

Figure 4.9: XPS curve-fitting results of (a,b) Ni 2p, (c,d) Zn 2p spectra from pristine and post **[Zn–Ni]** samples…… 61

Figure 4.10: XPS curve-fitting results of (a,b) Co 2p, (c,d) Fe 2p spectra from pristine and post **[Co–Fe]** samples…….. 62

Figure 4.11: XPS curve-fitting results of Co 2p peaks spectra from (a) pristine and (b) post **[Co–Co]** samples……. 63

Figure 4.12: Photocatalytic HER activities of the compounds. Conditions: 10 mg Catalyst, 100 mM ascorbic acid, pH 5, (7.5 mg) 1 mM $[Ru(bpy)_3]Cl_2$, and 100 mW cm^{-2} white light source…….. 64

Figure 4.13: Cyclic voltammogram of (a) **[Co–Fe]**, (b) **[Co–Co]** and (c) **[Co–Ni]** recorded at different scan rate ranging from 25 – 125 mV s^{-1}. Conditions: FTO (WE), Pt mesh (CE), Ag/AgCl (RE) in 0.1 M PBS (pH 7) containing 1 M KNO_3 as the supporting electrolyte. Inset: linear plot of the peak current (I) of Co^{3+}/Co^{2+} reduction wave versus scan rate (ν)…… 65

Figure 4.14: (a) The effect of the amount of catalyst on the photocatalytic HER performance of **[Co–Ni]** for 1 h. (b) The effect of the amount of Ru on the photocatalytic HER performance of **[Co–Ni]** for 1 h…… 66

Figure 4.15: The effect of pH on the photocatalytic HER performance of **[Co–Ni]** (2 mg) for 1 h……. 68

Figure 4.16: (a) LSV profiles and the zoomed onset potential of **[Co–Ni]**. (b) UV-Vis spectra of $[Ru(bpy)_3]^{2+}$ in ascorbic acid solution, showing the absorbance tail of around 500 nm. (c) Extracted energy band diagram of **[Co–Ni]** for the photocatalytic hydrogen reduction process, involving the electron transfer mechanism……. 69

Figure 4.17: (a) Comparison of photocatalytic HER performance of **[Co–Ni]** and **[Zn–Ni]**. Conditions: 10 mg Catalyst, 100 mM ascorbic acid, pH 5, 1 mM $[Ru(bpy)_3]Cl_2$, and 100 mW cm^{-2} white light source. (b) Diffuse reflectance UV-Vis spectra of **[Co–Ni]** and **[Zn–Ni]** (c) UV-Vis absorption spectra of 10 mM aqueous solution of $Co(NO_3)_2{\cdot}6H_2O$ and $K_2Ni(CN)_4$..…….. 70

Figure 4.18: Photocatalytic HER activity of **[Co–Ni]** upon addition of only 1 mM $[Ru(bpy)_3]Cl_2$, into the reaction mixture after 3 hours of illumination…….. 71

Figure 4.19: PXRD spectra of the pristine and post-catalytic samples of **[Co–Ni]**…….. 72

Figure 4.20: ATR-FTIR spectra of the pristine and post-catalytic samples of the compounds showing the full spectrum ranging from 4000 to 400 cm^{-1}…… 72

Figure 4.21: LSV curves of the compounds on a FTO electrode in 0.1 M KPi electrolyte at pH 7 at a scan rate of 50 mVs^{-1}. (b) LSV curve of the compounds on a FTO electrode upon addition of 10 mM Trifluoroacetic acid (TFA) into the 0. 1 M KPi electrolyte. Conditions: FTO (WE), Pt mesh (CE), Ag/AgCl (RE) in 0.1 M PBS (pH 7) containing 1 M KNO_3 as the supporting electrolyte. All the potentials are converted to RHE using the relation $E_{RHE} = E_{AgCl} + E^{\theta}_{AgCl}$, where E^{θ}_{AgCl} = 0.198 V vs NHE at T = 25 ºC.[134]…….. 73

Figure 5.1: Schematic diagram showing the relationship between the well-defined ligand coordination environment and activity. Reprinted with permission from Ref. [70]. Copyright 2022. American Chemical Society……... 75

Figure 5.2: Schematic diagram showing the relationship in structure and catalytic activity by switching from 3D to 2D…… 76

LIST OF TABLES

Table 3.1: IR bands on the cobalt precursors and their assignments……... 30

Table 3.2: EDX elemental analysis of CoFe compounds and their obtained chemical formulas…… 32

Table 3.3: CHN elemental analysis of the CoFe compounds……. 33

Table 3.4: Cyanide stretching frequencies, υ(CN), of the CoFe compounds and their assignments…… 35

Table 3.5: Comparison of water oxidation TOF of various cobalt catalysts and PBA-based compounds…… 43

Table 4.1: The obtained chemical formula of the compounds derived from EDX elemental analysis and thermogravimetric analysis (TGA)……. 53

Table 4.2: CHN elemental analysis of the synthesized compounds…… 55

Table 4.3: Cyanide stretching frequencies, υ(CN), of the precursors and the synthesized compounds…… 56

Table 4.4: Comparisons of the photocatalytic hydrogen evolution activities of various heterogeneous catalyst systems……. 67

CHAPTER 1

1.0 INTRODUCTION

Undoubtedly, one of the crucial challenges tackled by present-day scientists is the development of clean and sustainable energy pathways. The US Department of energy projected a considerable increase in energy consumption up to 8.1 x 10^{20} J by 2040.[1] In addition, the world's heavy reliance on the use of fossil fuel as a source of energy has resulted in an accelerated increase in the concentration of atmospheric CO_2, exceeding 800 ppm in 2015 for the first time in 800,000 years.[2]

The unusual increase in the global energy demands due to the continual increase in the world's population, coupled with the devastating environmental issues associated with the combustion of fossil fuels, have raised a huge concern and triggered the scientific community to find a cheap, abundant, efficient, and green source of energy. One of the most attractive ways to address this crisis is to use the energy derived from sunlight to split water into oxygen and hydrogen, "solar water splitting". The hydrogen generated at the end of the water-splitting process has been proposed as a clean and sustainable alternative energy to fossil fuels.[3]

1.1 Photocatalytic (Solar) Water Splitting

Given the natural abundance of water and sunlight, splitting water into molecular oxygen and hydrogen with solar energy has proven to be a green and inexhaustible approach to addressing the global energy crisis (Figure 1.1).[4] Although the intermittent nature of the sun limits its practical application, the utilization of solar for energy production still holds a great promise since the amount of energy radiated on the earth's surface by the sun in a day is far more than human energy needs for the whole year.[5] For instance, a recent report from the US Department of Energy reveals that suspended heterogeneous photocatalysts operating at 10% solar energy conversion efficiency are theoretically able to produce hydrogen fuel at the cost of \$1.63/kg H_2,[6] which is cheaper than the hydrogen generation from electrolysis estimated at the lowest cost of \$2.3/kg H_2.[7]

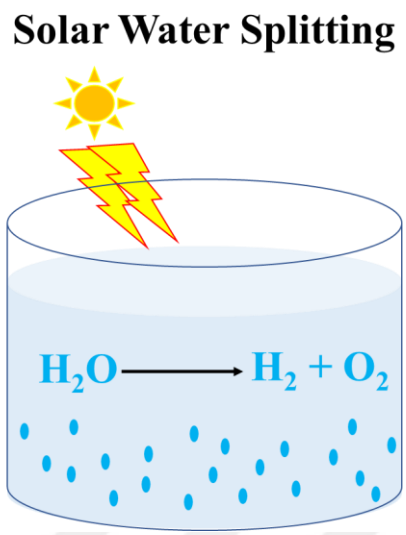

Figure 1.1: Schematic of solar water splitting using a suspended photocatalyst.

Water splitting reaction can be divided into two main half-reactions, namely oxygen evolution reaction (OER) and hydrogen evolution reaction (HER).[8] The OER step involves the oxidation of water:

$$2H_2O \rightarrow O_2 + 4H^+ + 4e^-;\ E^0 = 1.23 - 0.059 \text{ x pH V vs NHE} \qquad \text{Eq. 1}$$

The oxidation of water provides electrons and protons, which are then utilized in the HER step for the reduction of protons:

$$2H^+ + 2e^- \rightarrow H_2;\ E^0 = -0.059 \text{ x pH V vs NHE} \qquad \text{Eq. 2}$$

The OER step is considered the bottleneck of this reaction since it involves a complex four-electron/proton transfer pathway and a rate-limiting O–O bond formation, leading to a large overpotential and, thus, limiting the efficiency of the overall reaction.[1] Nonetheless, performing an overall water splitting reaction requires the water oxidation system to be coupled with an efficient water reduction catalyst. Thereby, catalysts that can efficiently drive both of these reactions are desired.

The state-of-the-art catalysts for the OER and HER are noble metals such as Pt, Ir, Ru, and their oxides.[9]–[12] However, rarity and high cost greatly restrict their commercial applications. Therefore, tremendous research efforts have been devoted to the development of a cheap, earth-

abundant, and robust catalyst that can drive water-splitting reaction efficiently for large-scale applications.

1.2 Inspiration from Nature

From the beginning of time, nature has provided us with a fundamental knowledge of harnessing the energy from sunlight for water splitting. In natural photosynthesis (Figure 1.2), light energy is extracted by an enzyme complex known as the photosystem II (PSII) to oxidize water into molecular oxygen, four electrons and four protons.[5] Upon excitation of the PSII system by light with an optimum wavelength of 680 nm, the chlorophyll centre known as the P_{680} is oxidized (forming a cation radical, P_{680}^{+}), and a pheophytin molecule is reduced (forming an anion radical, $Pheo^{-}$).[13] The electron generated with the excitation of P_{680} is transferred to an acceptor system where it proceeds from a tightly bound quinone cofactor Q_A to a weakly bound Q_B to undergo a two-electron/proton reduction. Then, through the cytochrome b_6f complex and photosystem I, until CO_2 is reduced in the Calvin-Benson Cycle.[14]

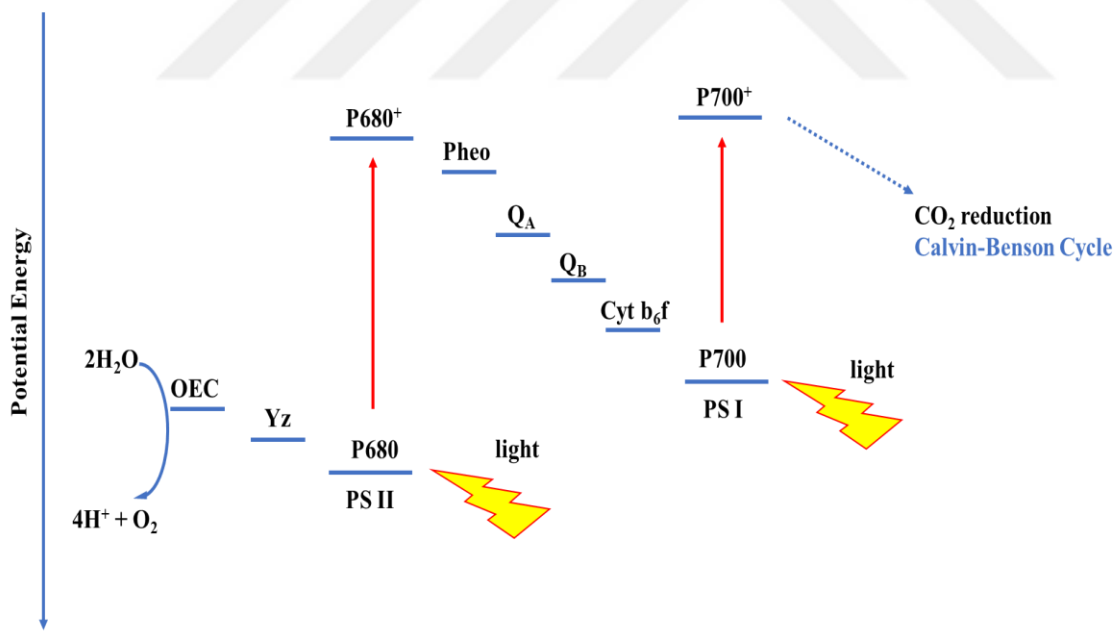

Figure 1.2: Electron transfer pathway in natural photosynthesis. All processes from PS I that lead to the Calvin-Benson cycle where CO_2 is reduced are omitted and replaced with a dash line.

The key to water splitting is the donor system, where the strongly oxidizing P_{680}^{+} (1.25 V vs NHE) oxidizes a redox-active tyrosine molecule (Y_Z), which is in close proximity to the oxygen evolving complex (OEC), Mn_4Ca-cluster, for efficient charge transfer.[13] After four consecutive one-

electron oxidation steps of the OEC by the oxidized P_{680}^{+} through S_0 – S_4 state transitions, two molecules of water are converted into molecular oxygen, four protons, and four electrons.[5] While the water splitting reaction of interest occurs in the donor system, it is important to note that the rate-determining step for natural photosynthesis is the $2e^{-}/2H^{+}$ reduction of Q_B that takes places in the acceptor system.[14]

1.2.1 Oxygen Evolving Complex (OEC)

It is pertinent to understand the detailed structure and coordination environment of the oxygen evolving complex in order to uncover the mechanism of photocatalytic water oxidation and to design a similar catalyst. The OEC is a tetra-manganese cluster consisting of one calcium and four manganese atoms (Mn_4Ca-cluster).[15] This is a cubane-like structure, consisting of three of the manganese and the calcium atom arranged at the corners of a tetrahedron with three μ-oxo bridges on each atom (Mn_3CaO_4), while the fourth manganese is dangling and connected to the cubane by a mono-μ-oxo bridge (Figure 1.3a).[5] While earlier studies have shown that the OEC is mainly coordinated to oxygen and nitrogen bonds within its first coordination sphere, later spectroscopic investigations have revealed the presence of coordinating amino acid ligands in the extended sphere, which provide a stable ligand environment for the metal cluster.[16]

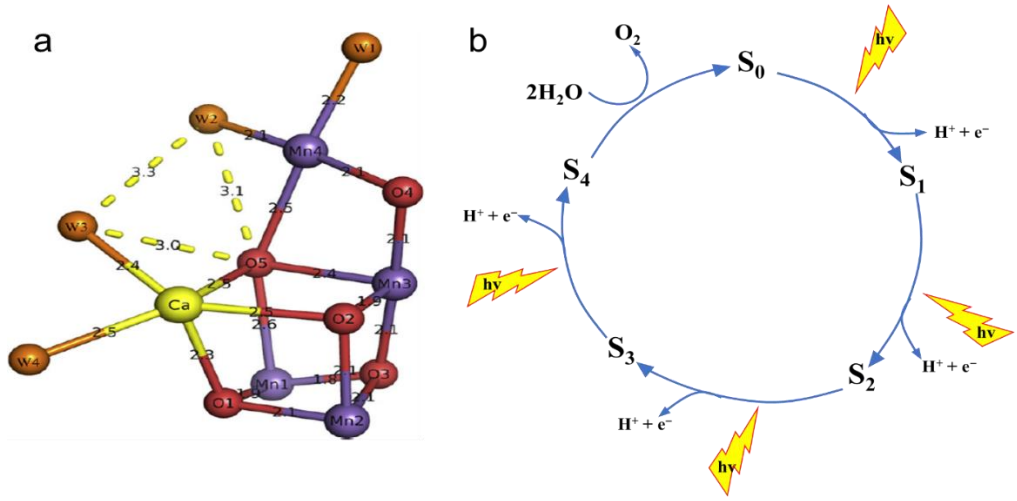

Figure 1.3: (a) Chemical structure of the OEC of photosystem II obtained at 1.9 A resolution. Colours: Mn, purple; Ca, yellow; bridging oxo groups, red; bound water molecules, orange. Reprinted with permission from ref [15]. Copyright 2011 Elsevier B. V. (b) Catalytic (Kok) cycle of the OEC from S_0 to S_4.

The OEC catalyses water oxidation by cycling from the S_0 – S_4 state transition (Kok cycle).[17] Each oxidation state of OEC is referred to as the S-state, where S_0 is the most reduced state (the cycle begins with S_0) and S_4 is the most oxidized state (Figure 1.3b). The oxidation of the S-states is induced by the strongly oxidizing P_{680}^+ group. P_{680}^+ is the most oxidizing species known in biology, with an estimated reduction potential of 1.25 V vs NHE.[18] This potential is sufficiently strong to drive water oxidation at pH 7 (E^0 = 820 mV), making this kinetic limiting water oxidation proceed at a relatively fast rate. All these characteristics support that the OEC is an exceptionally advanced water oxidation catalyst, reaching an optimal turnover frequency of 400 mol of O_2 (mol OEC)$^{-1}$ s^{-1}.[14]

1.3 Artificial Photosynthesis (Mimicking Natural Photosynthesis)

Artificial photosynthesis involves using the fundamental understanding of the complex biological process taking place in natural photosynthesis to build synthetic systems that can perform identical functions efficiently.[19] Researchers rely on these principles to construct and tune new materials for solar water splitting. Similar to natural photosynthesis, an efficient artificial photosynthetic system must possess three main components (Figure 1.4);[20] i) a light-absorbing component that can absorb radiation from sunlight preferable in the visible region, ii) a water oxidation catalyst that can efficiently oxidize water into oxygen, protons, and electrons, and iii) a water reduction catalyst that can reduce the protons and electrons generated from the oxidation step into hydrogen. A common strategy adopted for the development of catalysts is to investigate water oxidation and reduction reactions separately in the presence of a sacrificial oxidant and reductant, respectively.[19], [21]–[23]

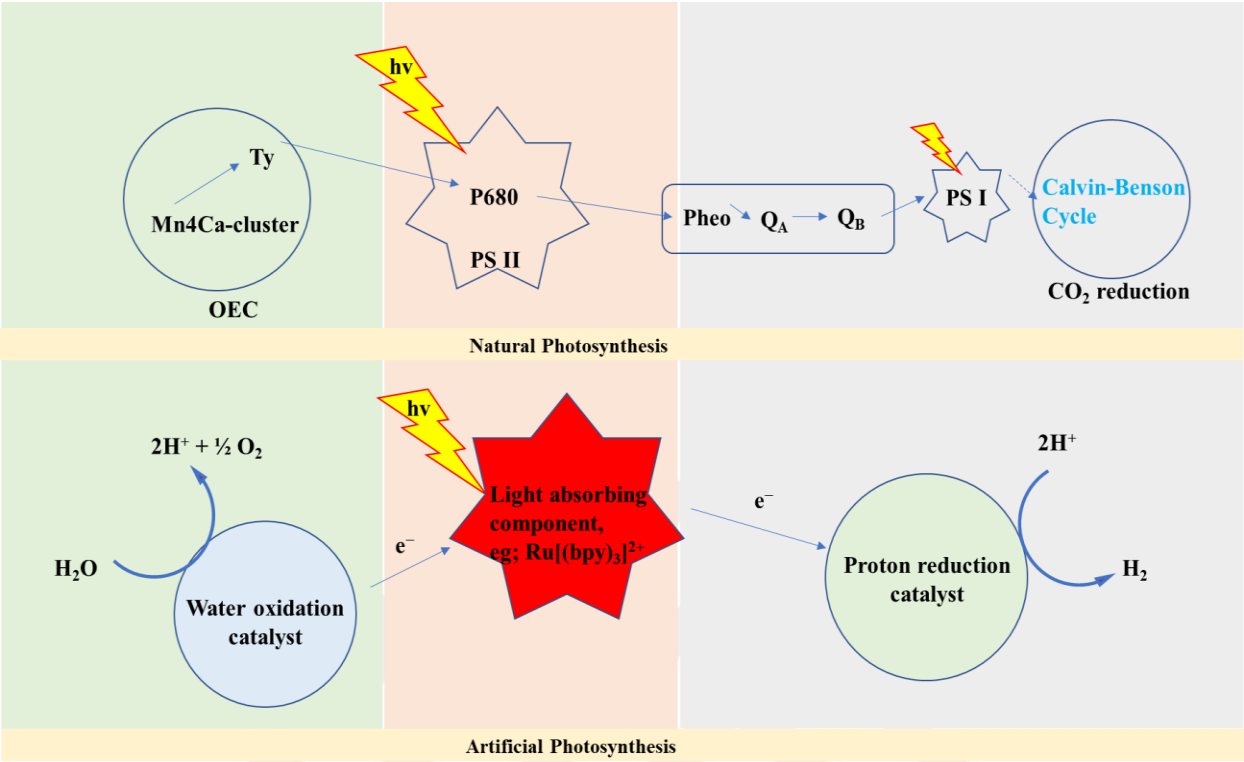

Figure 1.4: Diagram showing the key components of natural photosynthesis and a comparison with an artificial design that mimics the natural functional components.

1.3.1 The Light Absorbing Component (Photosensitizer)

In agreement with natural photosynthesis, the first feature required for the design of an artificial solar water splitting system is a light-harvesting chromophore or a photosensitizer. A good chromophore should possess the following characteristics:(i) The ability to absorb light strongly over a broad range since more than 47% of the solar spectrum is composed of visible radiation, (ii) a redox potential suitable for water oxidation or reduction reactions, (iii) a long excited-state lifetime within nanosecond to microsecond range or lifetime long enough for charge-transfer reaction to take place, (iv) a chromophore, which could be easily synthesized and with excited/ground state properties that can be easily adjusted, and finally (v) a long-term stability.[24] Light-harvesting components used so far include inorganic metal complexes, organic dyes, and semiconductors.[25]–[28] The inorganic or organic dyes can also be coupled to a proper semiconductor to form a dye-sensitized assembly.[29]–[31]

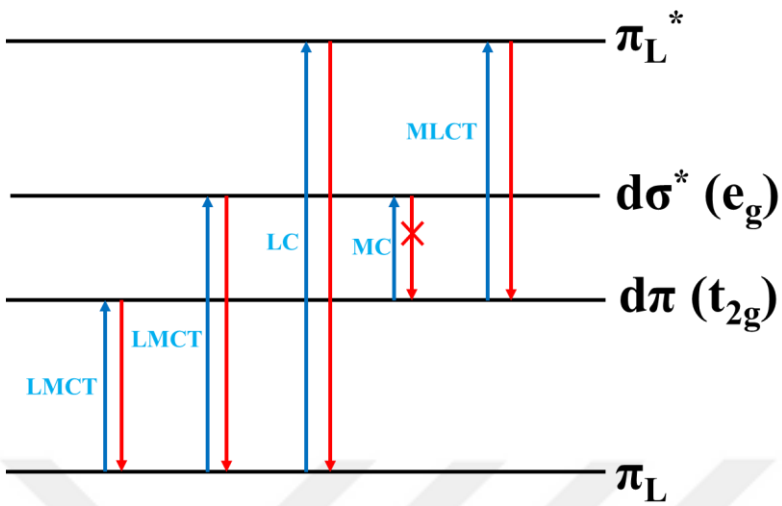

Figure 1.5: Electronic transition (excitation and emission) in an inorganic metal complex, ML_6, in an O_h symmetry. LMCT: ligand to metal charge transfer; LC: ligand centered transition; MC: metal centered transition; MLCT: metal to ligand charge transfer.

Among these chromophores, the most studied are the inorganic metal complexes. Inorganic metal complexes are favourable as photosensitizers due to their charge-transfer excited state transitions (Figure 1.5).[24] They can undergo metal to ligand charge transfer (MLCT), which involves a photo-induced electron transfer from the metal-centred t_{2g} orbital (HOMO) to the ligand-centred π^* orbital (LUMO).[32] This MLCT transition leads to a photo-induced one-electron oxidation of the metal and one-electron reduction of the ligand. The redistribution of electron density dramatically alters the excited states' redox potential and makes them a better oxidant and reductant than the ground state.[33] The reactivity of the MLCT excited state facilitates a charge transfer process similar to natural photosynthesis. Ru(II) and Ir(II) metal complexes have been explored as efficient chromophores due to their exciting electronic and excited state properties.[32] Isoelectronic Fe(II) metal complexes have also emerged recently due to the desire to replace expensive Ru(II) and Ir(II) complexes with earth-abundant ones.[34]

1.3.1.1 Ru(II) Photosensitizers

The most investigated inorganic metal-complex photosensitizer is the $Ru(bpy)_3^{2+}$ due to its rich excited state photochemistry.[35] $Ru(bpy)_3^{2+}$ has a strong MLCT excitation in the visible region (λ_{max} = 452 nm in acetonitrile solution), which involves a one-electron transfer from the metal to

the ligand orbital as depicted in Eq 3. The MLCT excited state $[Ru^{III}(bpy^{-})(bpy)_2]^{2+*}$ is more oxidizing and reducing than the ground state which enables it to be used in both reduction and oxidation reactions.[24], [36]

$$[Ru^{II}(bpy)_3]^{2+} \xrightarrow{hv} [Ru^{III}(bpy^{-})(bpy)_2]^{2+*} \qquad \text{Eq. 3}$$

Upon visible light illumination, $Ru(bpy)_3^{2+}$ is excited into a short-lived ^{1}MLCT excited state, which relaxes rapidly within ~ 100 fs via intersystem crossing to the long-lived ^{3}MLCT excited state (Figure 1.6).[33] The ^{3}MLCT undergoes a phosphorescent emission in solution at room temperature (λ_{em} = 620 nm in acetonitrile solution).[33] The ^{3}MLCT excited state of $Ru(bpy)_3^{2+}$ has a long lifetime of about 1.1 µs.[37] Unique properties such as strong absorption in the visible range, excellent redox properties of the excited state, and long excited state lifetime make $Ru(bpy)_3^{2+}$ and other Ru-type complexes one of the most widely used chromophores for photo-redox catalysis.[5], [35]

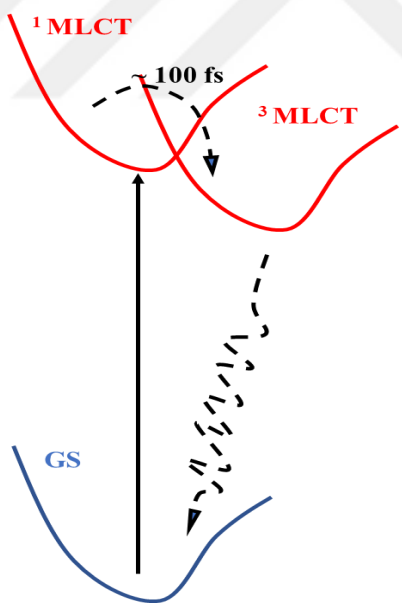

Figure 1.6: Potential energy surface diagram for $[Ru(bpy)_3]^{2+}$showing the relevant electronic states, transitions, and lifetimes

1.3.2 The Catalyst

Besides excitation of the chromophores and generation of excited state carriers (electrons and holes), an efficient catalyst is required to handle the catalytic reaction process.[20] A solar water

splitting catalyst is accessed based on key parameters,[38] such as (i) cost: a catalyst that will mimic natural photosynthesis should be inexpensive, (ii) stability: the stability of a catalyst is accessed by subjecting the catalyst to long-term experiment and performing post-catalytic characterization to ensure that the catalyst is not degraded, and (iii) activity: the activity of the exposed catalytic sites can be evaluated from the turnover number (TON) or turnover frequency (TOF).

$$TON = \frac{no\ of\ H_2/O_2\ evolved}{no\ of\ active\ site}$$

Eq. 4

$$TOF = \frac{no\ of\ H_2/O_2\ evolved}{no\ of\ active\ sites\ \times reaction\ time}$$

Eq. 5

Two catalytic systems are required for solar water splitting, namely; the oxidation catalyst where oxygen evolution takes place and the reduction catalyst where hydrogen evolution reaction occurs. To thoroughly investigate the structure-function relationship of a catalyst, an approach commonly used by most studies is to catalyse these half-reactions separately in the presence of sacrificial reagents.

1.3.2.1 The Water Oxidation Catalyst (WOC)

Water oxidation is a fundamental and key reaction in photosynthesis. It involves a four electron-proton transfer (Eq. 1), and requires a thermodynamic potential of $E^0 = -1.23$ V vs RHE.[5], [8] The mechanism of water oxidation proceeds through a four proton-coupled electron transfer (PCET steps), beginning with the coordination of H_2O to the reactive site, then the formation of hydroxo species, followed by the formation of oxo-intermediate, the formation of oxyhydroxide intermediate, and finally the removal of H^+ to produce O_2.[39], [40] Classical mechanistic studies have shown that the rate-determining step of this mechanism is the O–O bond formation step, which primarily involves the attack of water molecules on the high valent oxo-intermediate resulting in the formation of the oxy-hydroxide intermediate.[40] The water oxidation reaction is regarded as the limiting step in overall water splitting due to the complexity of the kinetics and thermodynamics involved in this process.[14]

Numerous catalysts, including homogeneous and heterogeneous systems have been investigated for water oxidation. The benchmark catalysts for water oxidation are the high-performing IrO_x and RuO_2.[41], [42] However, the high cost and rarity of the noble metals have restricted their practical application and led to the search for low-cost catalysts such as the first-row transition metals (TM). Inspired by nature, Mn-based catalysts similar to the OEC (Mn_4Ca-cluster) have been studied and shown to be active for water oxidation.[43] Various other first-row TM-based systems have been used for the development of a low-cost and efficient water oxidation catalyst. In particular, the catalysts made from cobalt have shown to be more promising as an alternative to the noble metals.[19] The homogenous systems that have been investigated include metal polypyridyl complexes, while the heterogeneous systems are metal oxides, metal hydroxides, metal nitrides, metal-organic frameworks (MOFs), etc.[44]–[47] Metal-free catalysts such as graphene and carbon nanotubes have also been studied for water oxidation.[2]

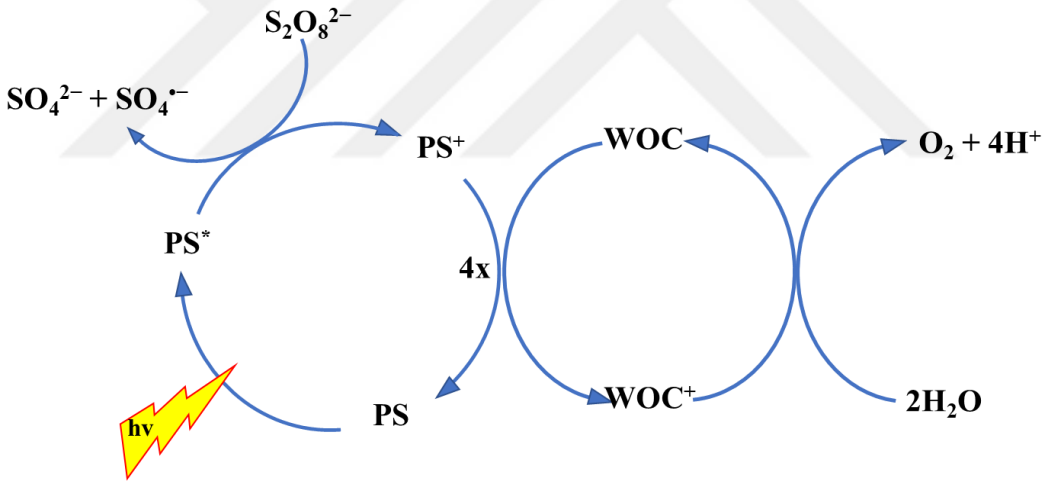

Figure 1.7: Scheme of photocatalytic water oxidation cycle of a catalyst in the presence of persulfate and a photosensitizer.

The Photocatalytic (solar-driven) water oxidation process could be investigated separately as a half-reaction in the presence of sacrificial oxidants such as sodium persulfate ($Na_2S_2O_8$) and silver nitrate ($AgNO_3$).[48], [49] The most commonly used sacrificial oxidant for water oxidation is $Na_2S_2O_8$.[49] In a photocatalytic set-up containing $Na_2S_2O_8$, the excited photosensitizer is oxidized by the persulfate ion, and then the oxidized PS oxidizes the WOC, which in turn oxidizes water into O_2 after four consecutive electron transfer steps (Figure 1.7).[50]

1.3.2.2 The Reduction or The Hydrogen Evolution Catalyst

The other half of water splitting is the reduction of protons to hydrogen, which involves a two-electron reduction (Eq. 2) with a thermodynamic potential of E^0 = 0 V vs RHE.[8] The classic HER mechanism proceeds through the reduction of the reactive metal site, the formation of a metal-hydride species, and finally, the evolution of H_2.[51] Hydrogen (H_2) is believed to be the most promising alternative to fossil fuel, and therefore, the development of a highly-active catalyst for this process is pertinent.

Platinum sits at the top of the ranks and is regarded as the best catalyst for HER,[52] but its practical utilization is limited owing to its low abundance and high cost. Therefore, significant attention has been paid to earth-abundant transition metal catalysts such as Co, Fe, Ni, and Mo. Similar to water oxidation, Co-containing catalysts have been used and studied extensively due to their exciting redox chemistry.[19] Earth-abundant TM catalysts such as metal sulfides, metal selenides, metal nitrides, and MOFs have been used as heterogeneous catalytic systems,[4], [53] while metal polypyridyl, cobaloximes, cobalt-corroles, and cobalt-dithiolenes have been investigated extensively as homogeneous catalytic systems.[51], [54], [55] Notable of mention are the highly active [FeFe], [NiFe], and [Fe] hydrogenases found in nature, which can catalyze hydrogen evolution with turnover frequencies beyond 9000 s^{-1}.[56] While it is difficult to use these enzymes directly in a non-natural environment, innovative and efficient catalysts mimicking the hydrogenases have been developed recently for HER.[57]–[61]

A hydrogen evolution catalyst could be coupled with a water oxidation catalytic system for overall photocatalytic water splitting. However, the hydrogen evolution catalyst can be studied independently as a half-reaction in the presence of sacrificial reductants (SR) such as ascorbate, triethanolamine (TEOA), triethylamine (TEA), acetic acid, and methanol.[21], [62]–[70] In a three-component photocatalytic set-up containing the HEC, SR, and photosensitizer, the excited photosensitizer can be quenched via two different electron transfer quenching pathways known as the reductive quenching or oxidative quenching. In the reductive quenching pathway, the excited photosensitizer is reduced by the SR, then the reduced PS reduces the HEC, which in turn reduces H^+ into H_2 after two consecutive electron transfer steps (Figure 1.8a).[21] In an oxidative quenching pathway, the excited photosensitizer reduces the HEC, which in turn reduces H^+ into H_2 after two consecutive electron transfer steps, and the PS is regenerated by electron transfer from

the SR (Figure 1.8b).[23] Under the experimental conditions of our HER experiment performed in chapter four, the concentration of ascorbate which served as the SR is far greater than the catalyst concentration. Thus, reductive quenching will be the dominating pathway as ascorbate will be the primary quencher of the PS.

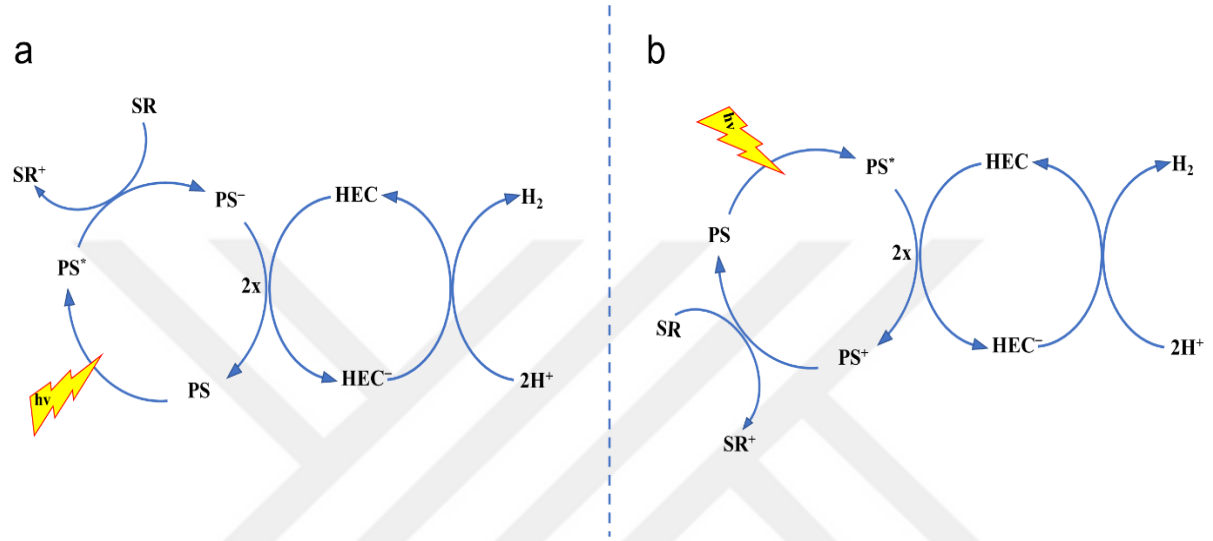

Figure 1.8: (a) reductive quenching and (b) oxidative quenching pathway scheme of photocatalytic hydrogen evolution cycle of a catalyst in the presence of sacrificial reductants and a photosensitizer.

1.4 Prussian Blue Analogues as Water Splitting Catalysts

Prussian blue (PB) is an insoluble pigment initially discovered in the 18th century by a German pigment manufacturer. The earliest studies performed by inorganic chemists recognized PB as a mixed-valence Iron(III)hexacyanoferrate(II) compound, $Fe_4[Fe(CN)_6]_3 \cdot xH_2O$ (x = 14 – 16).[65] The pioneer single crystal study performed by Buser *et al.* in 1977 reported that PB belongs to the face-centered cubic (fcc) unit cell in the *Fm3m* or *Pm3m* space group.[66] Subsequently, modern inorganic chemists discovered that other transition metals could replace the Fe species in PB to generate what is termed Prussian blue analogues (PBAs).

PBAs are a diverse class of three-dimensional coordination polymers with a general formula, $A_xT_y[M(CN)_6] \cdot zH_2O$, where T and M are transition metals, and A is an alkali or an alkaline metal ion positioned in the tetrahedral interstitial sites (Figure 1.9).[67] It adopts a face-centered cubic (fcc) structure in the *Fm3m* space group with a lattice parameter varying from 10.10

to 10.25 Å.[68]–[70] The two metal sites (T and M) are connected through cyanide bridging ligands to afford an extended framework, in which M is connected from the C end, and T is connected from the N end. The water molecules in the framework can either coordinate to the N-ligated transition metals sites (T) or exist in the interstitial sites/vacancies.[67]

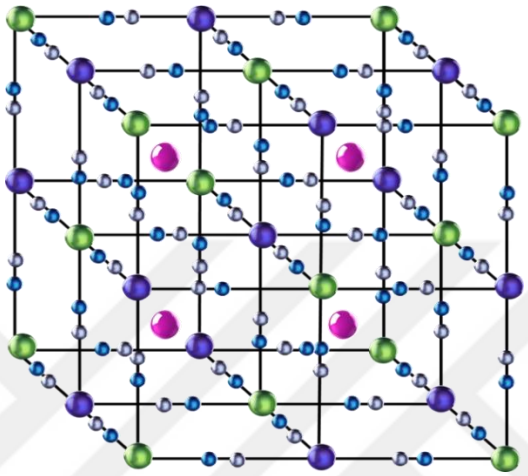

Figure 1.9: A simplified crystal structure PBA ($A_xT_y[M(CN)_6]\cdot zH_2O$) in the *Fm3m* space group. The T site, M site, C, and N are represented by the green, violet, blue, grey, and blue spheres, respectively. The A in the vacant interstitial sites are shown by the pink balls. The water molecules also present in the interstitial sites are omitted due to clarity.

PBAs have garnered an intense research interest as water splitting catalysts due to their exiting synthetic and structural characteristics: i) They have a facile synthetic procedure from cheap precursors, which makes it economically affordable for large-scale water splitting. ii) They constitute easily tuned metal sites. The structure could be easily modified with substrates that can impart unique functionality, electronic properties, or morphology. iii) They exhibit porous and robust network structures with the ability to retain their structural configuration under water splitting catalysis at a wide pH range (pH 1 – 13). iv) They possess a fast electron transfer between the metal sites through the short cyanide bridge.[71] In addition to water splitting catalysis, PBAs have been used in various applications such as gas storage, batteries, electrochromism, magnetism, and sensors.[72]

1.4.1 Coordination Environment of PBAs for Water Splitting

Initial investigations on the tuning of the metal sites in PBAs and all the current works on the application of PBAs for heterogeneous water splitting catalysis have shown that the cobalt hexacyanometalate analogue, $A_xCo_y[M(CN)_6].zH_2O$ (Co–M PBA), exhibits superior activity and stability.[47], [69], [73], [74] These studies indicate that the cobalt sites with accessible sites, which are on the surface or in the vacancies created to provide charge balance, are the active catalytic sites for water splitting (Figure 1.10). The cyanometalate site does not serve as a catalytic site due to the lack of an accessible coordination site, however, it plays an important electronic role in enhancing the activity and the stability of cobalt sites. The structural coordination of the surface catalytic cobalt sites in Co–M PBA mimics that of the highly active sites in natural photosynthesis due to its ability to coordinate to water molecules or protons for water splitting catalysis without being destroyed in the process and their judicious use of the cyanide linkage for efficient charge transfer and stability. These interesting and unique chemistry makes PBAs an efficient bifunctional heterogeneous catalyst that can catalyze both OER and HER processes.

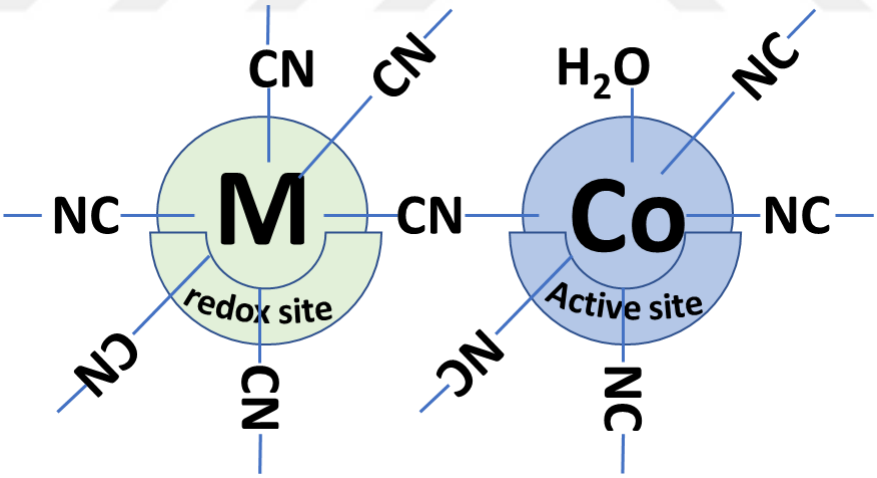

Figure 1.10: The octahedral coordination environment of the metal sites in Co–M PBA.

1.4.2 PBAs for Photocatalytic Water Oxidation

In contrast to homogeneous systems which suffers from instability under photocatalytic condition and non-scalability, Prussian Blue (PB), $Fe_4[Fe(CN)_6]_3$, has been recognized as far back as the late 20th century as a highly stable heterogeneous catalyst. PB exhibited catalytic properties for water oxidation in the presence of $[Ru(bpy)_3]^{2+}$/persulfate couple and displayed remarkable

stability.[75], [76] Later in 2014, Galán-Mascarós and co-workers performed the first study on the application of Co-PBAs for photocatalytic water oxidation in the presence of $[Ru(bpy)_3]^{2+}$/persulfate couple.[69] They found that Co–Fe and Co–Co analogues exhibit a maximum initial TOF of 4.5 x 10^{-4} s^{-1} and 8.1 x 10^{-4} s^{-1}, respectively, which is higher than that of commercially available Co_3O_4 (4.2 x 10^{-4} s^{-1}). The success of this work portrayed Co-M PBA as a competitive candidate for photocatalytic water oxidation and inspired other research groups, including our own, to study PBAs extensively for water splitting. The several works that have been done in this field to enhance the photocatalytic water oxidation activity of PBAs could be divided into four main strategies.

i) Utilizing PBA as a pre-catalyst: Due to the insufficient number of surface-active sites in PBAs, the majority of studies in enhancing the activity tend to use PBA as a precursor and integrate it with other highly active and conductive materials, which leads to reconstruction or decomposition of the cyanide network to their corresponding oxides, phosphides, or selenides to form what is referred to as a "PB derived-catalyst". For instance, Guo *et al.* designed $Co(OH)_2$/CuO nanoparticles using Cu–Co PBA as a precursor.[77] The derived catalyst showed long-term stability and superior photocatalytic water oxidation performance in the presence of persulfate as an electron scavenger.

ii) Coupling PBA with a light-absorbing component: Another strategy commonly employed in this field is to couple PBA with a proper semiconductor (SC) or a photosensitizer. This strategy aims to achieve a proper energy level matching between the valence band of SC and the HOMO of the catalytic site to boost the OER activity and the stability of PB-based assembly. This strategy also significantly reduces electron-hole recombination on the SC owing to its efficient hole transfer to the PBA catalyst surface.[78] Several Co–Fe PBA catalyst/visible–light absorbing SC assemblies have been designed by our group, e.g. using a simple co-precipitation synthetic strategy, which prevents the decomposition of the cyanide network. A Co–Fe PBA catalyst was coupled with a layered double hydroxide (LDH),[79] a niobate,[80] $BiVO_4$,[81] and brown-TiO_2,[82] in different studies. Each of these assemblies displays a proper alignment of energy level, allowing an efficient hole transfer to the surface of Co–Fe PBA catalyst for photocatalytic water oxidation. Besides our work, Shi *et*

al. also designed an anisotropic PBA–TiO_2 Janus nanoreactor by growing TiO_2 nanoflakes on an etched Ni–Co PBA surface.[70] This assembly displayed improved photocatalytic activity compared to ordinary PBA or TiO_2 attributed to the unique Janus nanostructure.

iii) Changing or tuning the cyanometalate precursor: another adopted strategy is to chemically modify or tune the cyanometallate site, which will consequently have an indirect electronic effect on the activity on the catalytic sites. Yamada *et al.* prepared heteropolynuclear cyanide compounds by partially replacing the hexacyanocobaltate precursor in Co–Co PBA with octahedral $[Pt^{IV}(CN)_6]^{4-}$ or square planar $[Pt^{II}(CN)_4]^{2-}$ complexes.[74] The compounds showed an increase in photocatalytic water oxidation activity in the presence of $[Ru(bpy)_3]^{2+}$/persulfate couple, attributed to the electronic and structural modifications introduced by the Pt ions. In 2016, our group found that replacing the hexacyanoferrate precursor in Co–Fe PBA with a polymer bound pentacyanoferrate precursor results in the formation of an amorphous structure with 7 times increase in surface concentration of catalytic cobalt sites and consequently leading to an enhancement in the activity.[73] Follow-up studies by Galán-Mascarós group leveraged on comparative studies to understand the influence of ligands attached to the pentacyanoferrate precursor of CoFe–L PBA on its photoactivity.[83] Further investigations have elucidated the linkage of the pentacyanoferrate precursor to chromophore groups for the development of a molecular sensitizer-heterogeneous catalyst system. Kap and Karadas designed a heterogeneous PS-WOC dyad by incorporating a Ru–P4VP consisting of a bridging polymer to the pentacyanoferrate units of Co–$Fe(CN)_5$.[84] The synthesized dyad displayed higher activity than the physical mixture of CoFe PBA and Ru PS, and it retained its activity for at least 6 hours, which has not been achieved by a solution mixture of $[Ru(bpy)_3]^{2+}$ and catalyst due to the instability of $[Ru(bpy)_3]^{2+}$. In 2016, Karadas group designed the first earth-abundant PB-based catalyst triad, [CoFe–TPyP], by connecting TPyP organic chromophore to pentacyanoferrate precursor and then reacting with cobalt (ii) ions.[85] [CoFe–TPyP] displayed excellent photocatalytic water oxidation performance in the presence of persulfate ions as an electron scavenger, yielding an initial TOF of 4.5 x 10^{-4} s^{-1}, which is compatible with studies utilizing rare $[Ru(bpy)_3]^{2+}$ as the

photosensitizer. In addition, this molecular sensitized-PBA catalyst displayed extraordinary stability with no change in activity over a minimum of three cycles, which is difficult to attain in a ruthenium sensitized system due to bipyridyl poisoning.

iv) Changing or tuning the catalytic sites: Early investigations on the effect of the type of transition metals serving as the catalytic sites on the activity of PBA have shown the cobalt hexacyanometalate analogue (Co–M) to exhibit superior activity and stability.[69], [73] Few studies on directly tuning the catalytic cobalt sites without decomposition in the cyanide network are focused on partially substituting or doping with a different metal. Han and Galán-Mascarós showed that doping or partially substituting the catalytic cobalt sites in a Co-Fe PBA with $Fe^{II/III}$ resulted in an enhancement in OER activity.[86] Furthermore, Yamada *et al.* revealed that the introduction of small amounts of Ca^{2+} into the vacancies of Co–Co PBA leads to an increment in photocatalytic water oxidation activity in the presence of $[Ru(bpy)_3]^{2+}$/persulfate couple and maximum quantum efficiency of 200 % for O_2 evolution.[87]

1.4.3 PBAs for Photocatalytic Hydrogen Evolution

While substantial progress has been made on the utilization of PBAs for photocatalytic water oxidation, comparatively less attention has been paid to exploiting PBAs as a hydrogen evolution catalyst. PBAs exhibit an extremely low intrinsic HER activity compared to their heterogeneous metal sulphides and phosphides counterparts due to a smaller number of surface-active sites and low conductivity.[4], [88] Thus, high crystallinity and less accessible catalytic sites remain the main challenges to developing highly active PBA catalysts for HER processes. The studies on enhancing the photocatalytic hydrogen evolution activity are divided into two strategies.

i) Coupling PBA to the surface of a SC: In this strategy, PBA serves as a co-catalyst for efficient electron transfer and prevents charge carrier recombination. For instance, Pena *et al.* reported 16 times increase in photocatalytic HER activity using methanol as an electron donor when Cu–Co PBA is employed as a co-catalyst on the surface of TiO_2 compared to the bare TiO_2.[89] Recently, a PB–Co/CdS hybrid material synthesized by immobilizing Co–Co PBA on the surface of CdS reached a high photocatalytic HER activity of 57,228 μmol g^{-1} h^{-1} in the presence of lactic acid as a sacrificial electron donor.[90] The superb increase in activity achieved in both cases is attributed to the

faster charge transfer from the SC to the PBA, which is favoured by the bridging CN ligands.

ii) Decomposing the cyanide network by integrating with conductive materials to form a PBA-derived catalyst: The PBA-derived catalyst possesses the inherent properties of PBA and, in addition, enhanced electronic properties and surface-active sites. For instance, Qi et al. synthesized iron nitride (Fe_2N) nanoparticles by nitriding Prussian blue nanocubes.[91] The derived Fe_2N nanoparticles reached an optimal photocatalytic HER of 88.7 μmol g^{-1} h^{-1} on g-C_3N_4 nanosheets using TEOA as a sacrificial electron donor. In addition, the Ni_xCd_yS prepared by Cao et al. through the decomposition of a Ni-doped Cd–Co PBA exhibit a 3 times increase in photocatalytic HER activity than pure CdS in the presence of Na_2S/Na_2SO_3 solution as the sacrificial electron donor.[92]

1.5 Thesis Objectives

Understanding the structure-activity relationship of an active site has been a significant approach toward the rational design of a high-performing catalyst for water splitting. Although extensive studies have been performed on the investigation of PBAs as a water splitting catalyst, a clear understanding on the effect of the structural coordination of the catalytic sites on the morphology/electronic properties and the activity of PBAs is yet to be explored to date. To this end, chapters three and four of this thesis focus on manipulating the structural coordination of the catalytic sites in PBAs to enhance the photocatalytic activity (Figure 1.11), using the well-established $[Ru(bpy)_3]^{2+}$ as the photosensitizer.

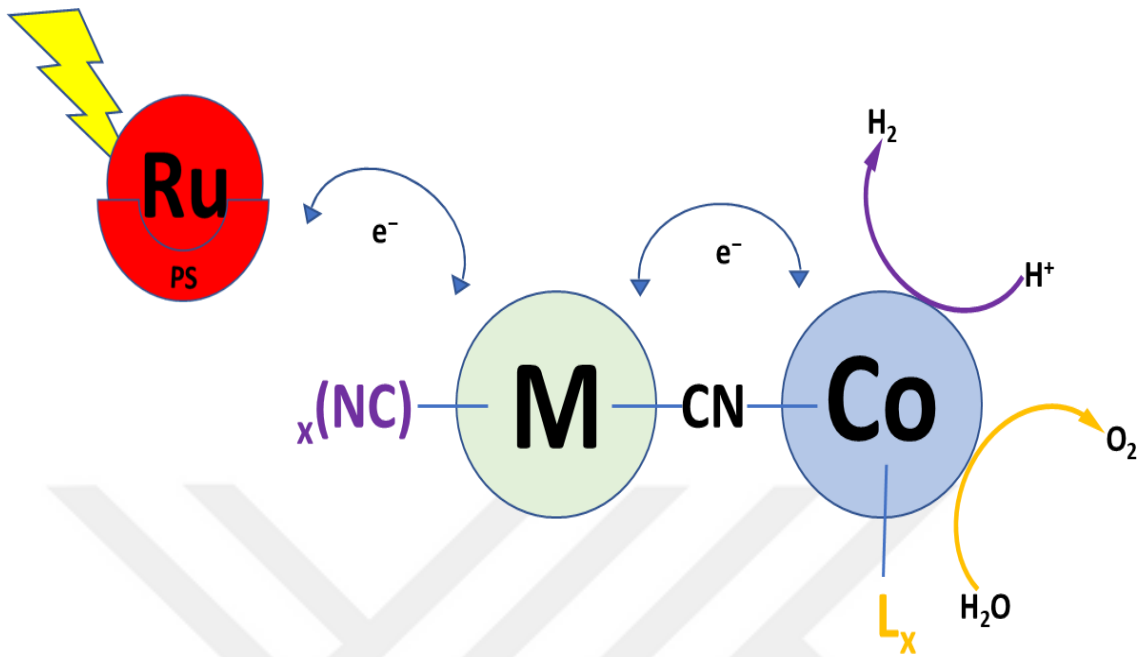

Figure 1.11: Schematic drawing showing (i) the coordination tuning of the metal sites to achieve an ideal catalytic cobalt environment for water oxidation and hydrogen evolution reaction. (ii) electron transfer pathway between $[Ru(bpy)_3]^{2+}$ and the catalytic cobalt site.

Chapter three introduces a simple synthetic approach, referred to as "ligand-engineering", to tune the dimensionality of Co–Fe PBA through the coordination of donor-acceptor bidentate ligands to their catalytic cobalt sites. Experimental and DTF computational investigations revealed the relationship between the well-defined ligand environment of the catalytic sites and water oxidation activity.

Chapter four presents the first application of a 2D layered cyanide coordination polymer for photocatalytic hydrogen evolution reaction. This work elucidates the effect of changing the precursor units from the typical $[Fe(CN)_6]^{3-}$ to a square planar $[Ni(CN)_4]^{2-}$ on the morphology, structural environment, electronic features, and catalytic properties of the active sites.

CHAPTER 2

2.0 EXPERIMENTAL

2.1 Chemicals and Reagents

Cobalt(II) nitrate hexahydrate $Co(NO_3)_2.6H_2O$ (Carlo-Erba, ≥ 95%), Zinc(II) nitrate hexahydrate $Zn(NO_3)_2.6H_2O$ (Sigma-Aldrich, ≥ 98%), Potassium hexacyanoferrate(III) $K_3Fe(CN)_6$ (Sigma-Aldrich, ≥ 99%), Potassium hexacyanocobaltate(III) $K_3Co(CN)_6$ (Sigma-Aldrich, ≥ 97%), Potassium tetracyanonickelate(II) hydrate $K_2Ni(CN)_4{\cdot}xH_2O$ (Sigma-Aldrich, ≥ 98%), Tris(2,2'-bipyridyl)dichlororuthenium(II) hexahydrate $[Ru(bpy)_3]Cl_2{\cdot}6H_2O$ (Alfa-Aesar, ≥ 98%), Sodium hydroxide NaOH (Sigma-Aldrich, 98–100.5%), Trifluoroacetic acid CF_3COOH (Merck, ≥ 99%), 2,2'-bipyridine (Sigma-Aldrich, ≥ 97%), 1,10-phenanthroline (Sigma-Aldrich, ≥ 97%), Ascorbic acid $C_6H_8O_6$ (Carlo-Erba, ≥ 95%), Acetone (Sigma-Aldrich, ≥ 97%) and Methanol (Sigma-Aldrich, ≥ 97%) were purchased and used without any further purifications. All the solutions were prepared with Milli Q deionized water (resistivity: 18 MΩ.cm).

2.2 Synthesis of PBAs

$K_{0.1}Co_{2.9}[Fe(CN)_6]_2 \cdot 12H_2O$, [Co–Fe]. A 50 mL aqueous solution of 0.75 mmol of $Co(NO_3)_2.6H_2O$ was added drop-wisely to an equal volume of an aqueous solution of 0.5 mmol of $K_3Fe(CN)_6$ under constant stirring. The resulting solution was stirred vigorously for 2 hours, centrifuged, washed with deionized water, and dried in the oven at 60°C to obtain a brown powder. Anal. Calcd. (%) for $C_{12}H_{24}N_{12}O_{12}K_{0.1}Co_{2.9}Fe_2$: C, 17.69; H, 2.94; N, 20.61. Found: C, 17.19; H, 2.84; N, 19.52. EDX Co/Fe atomic ratio: 3/2.

Well-defined cubic shape Co–Fe PBA were synthesized following a previously reported method with slight changes.[93] Briefly, A 50 mL aqueous solution of 0.75 mmol of $Co(NO_3)_2.6H_2O$ and an equal volume of an aqueous solution of 0.5 mmol of $K_3Fe(CN)_6$ under were added simultaneously at a drop-wise rate to 100 mL of de-ionized water under constant stirring at room temp. After complete addition, the resulting solution was stirred vigorously for an additional 1 hour and allowed to stand overnight. Then, the obtained brown precipitate was centrifuged, washed with de-ionized water, and dried in the oven at 60 °C.

$K_{0.1}Co_{2.9}[Co_2(CN)_6]_2 \cdot 14.5H_2O$, [Co–Co]. A 50 mL aqueous solution of 0.75 mmol of $Co(NO_3)_2.6H_2O$ was added drop-wisely to an equal volume of an aqueous solution of 0.5 mmol of $K_3Co(CN)_6$ under constant stirring. The resulting solution was stirred vigorously for 2 hours and allowed to stand overnight. Then, the obtained pink precipitate was centrifuged, washed with de-ionized water, and dried in the oven at 60 ^oC. Anal. Calcd. (%) for $C_{12}H_{29}N_{12}O_{14.5}K_{0.1}Co_{4.9}$: C, 16.63; H, 3.35; N, 19.40. Found: C, 16.82; H, 3.03; N, 19.49.

$Co[Ni(CN)_4] \cdot 2.3H_2O$, [Co–Ni]. A 50 mL aqueous solution of 0.5 mmol of $Co(NO_3)_2.6H_2O$ was added drop-wisely to an equal volume of an aqueous solution of 0.5 mmol of $K_2Ni(CN)_4 \cdot xH_2O$ under constant stirring. The resulting solution was stirred vigorously for 2 hours, allowed to stand overnight, centrifuged, washed with de-ionized water, and dried in the oven at 60 ^oC. A light-magenta precipitate that turned purple upon drying was obtained. Anal. Calcd. (%) for $C_4H_{4.6}N_4O_{2.3}CoNi$: C, 18.24; H, 1.75; N, 21.28. Found: C, 18.31; H, 1.69; N, 21.49. EDX Co/Ni atomic ratio: 1/1.

$Zn[Ni(CN)_4] \cdot 0.4H_2O$, [Zn–Ni]. A 25 mL aqueous solution of 0.5 mmol of $Zn(NO_3)_2.6H_2O$ was added drop-wisely to an equal volume of an aqueous solution of 0.5 mmol of $K_2Ni(CN)_4 \cdot xH_2O$ under constant stirring. The resulting solution was stirred vigorously for 2 hours and allowed to stand overnight. Then, the obtained white precipitate was centrifuged, washed with de-ionized water, and dried in the oven at 60 ^oC. Anal. Calcd. (%) for $C_4H_{0.8}N_4O_{0.4}ZnNi$: C, 20.40; H, 0.34; N, 23.80. Found: C, 20.24; H, 0.34; N, 23.52. EDX Zn/Ni atomic ratio: 1/1.

2.3 Synthesis of Cobalt Precursors

mono(2,2'-bipyridine)dichlorocobalt(II), $CobpyCl_2$. 2 mmol of 2,2'-dipyridyl in 20 ml of acetone was mixed with a solution containing 2 mmol anhydrous cobalt (II) chloride in 20 ml of acetone. The resulting solution was stirred for two hours, filtered, and dried in a desiccator to obtain a light-blue precipitate. Yield: 486.5 mg (85%). Anal. Calcd. (%) for $C_{10}H_8N_2Cl_2Co$: C, 41.94; H, 2.78; N, 9.79. Found: C, 43.27; H, 2.86; N, 9.96.

mono(1,10-phenanthroline)dichlorocobalt(II), $CophenCl_2$. 2 mmol of 1,10-phenanthroline monohydrate in 20 ml of acetone was mixed with a solution containing 2 mmol anhydrous cobalt (II) chloride in 20 ml of acetone. The resulting solution was stirred for two hours, filtered, and

dried in a desiccator to obtain a blue precipitate. Yield: 600.8 mg (85%). Anal. Calcd. (%) for $C_{12}H_8N_2Cl_2Co$: C, 46.43; H, 2.58; N, 9.02. Found: C, 47.22; H, 2.85; N, 8.79.

bis(2,2'-bipyridine)dichlorocobalt(II), Cobpy$_2$Cl$_2$. 4 mmol of 2,2'-dipyridyl in 20 ml of acetone was mixed with a solution containing 2 mmol anhydrous cobalt (II) chloride in 20 ml of acetone. The resulting solution was stirred for two hours, filtered, and dried in a desiccator to obtain an orange-red precipitate. Yield: 817 mg (90%). Anal. Calcd. (%) for $C_{20}H_{16}N_4Cl_2Co$: C, 54.26; H, 3.62; N, 12.66. Found: C, 53.50; H, 3.52; N, 12.45.

bis(1,10-phenanthroline)dichlorocobalt(II), Cophen$_2$Cl$_2$. 4 mmol of 1,10-phenanthroline monohydrate in 20 ml of acetone was mixed with a solution containing 2 mmol anhydrous cobalt (II) chloride in 20 ml of acetone. The resulting solution was stirred for two hours, filtered, and dried in a desiccator to obtain a red precipitate. Yield: 1065.5 mg (90%). Anal. Calcd. (%) for $C_{24}H_{16}N_4Cl_2Co$: C, 58.73; H, 3.26; N, 11.42. Found: C, 57.88; H, 3.19; N, 11.19.

2.4 Synthesis of Ligand-Engineered PBAs

All the ligand-engineered cyanide-bridged complexes used as catalysts were prepared using a similar method. Therefore, only the synthesis of **[Cobpy–Fe]** will be discussed in detail.

$K_{0.1}$[Co(bpy)]$_{2.9}$[Fe(CN)$_6$]$_2$ .7.5H$_2$O, [Cobpy–Fe]. 20 mL aqueous solution of CobpyCl_2 (0.6 mmol) was added to 20 mL aqueous solution of $K_3Fe(CN)_6$ (0.4 mmol). The resulting solution was stirred for one hour and allowed to stand overnight. Then, the obtained green precipitate was centrifuged, washed, and dried in the oven at 50°C for approximately 20 hours. Yield: 285 mg (60%). Anal. Calcd. (%) for $C_{41}H_{38.2}N_{17.8}O_{7.5}K_{0.1}Co_{2.9}Fe_2$: C, 41.45; H, 3.21; N, 20.99. Found: C, 41.84; H, 2.85; N, 20.16. EDX Co/Fe atomic ratio: 3/2.

$K_{0.2}$[Co(phen)]$_{2.8}$[Fe(CN)$_6$]$_2$ .7.5H$_2$O, [Cophen–Fe]. CophenCl_2 was used as the cobalt precursor and a similar procedure as **[Cobpy–Fe]** was followed to obtain a green precipitate. Yield: 256 mg (52%). Anal. Calcd. (%) for $C_{42}H_{37.4}N_{17.6}O_{7.5}K_{0.2}Co_{2.8}Fe_2$: C, 44.25; H, 3.02; N, 19.92. Found: C, 43.17; H, 2.80; N, 18.98. EDX Co/Fe atomic ratio: 3/2.

{[Co(bpy)$_2$]$_3$[Fe(CN)$_6$]$_2$}[Fe(CN)$_6$]$_{1/3}$.14.5H$_2$O, [Cobpy2–Fe]. Cobpy$_2$Cl$_2$ was used as the cobalt precursor and a similar procedure as **[Cobpy–Fe]** was followed to obtain a blue precipitate. Yield:

348 mg (55%). Anal. Calcd. (%) for $C_{74}H_{53}N_{26}O_{29}Co_3Fe_{2.3}$: C, 47.49; H, 4.06; N, 19.47. Found: C, 46.08; H, 3.72; N, 18.53. EDX Co/Fe atomic ratio: 3/2.4.

$\{[Co(phen)_2]_3[Fe(CN)_6]_2\}[Fe(CN)_6]_{1/3}Cl_{0.11}.17.5H_2O$, [Cophen2–Fe]. $Cophen_2Cl_2$ was used as the cobalt precursor and a similar procedure as **[Cobpy–Fe]** was followed to obtain a light–blue precipitate. Yield: 413 mg (59%). Anal. Calcd. (%) for $C_{86}H_{59}N_{26}O_{35}Cl_{0.11}Co_3Fe_{2.3}$: C, 49.81; H, 4.01; N, 17.57. Found: C, 47.58; H, 3.23; N, 17.28. EDX Co/Fe atomic ratio: 3/2.3.

2.5 Instrumentation

2.5.1 Fourier Transform Infrared Spectroscopy (FTIR)

FTIR spectra were recorded on Bruker Alpha Platinum–ATR Spectrometer model. The spectra were recorded in transition mode within the wavenumber range of 400 – 4000 cm^{-1} for 64 scans.

2.5.2 UV-Vis Spectroscopy

UV-Vis absorption spectra of the solutions were obtained on an Agilent Cary 5000 UV–Vis-NIR spectrophotometer, using a quartz cuvette with a path length of 1 cm.

2.5.3 Diffuse-reflectance UV-Vis Spectroscopy

The UV-Vis absorption spectra of insoluble powder samples were obtained on an Agilent Cary 5000 UV–Vis-NIR spectrophotometer equipped with a diffuse reflectance accessory. The samples were measured within the wavelength range of 250 – 800 nm.

2.5.4 Thermogravimetric Analysis (TGA)

Thermogravimetric analysis (TGA) was carried out on a Q500 thermogravimetric analyzer within the temperature range of 28 ºC to 800 ºC operating under a nitrogen atmosphere at a heating rate of 5 ºC min^{-1}.

2.5.5 CHN Elemental Analysis

The elemental analysis of carbon, hydrogen and nitrogen was carried out on Thermo Scientific FLASH 2000 Series CHNS/O elemental analyzer. The measurements were performed using 2,5-Bis(5-tert-butyl-benzoxazol-2-yl) thiophene (BBOT) as a standard and V_2O_5 as a catalyst.

2.5.6 X-ray Photoelectron Spectroscopy (XPS)

XPS analysis was performed on Thermo Fisher Scientific K–Alpha X-ray photoelectron spectrometer, using Al Kα micro-focused monochromator as the X-ray source and equipped with a flood gun for charge neutralization. All peaks were shifted with reference to C 1s peak position (284.8 eV).

2.5.7 Powder X-ray Diffraction (PXRD)

PXRD patterns were obtained using a PANalytical X'pert PRO X-ray diffractometer using Cu Kα radiation (1.5406 Å). The diffraction patterns were recorded in the 2θ diffraction angle within the range of 5 – 80º, using a step size of 0.02.

2.5.8 Transmission Electron Microscopy (TEM)

TEM was performed on FEI Tecnai G2 F20 X-TWIN. The TEM samples were prepared by dropping 3 μL of the sample solution (2mg of sample dispensed into 1 mL methanol/water (1:1) mixture) onto the cupper grid (carbon film, 400 mesh).

2.5.9 Scanning Electron Microscopy (SEM) and Energy Dispersive X-ray (EDX)

SEM was performed on FEI QUANTA 200 FEG ESEM operating at a beam voltage of 5 kV and a spot size of 3.0. The SEM powder samples were coated with Pt/Pd before measurements to make them conductive. The SEM instrument is equipped with an Ametek EDAX Energy Dispersive X-ray (EDX) system for elemental composition analysis. The instrument is operated at a beam voltage of 15 kV and a spot size of 5.0 during EDX analysis.

2.6 Electrochemistry

2.6.1 Electrochemical measurements

Electrochemical experiments were carried out on a Gamry Instruments Interface 1000 potentiostat/galvanostat at 25 ºC. Using the conventional three-electrode setup, with Pt mesh as the counter electrode, Ag/AgCl (3.5 M KCl) as the reference electrode, and fluorine-doped tin oxide (FTO) coated electrode (~80% transmittance; 2 mm slides with 7 $\Omega \cdot sq^{-1}$ surface resistivity and 1 × 2 cm size) as the substrate for working electrode.

Cyclic voltammetry experiments were performed at different scan rates (25 − 250 $mV \cdot s^{-1}$) to obtain the surface concentration (Γ) of active cobalt sites from the electrochemical linear plot of the peak current (I_p) of the Co^{3+}/Co^{2+} reduction wave versus the scan rate (ν).[68]

Electrocatalytic HER activity was evaluated by linear sweep voltammetry experiments performed in a potassium phosphate buffer (KPi) solution at pH 7 containing 1 M KNO_3 as the supporting electrolyte.

2.6.2 Working Electrode Preparation

1 × 2 cm FTO electrode was used as the working electrode, but only 1 × 1 cm of the conducting surface was coated with the catalyst. Prior to coating the FTO surface, the electrode was adequately cleaned by sonicating for 10 mins in a basic soapy solution, deionized water, and isopropanol, then annealed at 350 ºC in the furnace for 30 mins. After activation, the surface of FTO was coated with the catalyst using two different methods:

(i) Drop-casting method: Briefly, 5 mg of the catalyst was added to a mixture of ethanol (400 µL), de-ionized water (100 µL) and Nafion solution (10 µL; 5 wt%), and then the solution was sonicated for 30 min to obtain a uniform ink. Finally, 5 µL of the obtained ink was drop-casted on the FTO surface, air-dried and kept in the desiccator until measurement.

(ii) Two-step *in situ* method: Briefly, 1,000 µL of 0.05 M aqueous solution of hexacyanoferrate was spin-coated on FTO at 500 rpm for 150 seconds, air-dried, and dipped into a 0.075 M aqueous solution of Co^{2+} precursor for 15 min. This procedure was repeated three times. Finally, the electrode was dried in the oven at 60 °C for about 10 min., washed with deionized water, air-dried, and kept in the desiccator until ready for use.

2.7 Photocatalysis

2.7.1 Photocatalytic OER experiment

Photocatalytic experiments were conducted in a Pyrex flask totally sealed with a septum. A 30 mL 0.1 M potassium phosphate buffer solution (PBS) containing 10 mg catalyst, 5 mM sodium persulfate ($Na_2S_2O_8$), and 1 mM ruthenium photosensitizer ($[Ru(bpy)_3]Cl_2$) were prepared. PBS was prepared by mixing aqueous solutions of KH_2PO_4 (0.1 M) and K_2HPO_4 (0.1 M). The Pyrex flask was covered with aluminum foil before adding the ruthenium complex to prevent

an early light-induced reaction. Initially, the mixture was purged with N_2 gas thoroughly for 25–30 min. The photocatalytic experiment was carried out for 1 hour, and the amount of oxygen evolved was determined by injecting 100 μL of the headspace gas at a 15-minute interval into a gas chromatograph (Agilent 7820 A, a gas chromatograph equipped with a molecular sieve and a thermal conductivity detector (TCD), using argon as the carrier gas). The experiment was conducted at least twice for each catalyst to obtain a reproducible result.

2.7.2 Photocatalytic HER experiment

Photocatalytic experiments were performed in a Pyrex flask sealed with a septum. 1 – 10 mg catalyst and 1 mM ruthenium photosensitizer ($[Ru(bpy)_3]Cl_2$) were dispersed into a 10 mL aqueous solution of 0.1 M ascorbic acid (pH 5). The pH of the ascorbic acid solution was adjusted using a 3 M NaOH solution. The Pyrex flask was covered with an aluminum foil before adding the ruthenium complex to prevent an early light-induced reaction. Prior to light irradiation, the mixture was purged with N_2 gas thoroughly for 25 – 30 mins. The photocatalytic experiment was carried out for 3 hours, and the amount of hydrogen gas evolved was determined by injecting 100 μL of the headspace gas at 1–hour interval into a gas chromatograph (Agilent 7820 A, a gas chromatograph equipped with a molecular sieve and a thermal conductivity detector (TCD), using argon as the carrier gas). The experiment was carried out at least twice for each catalyst to obtain a reproducible result.

2.7.2.1 Cycle HER experiments

Before starting a new cycle, the solution containing the used catalyst was centrifuged and washed with deionized water. Then, it is suspended in a fresh solution containing ruthenium photosensitizer and ascorbic acid. The solution is purged with N_2 gas thoroughly for 25 – 30 mins, and the experiment is continued for another 3 hours.

CHAPTER 3.

3.0 LIGAND-ENGINEERED PRUSSIAN BLUE ANALOGUES FOR PHOTOCATALYTIC WATER OXIDATION

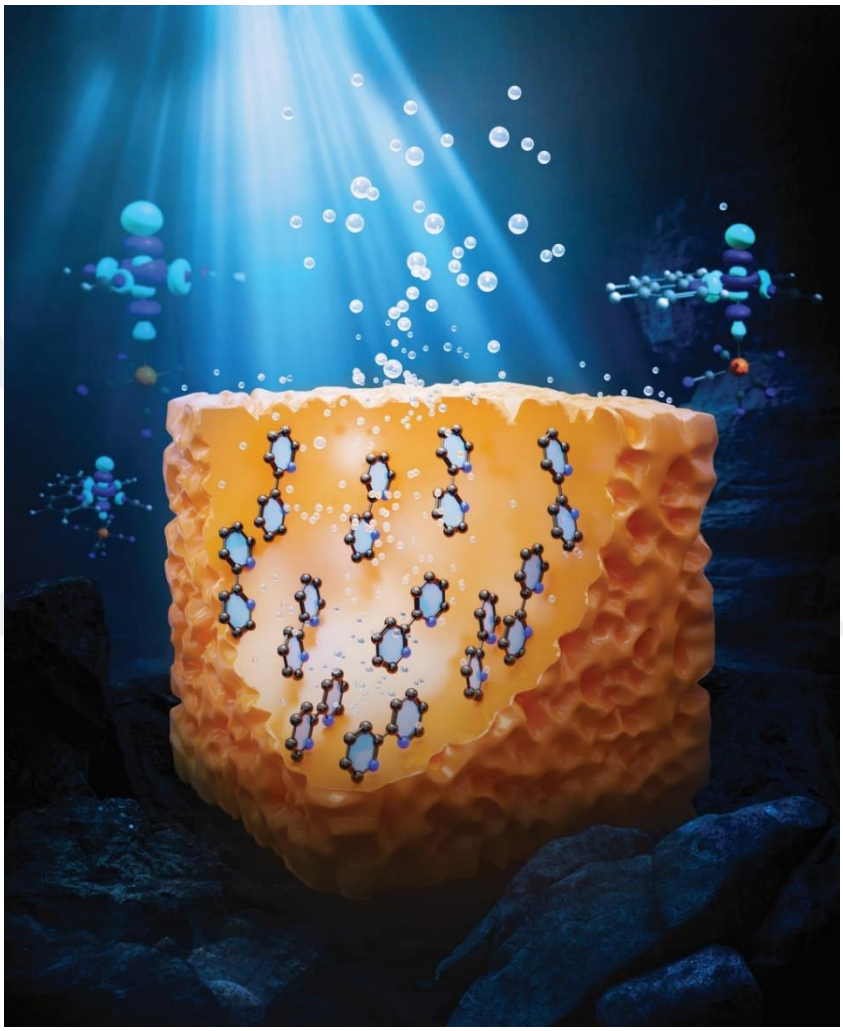

3.1 Preface

This chapter of the thesis is based on the publication "Ahmad, A. A.; Ghobadi, T. G. U.; Buyuktemiz, M.; Ozbay, E.; Dede, Y.; Karadas, F. Light-Driven Water Oxidation with Ligand-Engineered Prussian Blue Analogues". **Inorg. Chem.** 2022, 61, 3931− 3941. Adapted (or "Reproduced in part") with permission from Ref. [70]. Copyright 2022. American Chemical Society.

3.2 Introduction

Water oxidation is considered to be the crucial half of water splitting because of the slow kinetics caused by the multi-electron/proton transfer steps, the critical rate-determining O–O bond formation, and a large overpotential is often required to achieve a high performance in water oxidation. The benchmark noble IrO_2 and RuO_2 catalysts have limited use in practical applications due to their less abundance and high cost. Therefore, extensive research efforts have been devoted to replacing these noble catalysts with low-cost, abundant and highly efficient ones. CoFe Prussian blue analogues (Co–Fe PBA) are highly ranked as one of the alternatives for the noble catalyst due to their simple synthetic methodology, impressive stability, tuneable metal sites and fast electron transfer from Fe to catalytic Co sites through the short cyanide bridge. Several methods have been reported to tune the activity of Co–Fe PBA; however, the methods reported so far to directly tune the catalytic cobalt site usually lead to a decomposition of the cyanide framework and reconstruction into its corresponding oxides, phosphides, and chalcogenides.

Herein, using a simple synthetic strategy, we designed the catalytic cobalt sites of Co–Fe PBA with bidentate pyridyl ligands. A series of characterization techniques confirms the preservation of the cyanide coordination environment. Finally, we showed a relationship between the well-defined catalytic ligand environment and activity using experimental photocatalytic studies and computational DFT calculations.

3.3 Results and Discussions

3.3.1 Synthesis

We first prepared the cobalt precursors by coordinating appropriate equivalent bpy or phen ligands to the cobalt sites, following a previously existing protocol.[94], [95] Complexation of one equivalent of bidentate ligand to the cobalt sites gave the desired $CobpyCl_2$ and $CophenCl_2$ at a high yield, while coordination of two equivalents bidentate ligands to the cobalt sites generated $Cobpy_2Cl_2$ and $Cophen_2Cl_2$ with a good yield. A visible colour change was observed upon complexation. The UV-Vis spectra of the cobalt precursors are shown in Figure 3.1a, an MLCT band (~475 nm) which is caused by the electron transfer from the d–orbital of the Co to the π^*–orbital of the ligands, is evident in the visible region, while the ligands π–π^* and n–π^* transitions are responsible for the remaining bands below 350 nm.[96] The absorption spectra of

$CobpyCl_2$ and $CophenCl_2$ are similar in the visible region, indicating that a cobalt complex with one pyridyl ligand is effectively produced. $Cobpy_2Cl_2$ and $Cophen_2Cl_2$ follow a similar pattern. The synthesis of the cobalt precursors was also verified using FTIR spectroscopy (Figure 3.1b,c), the bands in the fingerprint region correspond well with the bpy and phen ligands (Table 3.1), with a minor shift confirming the complexation with cobalt.

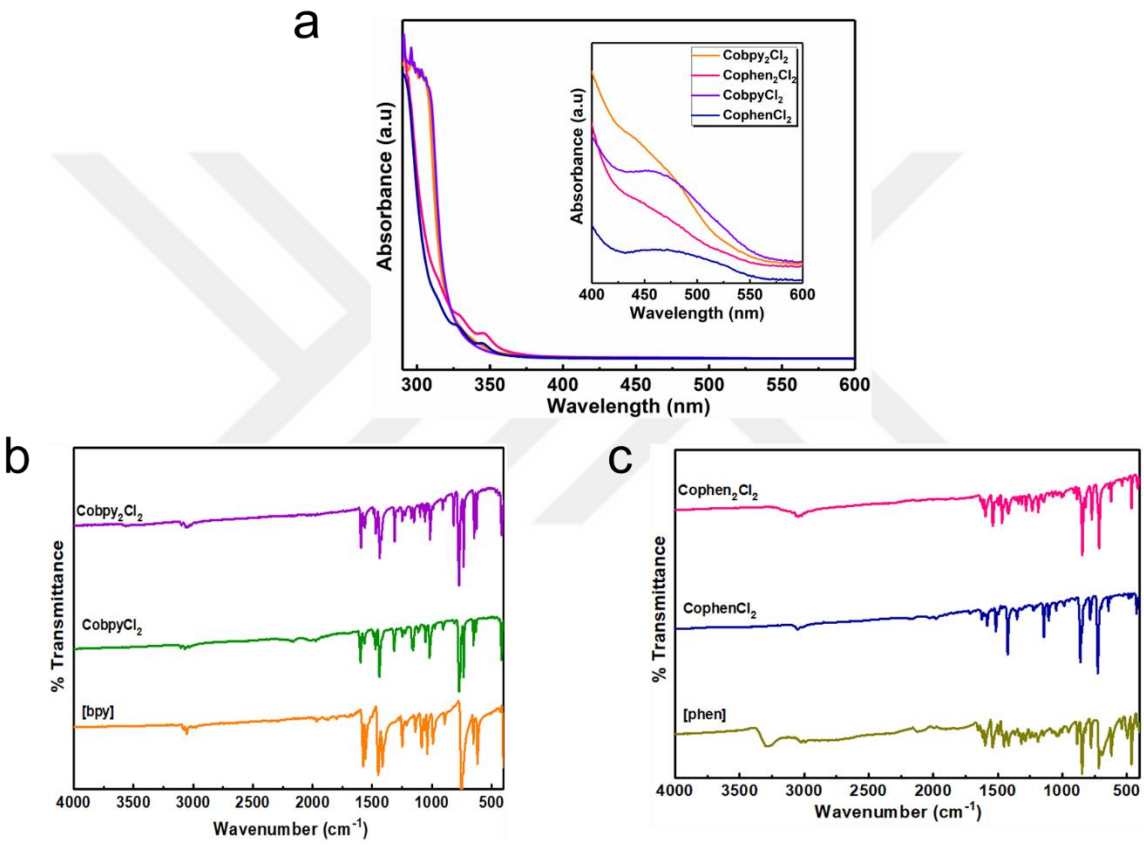

Figure 3.1: (a) UV-Vis absorption spectra of an aqueous solution of $CobpyCl_2$, $Cobpy_2Cl_2$, $CophenCl_2$, and $Cobpy_2Cl_2$. Inset: absorption bands in the visible region of the spectra (400 – 600 nm). (b) FTIR spectra of bipyridine (bpy) and their corresponding cobalt bipyridine precursors. (c) FTIR spectra of phenanthroline (phen) and their corresponding cobalt phenanthroline precursors.

After the synthesis of the cobalt precursors, all the compounds used as catalysts (**[Co–Fe]**, **[Cobpy–Fe]**, **[Cophen–Fe]**, **[Cobpy2–Fe]**, and **[Cophen2–Fe]**) were prepared by reacting three equivalents of cobalt precursor with two equivalents of hexacyanoferrate precursor in a co-precipitation method (Figure 3.2).

Table 3.1: IR bands on the cobalt precursors and their assignments.

IR bands (cm^{-1})	Assignment
2,900 – 3,100	C–H stretch
~1,600	C=N/C=C stretch
~1,200	C–C/C–N bend
~750 – 1,000	aromatic C–H vibrations

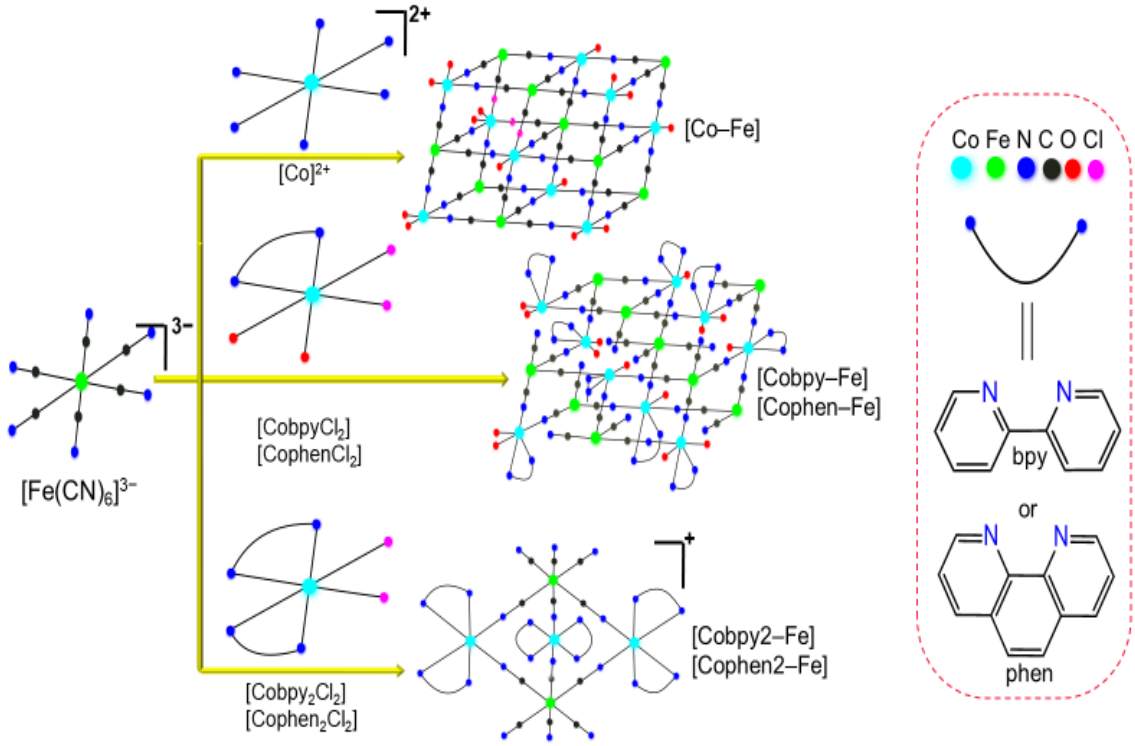

Figure 3.2: Schematic illustration for the synthesis and structural units of compounds: All five compounds are derived from the same precursor, $K_3Fe(CN)_6$. The resulting cyanide coordination compounds differ in their Co precursors; (top) 3D crystalline **[Co–Fe]**, (middle) low-dimensional **[Cobpy–Fe]** and **[Cophen–Fe]**, and (bottom) molecular **[Cobpy2–Fe]** and **[Cophen2–Fe]** compounds. The curved lines represent bpy and phen ligands framed by the blue circles. Reprinted with permission from Ref. [70]. Copyright 2022. American Chemical Society.

3.3.2 Catalysts Characterization

3.3.2.1 SEM-EDX

At a magnification of 10 µm, SEM images demonstrate that **[Co–Fe]** has a different surface topography than the other compounds (Figure 3.3). **[Co–Fe]** semi-cube-like crystal in agglomerated form. Whereas **[Cobpy–Fe]** and **[Cophen–Fe]** exhibit amorphous nature with a rough surface. The morphology of **[Cobpy2–Fe]** and **[Cophen2–Fe]** show aggregation into clusters.

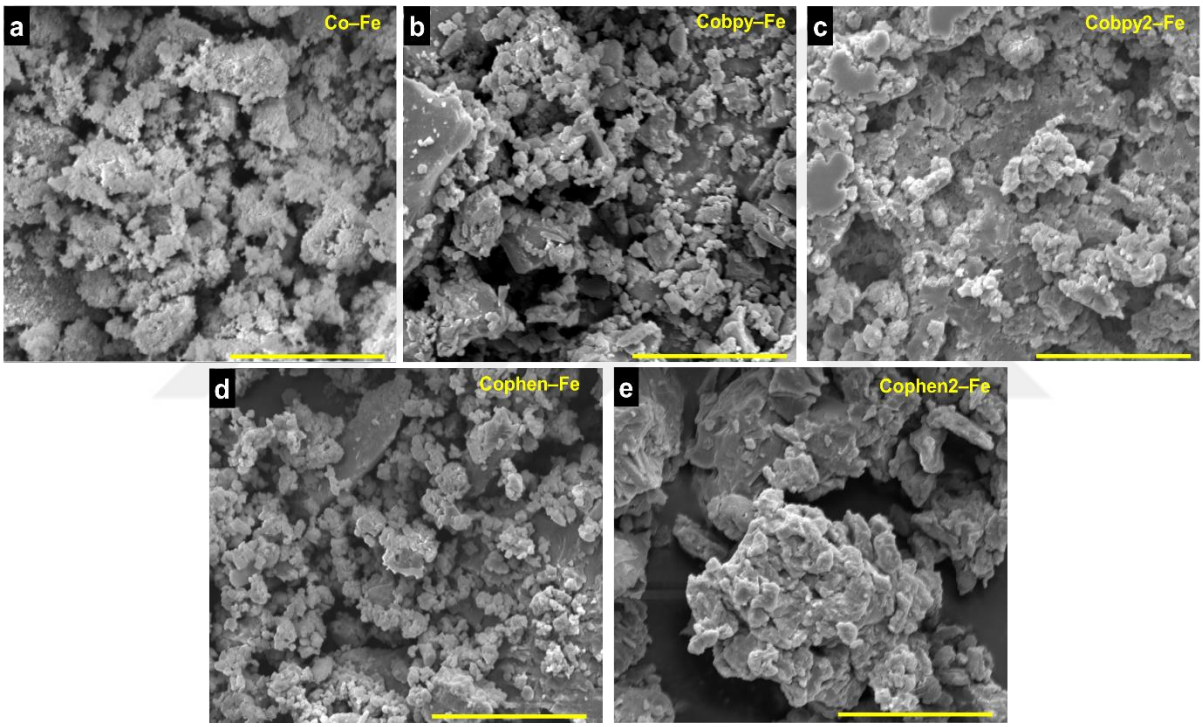

Figure 3.3: SEM micrographs of (a) **[Co–Fe]**, (b) **[Cobpy–Fe]**, (c) **[Cobpy2–Fe]**, (d) **[Cophen–Fe]**, and (e) **[Cophen2–Fe].** Scale bar: 10 µm. Reprinted with permission from Ref. [70]. Copyright 2022. American Chemical Society.

EDX elemental analysis revealed the atomic ratio of all the elements in the compound as shown in Table 3.2. The Co:Fe atomic ratio of 3 to 2 is confirmed by EDX evaluation.

Table 3.2: EDX elemental analysis of CoFe compounds and their obtained chemical formulas.

Compound	EDX Atomic %							TGA	Chemical Formula
	Co	Fe	C	N	O	K	Cl	%Water molecule	
[Co–Fe]	2.91	2.01	58.5	28.28	7.43	0.1	–	26.58	$K_{0.1}Co_{2.9}[Fe(CN)_6]_2 \cdot 12H_2O$
[Cobpy–Fe]	2.97	2.04	68.62	23.7	1.94	0.31	–	11.87	$K_{0.1}[Co(bpy)]_{2.9}[Fe(CN)_6]_2 \cdot 7.5H_2O$
[Cophen–Fe]	3.63	2.6	70.21	21.44	1.06	0.53	–	11.34	$K_{0.2}[Co(phen)]_{2.8}[Fe(CN)_6]_2 \cdot 7.5H_2O$
[Cobpy2–Fe]	1.79	1.47	68.13	27.61	0.55	–	–	14.32	$\{[Co(bpy)_2]_3[Fe(CN)_6]_2\}[Fe(CN)_6]_{1/3} \cdot 14.5H_2O$
[Cophen2–Fe]	2.11	1.65	75.79	18.09	1.13	–	0.62	15.48	$\{[Co(phen)_2]_3[Fe(CN)_6]_2\}[Fe(CN)_6]_{1/3}Cl_{0.11} \cdot 17.5H_2O$

3.3.2.2 TGA

Thermogravimetric analysis was used to determine the number of water molecules contained in each compound (Figure 3.4). The loss of coordinated and non-coordinated water molecules is attributed to the thermal event from 30 ^{o}C to 175 ^{o}C, while the rest of the thermal decomposition at temperatures above 250 ^{o}C is due to the decomposition and reconstruction of the cyanide network to oxides.[97] The combination of TGA and EDX elemental analysis was used to determine the chemical formula of the compound as shown in Table 3.2.

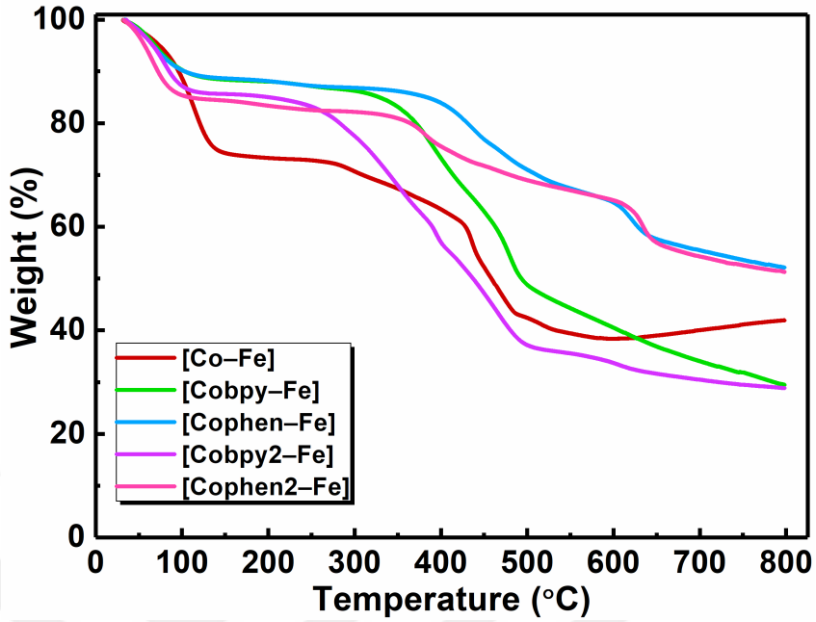

Figure 3.4: Thermogravimetric curves of CoFe compounds. Reprinted with permission from Ref. [70]. Copyright 2022. American Chemical Society.

3.3.2.3 CHN elemental analysis

CHN elemental analysis was used to ascertain the as-derived chemical formula of the compounds. As shown in Table 3.3, the elemental ratio of carbon, hydrogen and nitrogen revealed by CHN analysis accord with those calculated from the chemical formula.

Table 3.3: CHN elemental analysis of the CoFe compounds.

Compound	Chemical Formula	Calculated / Found (CHN)		
		%C	%N	%H
[Co–Fe]	$K_{0.1}Co_{2.9}[Fe(CN)_6]_2 \cdot 12H_2O$	17.69 / 17.19	20.61 / 19.52	2.94 / 2.84
[Cobpy–Fe]	$K_{0.1}[Co(bpy)]_{2.9}[Fe(CN)_6]_2 \cdot 7.5H_2O$	41.45 / 41.04	20.99 / 20.16	3.21 / 2.85
[Cophen–Fe]	$K_{0.2}[Co(phen)]_{2.8}[Fe(CN)_6]_2 \cdot 7.5H_2O$	44.25 / 43.17	19.92 / 18.98	3.02 /2.80
[Cobpy2–Fe]	$\{[Co(bpy)_2]_3[Fe(CN)_6]_2\}[Fe(CN)_6]_{1/3} \cdot 14.5H_2O$	47.49 / 46.08	19.47 / 18.53	4.06 / 3.72
[Cophen2–Fe]	$\{[Co(phen)_2]_3[Fe(CN)_6]_2\}[Fe(CN)_6]_{1/3}Cl_{0.11} \cdot 17.5H_2O$	49.81 / 47.58	17.57 / 17.28	4.01 / 3.23

3.3.2.4 FTIR

The FTIR technique is primarily used to analyze the nature of the cyanide bond and also whether or not the pyridyl groups is retained in these compounds. **[Cobpy–Fe]**, **[Cophen–Fe]**, **[Cobpy2–Fe]**, and **[Cophen2–Fe]** are clearly differentiated from **[Co–Fe]** by the presence of pyridyl bands in the fingerprint area of the FTIR spectra (Figure 3.5a). Distinctive cyanide stretching vibration (υ(CN)) in the 2,000–2,200 cm^{-1} region is observed for the compounds (Figure 3.5b), and the assignment of the bands according to literature is given in Table 3.4.[98]–[100]

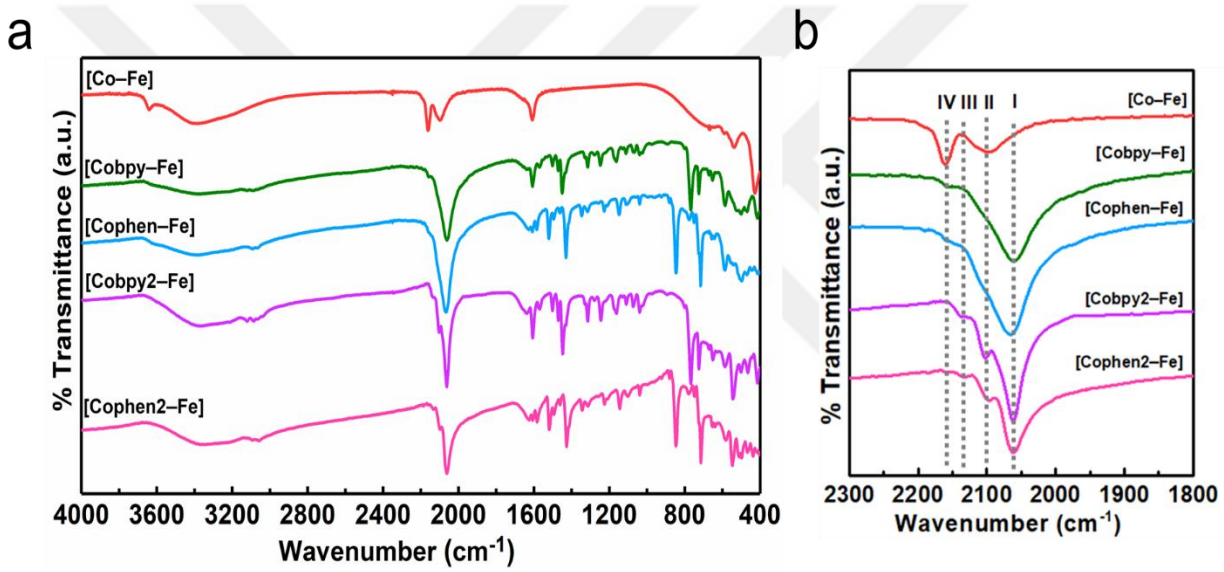

Figure 3.5: ATR-FTIR spectra of CoFe compounds at room temperature showing (a) the full spectrum from 4,000–400 cm^{-1} region. (b) the cyanide stretching region of the compounds with four different assignments: (I) terminal Fe^{2+}–CN, (II) terminal Fe^{3+}–CN & bridging Fe^{2+}–CN–Co^{2+}, (III) bridging Fe^{2+}–CN–Co^{3+}, and (IV) bridging Fe^{3+}–CN–Co^{2+} coordination mode. (b) PXRD patterns of compounds. Reprinted with permission from Ref. [70]. Copyright 2022. American Chemical Society.

Table 3.4: Cyanide stretching frequencies, υ(CN), of the CoFe compounds and their assignments.

Compound	υ(CN) (cm^{-1})	Assignment
[Co–Fe]	2162	Fe^{3+}–CN–Co^{2+}
	2098	Fe^{2+}–CN–Co^{2+}
[Cobpy–Fe]	2058 (very broad)	Fe^{2+}–CN & Fe^{2+}–CN–Co^{3+}
	2156	Fe^{3+}–CN–Co^{2+}
[Cophen–Fe]	2058 (very broad)	Fe^{2+}–CN & Fe^{2+}–CN–Co^{3+}
	2156	Fe^{3+}–CN–Co^{2+}
[Cobpy2–Fe]	2063	Fe^{2+}–CN
	2098	Fe^{3+}–CN
	2135	Fe^{2+}–CN–Co^{3+}
[Cobpy2–Fe]	2063	Fe^{2+}–CN
	2098	Fe^{3+}–CN
	2135	Fe^{2+}–CN–Co^{3+}

3.3.2.5 XRD

The diffraction patterns obtained from PXRD (Figure 3.6) revealed the crystal structure of the synthesized compounds. **[Co–Fe]** display sets of diffraction peaks at 14.77º, 17.30º, 24.56º, 35.02º, and 39.30º which are ascribed to the (111), (200), (220), (400), and (420) reflection planes of a face-centered cubic structure, respectively.[101] The PXRD patterns of **[Cobpy–Fe]** and **[Cophen–Fe]** revealed an amorphous nature with three main broad and weak intensity peaks at 17.63, 25.10, and 35.91, which are attributed to the characteristic (200), (220), and (400) reflection planes of cubic PB. These imply that these compounds are low-dimensional structures. **[Cobpy2–Fe]** has PXRD peaks that perfectly match a reference molecular compound previously described by Berlinguette *et al.* (Figure 3.6b).[102] **[Cobpy2–Fe]** consists of a $\{[Co(bpy)_2]_3[Fe(CN)_6]_2\}^+$ cation and a $[Fe(CN)_6]^{3-}$counter anion. Although **[Cophen2–Fe]** and **[Cobpy2–Fe]** are trigonal bipyramidal compounds (Figure 3.6c),[103] when compared to **[Cobpy2–Fe]**, the position of the

diffraction peaks is somewhat altered and is broader in **[Cophen2–Fe]**, which could be attributable to the variation in ligand size and potentially the type of counter ions.

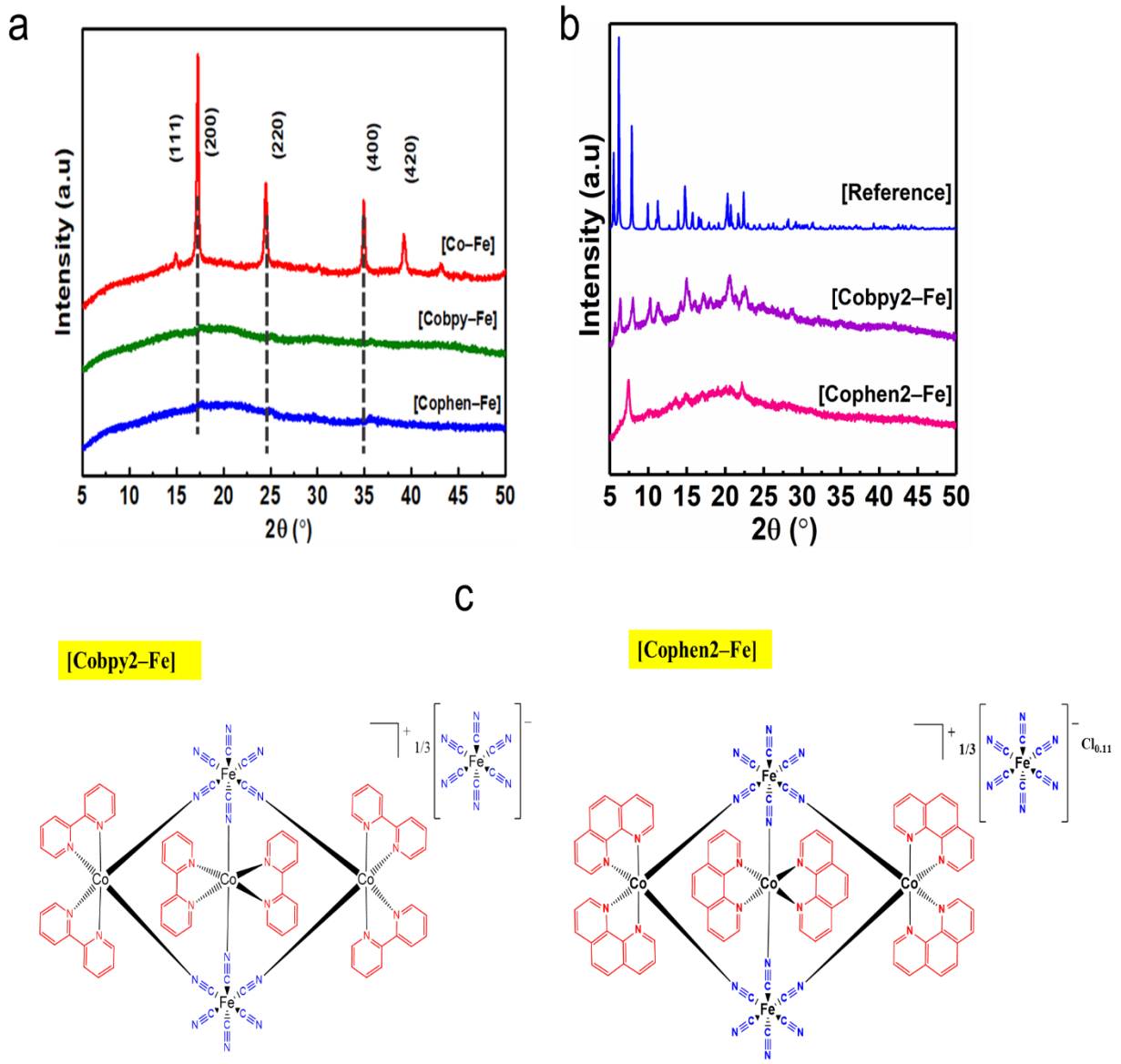

Figure 3.6: (a) PXRD patterns of **[Co–Fe]**, **[Cobpy–Fe]**, and **[Cophen–Fe]**. (b) PXRD patterns of **[Cobpy2–Fe]** and **[Cophen2–Fe]** matched with a reference compound. The reference is a previously synthesized molecular trigonal bipyramidal Co_3Fe_2 cluster $\{[Co(bpy)_2]_3[Fe(C.N.)_6]_2\}[Fe(C.N.)_6]_{1/3}$.[102] (c) Trigonal bipyramidal molecular structures of **[Cophen2–Fe]** and **[Cobpy2–Fe]**. Reprinted with permission from Ref. [70]. Copyright 2022. American Chemical Society.

3.3.2.6 XPS

The chemical composition of the compounds and oxidation states of the transition metals was determined using XPS measurements. As shown in Figure 3.7a-c, The C1s (284.8 eV), N1s (397.9 eV) and O1s (532.4 eV) signals are observed in all the compounds. The presence of C1s and N1s peak is due to the existence of the CN and pyridyl groups, while the O1s signal is assigned to the coordinated and non-coordinated water molecules. The absence of peaks in the 529–530 eV region of the O1s peak suggests no metal-oxide formation in the course of synthesis.[104] As shown in N1s spectra (Figure 3.7b), one peak assigned to the bridging–CN (μ–CN) is allocated to the N1s signal of **[Co–Fe]**. The N1s regions of Co(pyridyl)–Fe compounds, on the other hand, are fitted into three peaks at 396.43 eV, 397.9 eV, and 398.95 eV, respectively, which are attributed to the terminal–CN (CNterm), bridging–CN (μ–CN), and pyridyl–N (N–py). Furthermore, the atomic ratio of the pyridyl–N peak in **[Cobpy2–Fe]** is around two times that of **[Cobpy–Fe]**, implying that there is an increase in the number of coordinated bidentate ligand by twice. The trend for **[Cophen2–Fe]** and **[Cophen–Fe]** follows a similar pattern. The Fe2p signal (~704 – 728 eV) and Co2p signal (~ 775 – 805 eV) are deconvoluted into $2p_{3/2}$ and $2p_{1/2}$ according to spin-orbit coupling (Figure 3.7d and e), and fitted into their appropriate oxidation states according to the literature.[31], [105]

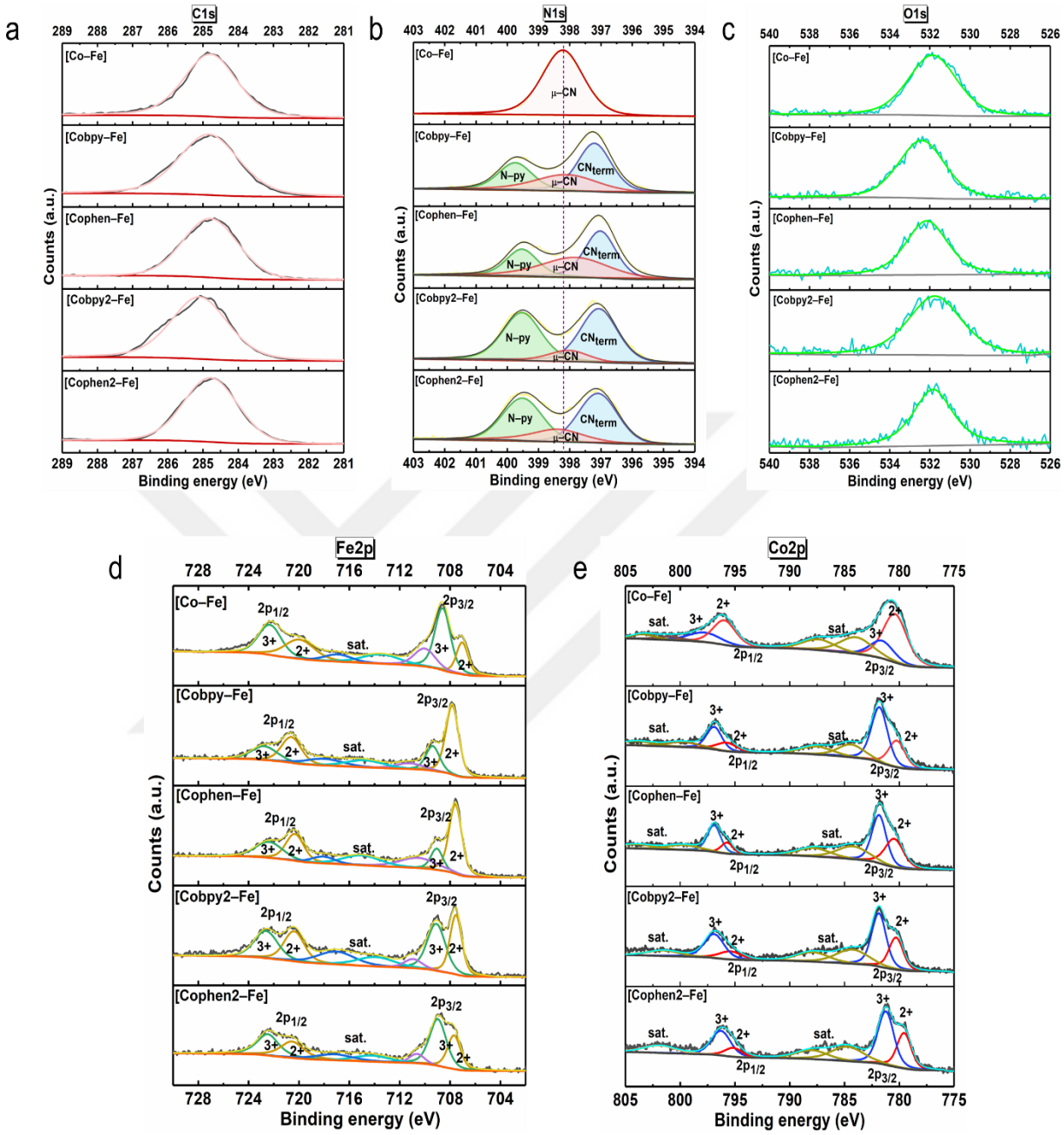

Figure 3.7: High-resolution XPS spectra of (a) C1s, (b) N1s, (c) O1s, (d) Fe2p, and (d) Co2p peaks for the obtained samples. Reprinted with permission from Ref. [70]. Copyright 2022. American Chemical Society.

3.3.3 Photocatalytic Water Oxidation

In a PBS solution, photocatalytic water oxidation experiments were conducted using $[Ru(bpy)_3]Cl_2$ as the photosensitizer and sodium persulfate as the electron scavenger. During a one-hour

photocatalytic experiment (Figure 3.8), **[Cophen–Fe]** and **[Cobpy–Fe]** exhibit the greatest activities of 1,594 μmol g^{-1} h^{-1} and 1,553 μmol g^{-1} h^{-1}, respectively, while **[Co–Fe]** reaches an activity of 1,210 μmol g^{-1} h^{-1} (Figure 3). If all cobalt sites in the compounds are assumed to be active, the lower-bound turnover frequencies (TOF_{lb}) attained were estimated as 4.35×10^{-4} s^{-1}, 3.91×10^{-4} s^{-1}, and 1.73×10^{-4} s^{-1}, for **[Cophen–Fe]**, **[Cobpy–Fe]** and **[Co–Fe]**, respectively, which are comparable to the previously reported ones for PBA-based catalysts.[69], [79] This reveals when pyridyl groups are introduced to the coordination sphere of cobalt sites, their activity rises by at least double.

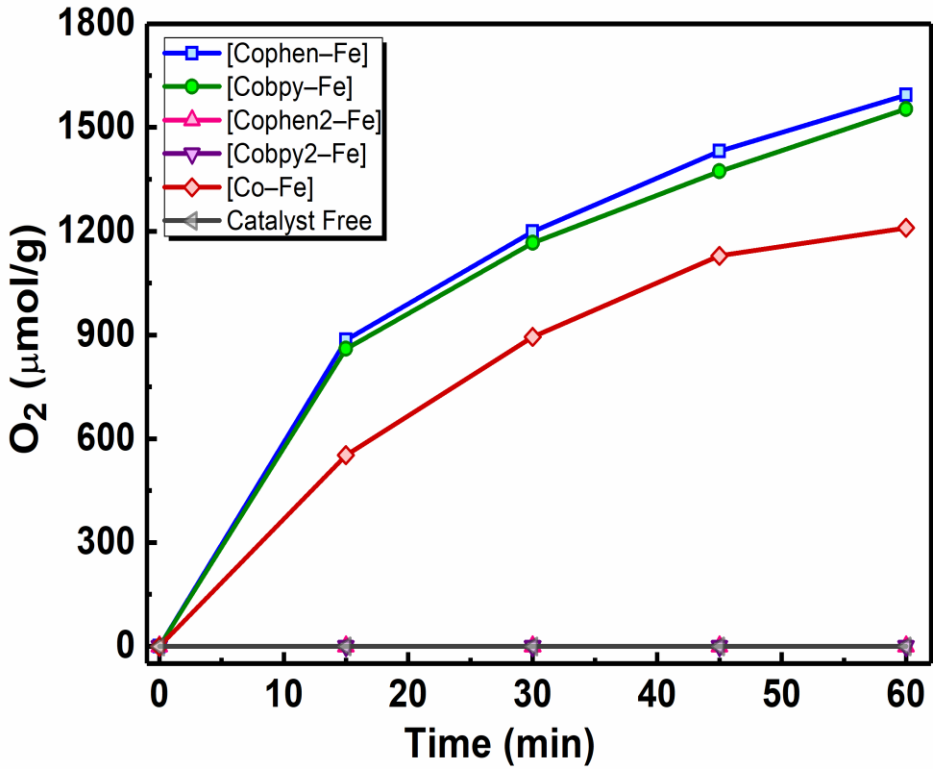

Figure 3.8: Photocatalytic oxygen evolution activities of the compounds in a 0.1 M PBS (pH 7) containing 10 mg catalyst, (7.5 mg) 1 mM $[Ru(bpy)_3]^{2+}$ photosensitizer, and 5 mM $Na_2S_2O_8$ as the sacrificial electron scavenger with a white light source, 100 mW cm^{-2}. Reprinted with permission from Ref. [70]. Copyright 2022. American Chemical Society.

The tuning of electron density of catalytic cobalt sites in **[Cophen–Fe]** and **[Cobpy–Fe]** with electron-withdrawing bidentate pyridyl groups resulted in a 30 percent increase in the catalytic activity. The strong withdrawing ability and stability of the bidentate ligands increase the electrophilicity and susceptibility of the high-valent catalytic Co(IV)–oxo species to the

nucleophilic attack of water for the rate-determining O–O formation.[39], [106] Therefore, by replacing two of the weak –NC ligands around the cobalt sites in **[Co–Fe]** with one equivalent of stronger π-accepting phen and bpy ligands favors enhancement in catalytic activity.

Furthermore, due to the lack of catalytic sites, **[Cobpy2–Fe]** and **[Cophen2–Fe]** show no oxygen evolution because all of the cobalt sites in these pentanuclear molecular complexes are fully coordinated to six –NC groups, preventing aqua (water) coordination to the cobalt sites. The complete inactivity of these complexes indicates that under photocatalytic conditions, the metal sites in cyanide-based Co–Fe compounds do not release the pyridyl or cyanide groups.

3.3.4 Electrochemistry and Surface Area Analysis

To understand the effect of pyridyl groups on the morphologic properties of the Co–Fe compounds, we conducted extensive characterisation and electrochemical experiments, determined the surface concentration of active cobalt sites, and estimated the upper bound turn-over frequency (TOF_{ub}).

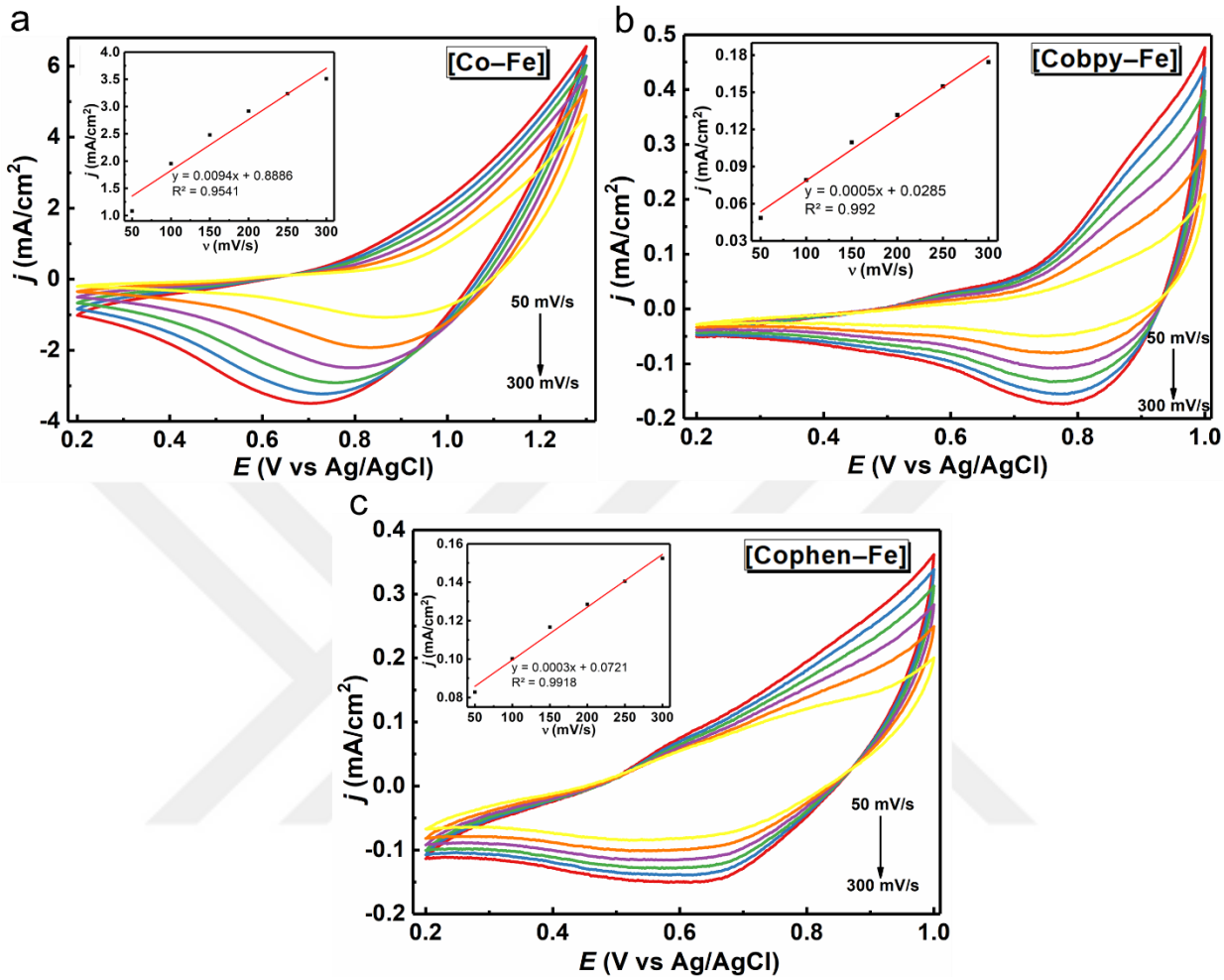

Figure 3.9: Cyclic voltammogram of (a) **[Co–Fe]**, (b) **[Cobpy–Fe]** and (c) **[Cophen–Fe]** recorded at different scan rate ranging from 50 – 300 mV s^{-1}. Inset: linear plot of the peak current (I) of Co^{3+}/Co^{2+} reduction wave versus scan rate (ν). Conditions: FTO (WE), Pt mesh (CE), Ag/AgCl (RE) in 0.1 M PBS (pH 7) containing 1 M KNO_3 as the supporting electrolyte. Reprinted with permission from Ref. [70]. Copyright 2022. American Chemical Society.

As shown in Figure 3.9, the surface concentration (Γ) of active cobalt sites was extracted from the electrochemical linear dependency between peak current (I) of the Co^{3+}/Co^{2+} reduction wave and the scan rate (ν), using cyclic voltammetry studies at varying scan rates (50–300 mV s^{-1}).[68] **[Co–Fe]**, **[Cobpy–Fe]**, and **[Cophen–Fe]** have surface concentration of 10.01, 0.53, and 0.32 nmol cm^{-2}, respectively. The bulky bidentate pyridyl groups block the surface-active sites, resulting in a considerable drop in surface concentration. The unfavorable blockage of cobalt sites with bidentate pyridyl groups, on the other hand, has no effect on the catalytic activity of **[Cobpy–Fe]**

and **[Cophen–Fe]**, implying that electronic factors are more important in the photocatalytic process than morphologic properties.

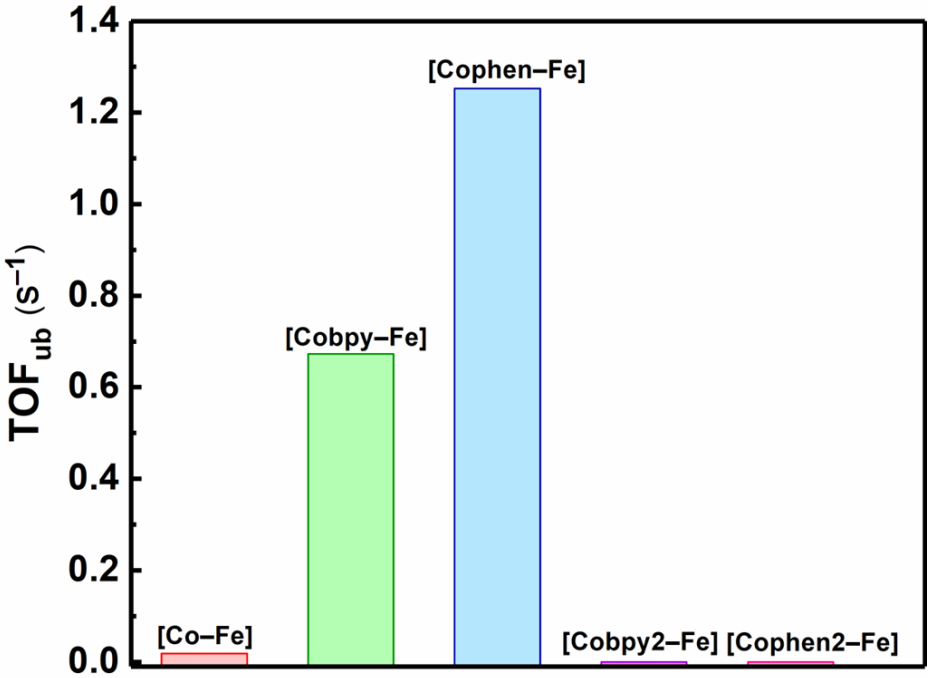

Figure 3.10: TOF_{ub} obtained by the compounds in the first 15 min. of photocatalysis. Reprinted with permission from Ref. [70]. Copyright 2022. American Chemical Society.

The upper-bound turnover frequency (TOF_{ub}) estimated from the surface-active cobalt species is given as 1.3 s^{-1}, 0.7 s^{-1}, and 1.8×10^{-2} s^{-1}, for **[Cophen–Fe]**, **[Cobpy–Fe]** and **[Co–Fe]**, respectively (Figure 3.10). **[Cobpy–Fe]** and **[Cophen–Fe]** have TOF_{ub} that is extremely higher than **[Co–Fe]**, revealing the remarkable electronic effect of the connected bidentate pyridyl groups. Because only the surface sites are active for catalysis in heterogeneous catalysis, the TOF_{ub} represents a reasonable value for the actual TOF. It also provides information on the catalytic activity of individual surface cobalt atoms. These TOF values are compared to those obtained by various techniques of improving cobalt catalyst photocatalytic activity (Table 3.5)

Table 3.5: Comparison of water oxidation TOF of various cobalt catalysts and PBA-based compounds.

Catalyst	Lower bound TOF x 10^{-4} (s^{-1})	Upper bound TOF (s^{-1})	Ref
Co–Fe PBA	1.7	0.018	This work
[Cobpy–Fe]	3.9	0.7	This work
[Cophen–Fe]	4.4	1.3	This work
nano-SiO_2/Co_3O_4	3.3	–	[22]
nano-Al_2O_3/Co_3O_4	4.61	–	[22]
cobalt oxide nanocubane	–	0.023	[45]
cobalt−phosphate (Co−Pi)	–	0.053, 0.105	[44]
Co–Fe PBA	3	0.0023	[69]
Co–Co PBA	5.3	0.0032	[69]
Mn–Fe PBA	2.2	–	[69]
CoFe–TPyP	3.2	–	[85]
LDH-PB	2.1	–	[79]

3.3.5 Post-Catalytic Characterization

After photocatalytic water oxidation measurements, post-catalytic FTIR and XPS tests were carried out to establish the catalysts' stability. The O1s XPS signals of the pristine and post-catalytic powder samples of **[Cobpy–Fe]** and **[Cophen–Fe]** show no discernible changes (Figure 3.11a,c). Furthermore, the absence of a lattice cobalt oxide signal in the 529–530 eV region of the post-catalytic samples rules out cyanide-based compounds being converted to metal oxides.[81] The pristine and post catalytic XPS spectra show similar Fe2p and Co2p signals (Figure 3.12a-d), indicating that the metal centers are intact.

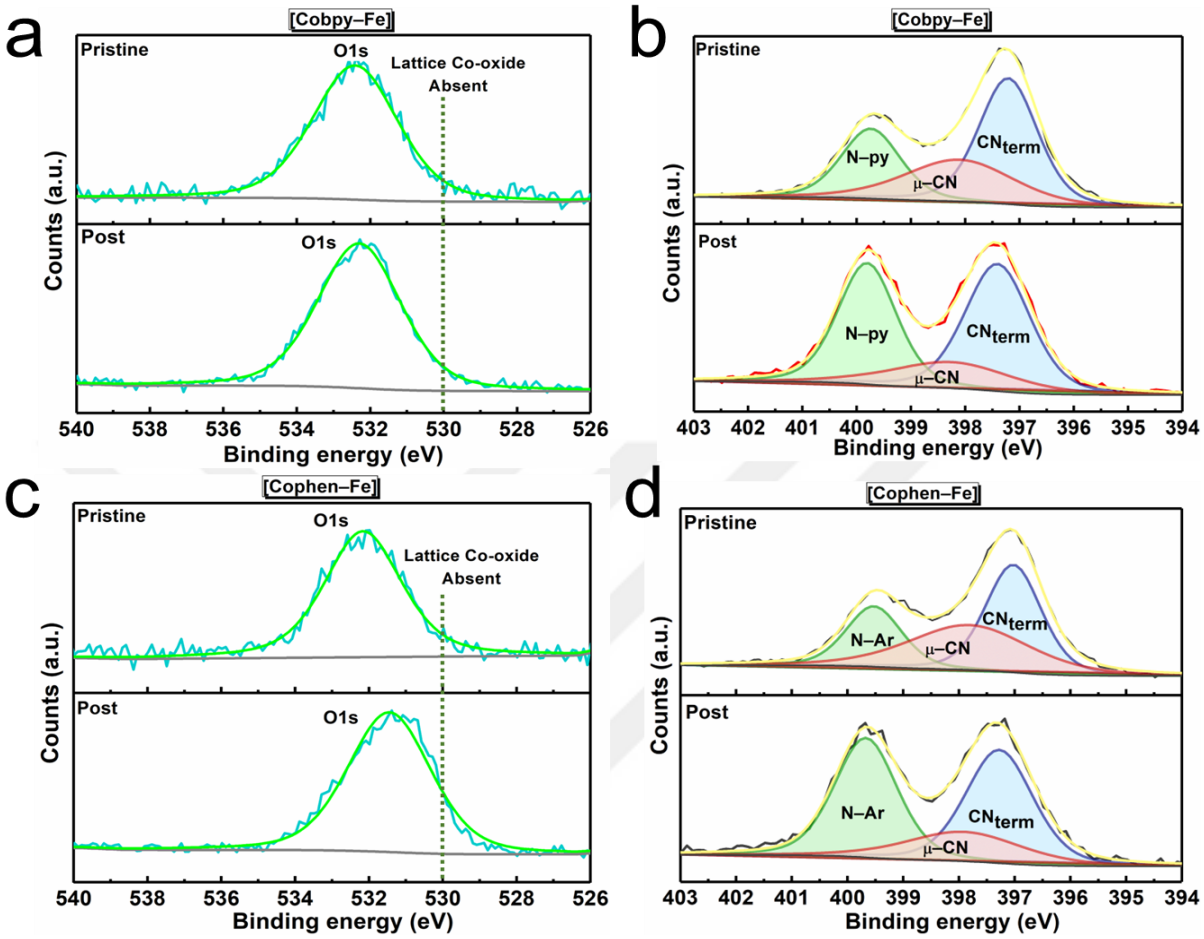

Figure 3.11: (a) O1s and (b) N1s pristine and post-catalytic high resolution XPS spectra for **[Cobpy–Fe]**. (c) O1s and (d) N1s pristine and post-catalytic high resolution XPS spectra for **[Cophen–Fe]**. Reprinted with permission from Ref. [70]. Copyright 2022. American Chemical Society.

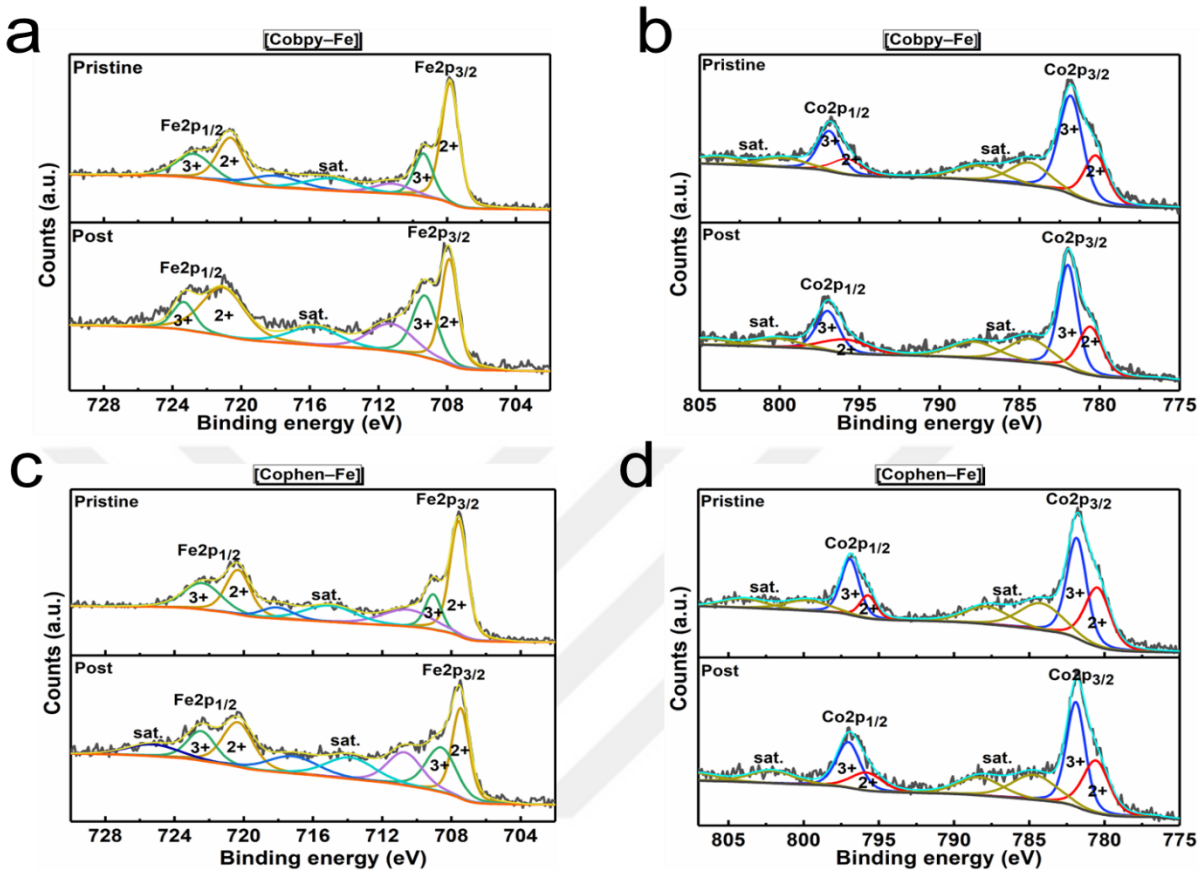

Figure 3.12: High resolution XPS spectra of (a,c) Fe2p and (b,d) Co2p from the pristine and post-catalytic samples of **[Cobpy–Fe]** and **[Cophen–Fe]**, respectively. Reprinted with permission from Ref. [70]. Copyright 2022. American Chemical Society.

In comparison to the pristine samples, the post catalytic FTIR analysis indicates an additional tiny band in the cyanide region (~ 2,100 cm^{-1}) and a widening at about 900–1,100 cm^{-1} (Figure 3.13a,b). Both of these alterations could be related to bipyridyl poisoning of the catalyst.[69] The ruthenium complex used as a photosensitizer in photocatalytic water oxidation decomposes after some time under light exposure by releasing bipyridyl groups. The bpy groups might then bind to the catalytic sites, rendering them inactive for water oxidation. In the N1s signal of the post-catalytic XPS spectra (Figure 3.11b,d), almost a twofold increase in the atomic percent of the pyridyl nitrogen (N–py) peak at 398.95 eV also suggests the presence of an extra pyridyl group in the structure that could only result via bipyridyl poisoning.

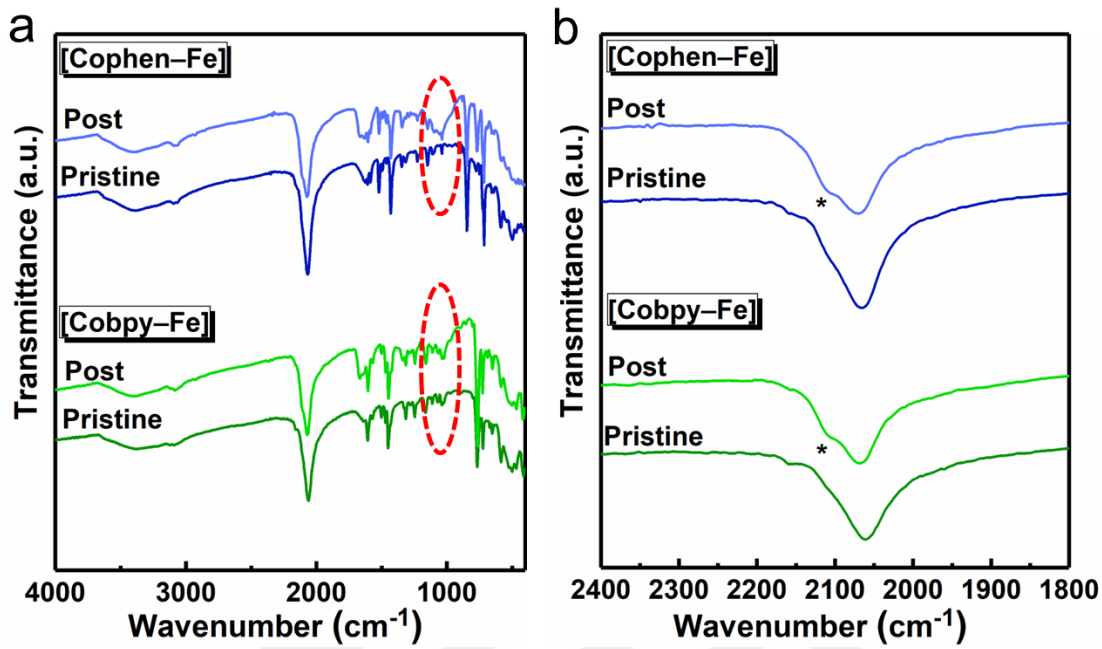

Figure 3.13: FTIR spectra of the pristine and post-catalytic samples of **[Cobpy–Fe]** and **[Cophen–Fe]** showing (a) the full spectrum ranging from 4,000–400 cm^{-1} (the encircled region from 900–1,100 cm^{-1} indicates the coordination of bipyridyl ligands to the Co–Fe structures) and (b) the cyanide stretching region ranging from 2,400–1,800 cm^{-1} (the asterisk point at ~ 2,100 cm^{-1} is ascribed to structural changes in the cyanide environment due to the coordination of bipyridyl groups to cobalt sites). Reprinted with permission from Ref. [70]. Copyright 2022. American Chemical Society.

Overall, post-catalytic investigations reveal that cyanide-based Co–Fe compounds are resilient under photocatalytic conditions and that the well-defined bidentate ligand environment of the catalytic sites has a significant impact on their water oxidation activities.

3.3.6 Electronic Structure Calculations

Electronic structural computations were used to study the effect of bidentate pyridyl ligands on the catalytic cobalt site. The literature suggests that the oxidation of water requires a Co^{IV}–oxo/Co^{III}–oxyl moiety, which is supported by our prior works.[47], [107]–[109] Proton coupled electron transfer (PCET) steps are used in PB-based water oxidation catalytic process to afford the Co^{IV}–oxo/Co^{III}–oxyl structure, i.e. $Co^{II}(OH_2) \rightarrow Co^{III}(OH) \rightarrow Co^{IV}(O)/Co^{III}(O)$. Incoming water then coordinates to the Co^{IV}–oxo/Co^{III}–oxyl molecule, resulting in the generation of an O–O bond

(Figure 3.14a). Our quantum mechanical computations are focused on the structural and electrical properties of the Co^{IV}–oxo/Co^{III}–oxyl moiety.

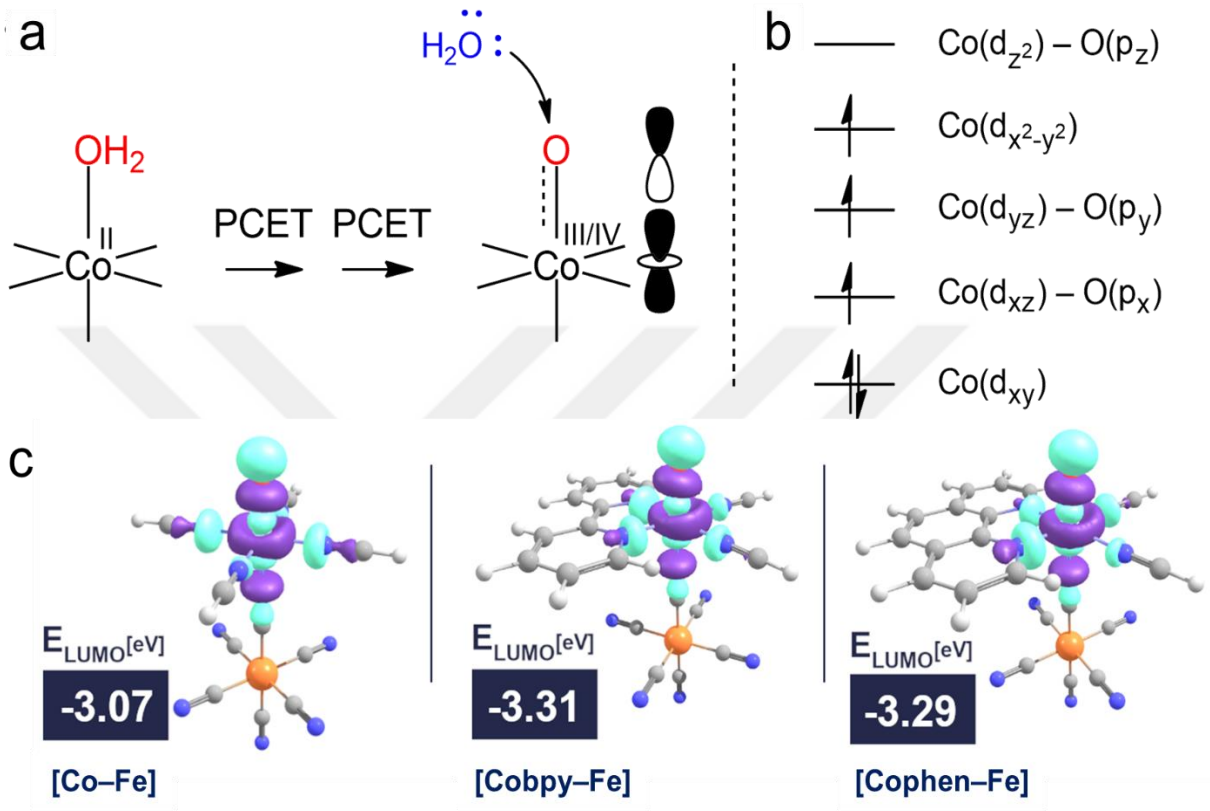

Figure 3.14: (a) PBAs proceeding through PCET steps to afford catalytically active Co(IV)–oxo/Co(III)–oxyl moiety, with incoming water attacking on Co–Oxygen moiety. (b) Electronic structure of Co–Oxygen moiety. (c) LUMO energies and orbital distributions for **[Co–Fe]**, **[Cophen–Fe]** and **[Cobpy–Fe]**. Reprinted with permission from Ref. [70]. Copyright 2022. American Chemical Society.

For **[Co–Fe]**, **[Cophen–Fe]** and **[Cobpy–Fe]**, the electronic structures of the Co^{IV}–oxo/Co^{III}–oxyl moiety exhibit a local quartet Co–Oxygen center (Figure 3.14b). Cobalt $d(x^2–y^2)$ orbital forms bonding and anti–bonding interactions with the ligand orbitals, $\sigma[Co(dx^2–y^2) + Ligand]$ and $\sigma[Co(dx^2–y^2) – Ligand]$. $d(z^2)$ analogues of the bonding/anti–bonding pair is then $\sigma[Co(dz^2) + O(pz)]$ and $\sigma[Co(dz^2) – O(pz)]$ molecular orbitals (MO). The remaining d orbitals are non–bonding, but oxygen p–orbitals form π–bonding interactions with the metal center.[110] Consequently, the xz and yz components of the d orbitals also form bonding and antibonding orbitals. An approximate local occupation pattern can be represented as $dxz(1\downarrow) \cdot \sigma[Co(dx^2–y^2) –$

Ligand](1) · π[Co(dxz) – O(px)](1) · π[Co(dyz) – O(py)](1) · σ[Co(dz^2) – O(pz)]() (Figure 3.14b). Spin density measurement is also used to confirm the Co center's local quartet assignment. It is worth noting that in our quantum chemical calculations, no limits on electron dispersion were imposed.

From the electronic structure, we can easily understand the essential O–O bond formation process. The oxygen lone pairs of water molecules look for available orbitals to transfer electron to, and the LUMO is the best choice. The LUMO is composed of Co(dz^2) and O(pz) orbitals as shown in Figure 3.14b. Since oxygen lone pairs of water are postulated to fill up the LUMO on Co–Oxygen center, the observed reactivities and energy of the LUMO should be related in this quartet electronic structure of Co–Oxygen center. Lower LUMO energies, in the instance, should result in increased catalytic activity.[39], [47], [83], [111] Figure 3.14c shows the LUMO orbital distributions and energies for the complexes. LUMO is obtained at lower energies for **[Cobpy–Fe]** and **[Cophen–Fe]** (–3.31 and –3.29 eV, respectively) compounds than for **[Co–Fe]** (–3.07 eV). This is consistent with our MO arguments. When bidentate pyridyl ligands, such as bpy or phen, are coordinated to the Co center, the electron affinity of the Co–Oxygen center is enhanced. As a result, the attack of water molecules becomes more facile in the well-defined ligand environment. Furthermore, because there is no bonded Co–Oxygen structure in **[Cobpy2–Fe]** and **[Cophen2–Fe]** compounds, there are no accessible orbitals for electron transfer and would display no activity.

Although we did not employ the whole molecular structure of the Prussian blue in our quantum chemical calculations, the electronic structure calculations and our experimental results correspond pretty well. Therefore, the abbreviated model used here is valid.

CHAPTER 4.

4.0 2D CYANIDE-BASED COORDINATION COMPOUND FOR PHOTOCATALYTIC HYDROGEN EVOLUTION

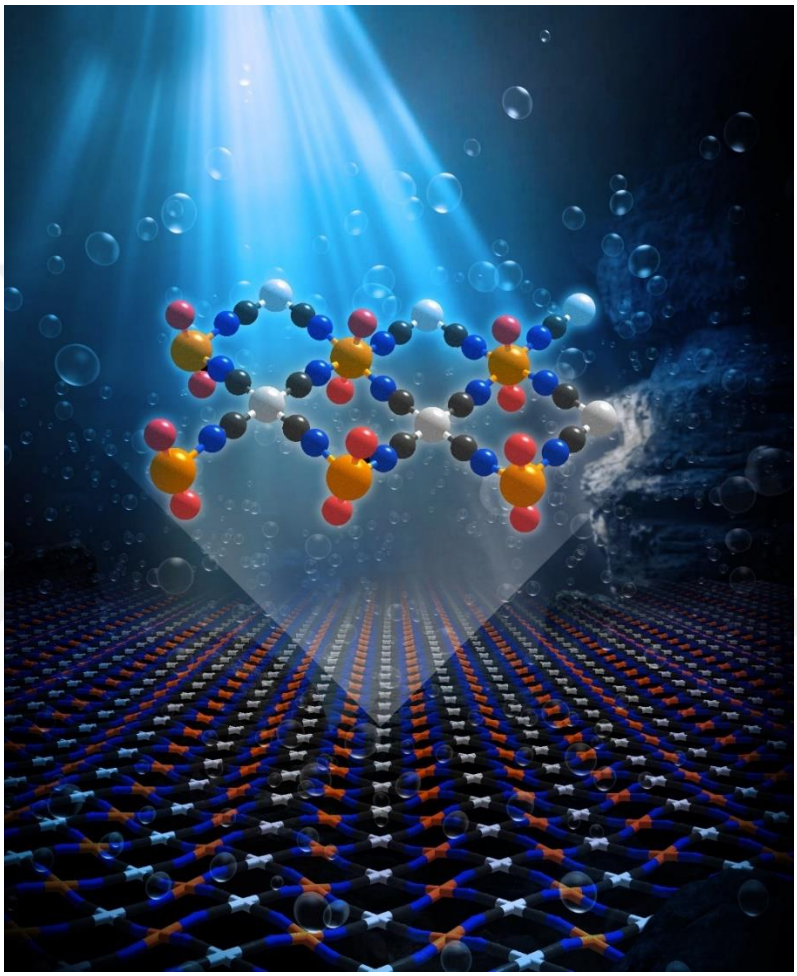

4.1 Preface

This chapter of the thesis is based on the publication "Ahmad, A. A.; Ghobadi, T. G. U.; Ozbay, E.; Karadas, F. 2D Network Overtakes 3D for Photocatalytic Hydrogen Evolution". **Chem. Commun.** 2022, ***Accepted.***

4.2 Introduction

Hydrogen production via catalytic water splitting is a promising and environmentally friendly alternative to fossil fuel energy sources. The scalable design requires a low-cost, easily-synthesized, and highly-efficient catalyst. 3D cyanide-based networks, typically known as Prussian blue analogues (PBA), have gained significant attention in catalysis due to their porosity, easily-tuned metal sites, and stability. However, the limited number of exposed active sites and low conductivity severely diminish their intrinsic catalytic activities. Therefore, PBA exhibit low intrinsic HER activity than their corresponding sulfides and chalcogenides. Recent efforts to promote PBA as a proton reduction catalyst have focused on coupling with active semiconductors or breakdown into phosphides and chalcogenides. However, the improved performance of these methods is reliant on the semiconductors or deconstructed structures. In contrast to 3D structures, 2D materials such as graphene and metal sulfides have been shown to have a high inherent catalytic due to their extensive surface-active sites and optoelectronic features. In this respect, we turned our attention to the preparation of a 2D cyanide-based coordination network to unify the exceptional advantages of cyanide-based assemblies and the unique surface/electronic properties of a 2D architecture.

Herein, using a square planar tetracyanonickelate precursor, $[Ni(CN)_4]^{2-}$, we synthesized a 2D cyanide-based coordination network polymer. We performed a series of characterization, catalytic experiments, and a comparative analysis with 3D cyanide coordination compounds. In addition, we used zinc tetracyanonickelate, **[Zn–Ni]**, as a control to determine the role of each metal site of the 2D architecture in the catalytic process.

4.3 Results and Discussions

4.3.1 Synthesis

The compounds were prepared by co-precipitation technique, simply by mixing an aqueous solution of the appropriate equivalent of Co^{2+} or Zn^{2+} with the proper equivalent of cyanide precursors (Figure 4.1). Hexacyanometalate served as the cyanide precursor for the synthesis of **[Co–Fe]** and **[Co–Co]**, while tetracyanonickelate precursor was used for the synthesis of **[Co–Ni]** and **[Zn–Ni]**.

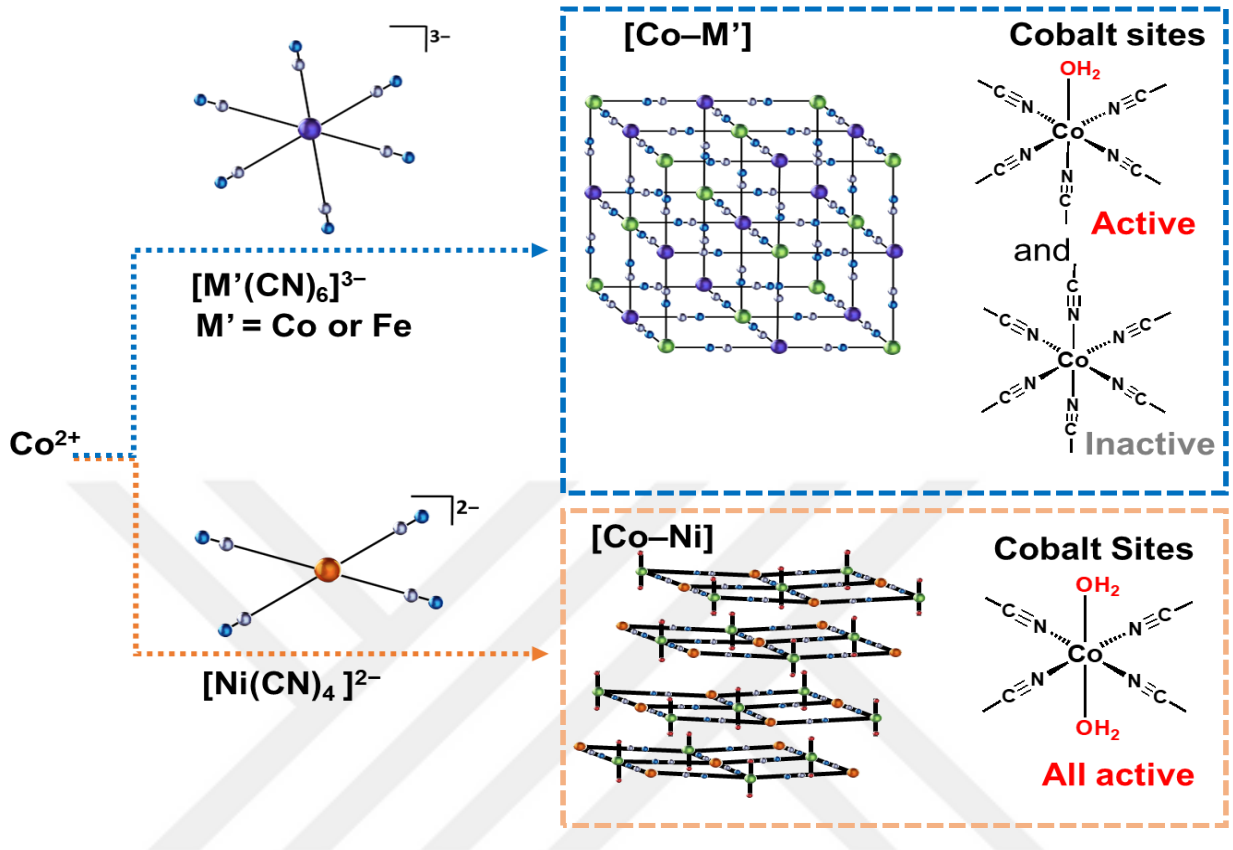

Figure 4.1: Schematic illustration for the synthesis of 3D **[Co–M']** and 2D **[Co–Ni]** coordination compounds and the coordination spheres of catalytic units.

4.3.2 Catalysts Characterization

4.3.2.1 TEM

Well-defined images revealing distinct morphology of the compounds were obtained from the TEM micrographs (Figure 4.2), the **[Co–Fe]** show a perfect cubic morphology with a mean width of about 270 nm, and the **[Co–Co]** exhibited irregular aggregated cubes with a width-size in the range of 50 nm. When the precursor is changed to tetracyanometalate, a notable divergence from the cubic morphology is found, **[Co–Ni]** presents a 2D-layered structure with a mean size of 250 nm. The multi-layered nature of the 2D sheets is vividly observed from the existence of multiple folds of sheets beneath the first layer. This multi-layered arrangement further increases the number of active sites present. The TEM images of **[Zn–Ni]** also reveal a 2D sheet structure.

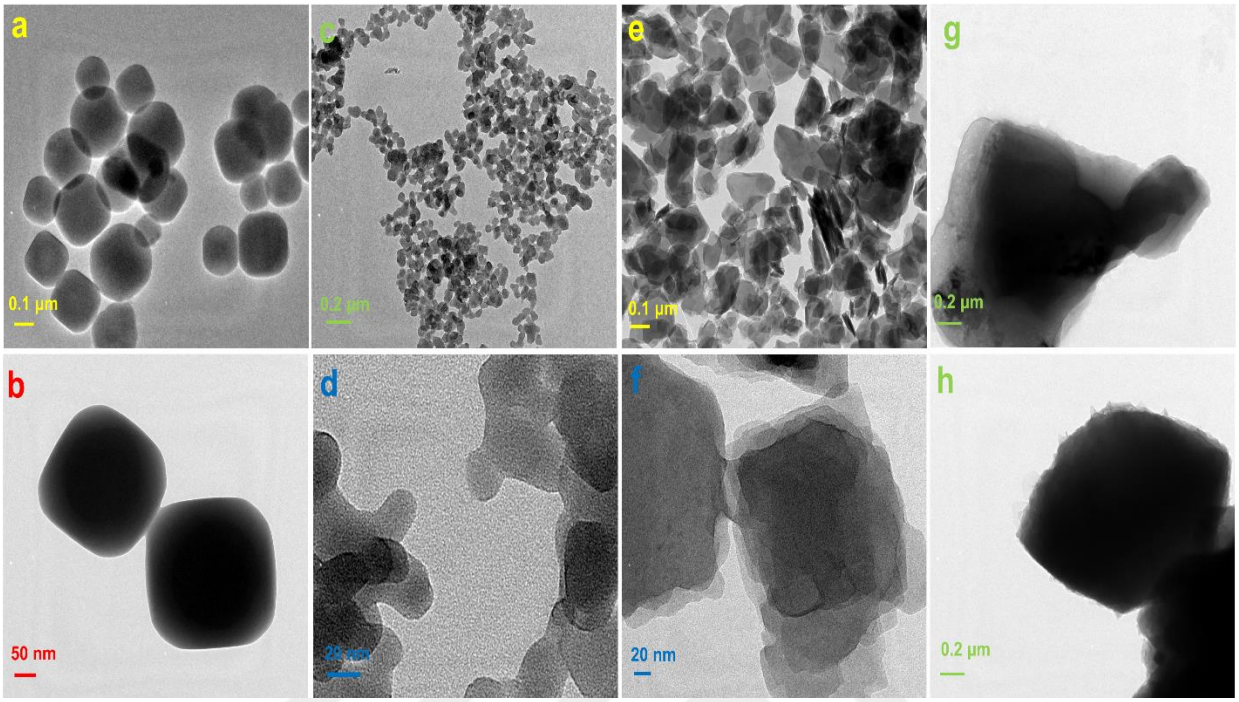

Figure 4.2: TEM micrographs of (a,b) **[Co–Fe]**, (c,d) **[Co–Co]**, (e,f) **[Co–Ni]** and (g,h) **[Zn–Ni]**. Scale bar: yellow (0.2 µm); red (50 nm); blue (20 nm); green (0.1 µm).

4.3.2.2 SEM-EDX

The SEM images of the compounds at 10 µm magnification is shown in Figure 4.3, **[Co–Ni]** revealed a cluster of layered particles for **[Co–Ni]**, **[Zn–Ni]** showed layers of spherical beads, and aggregated rough surfaces were observed for **[Co–Fe]** and **[Co–Co]**.

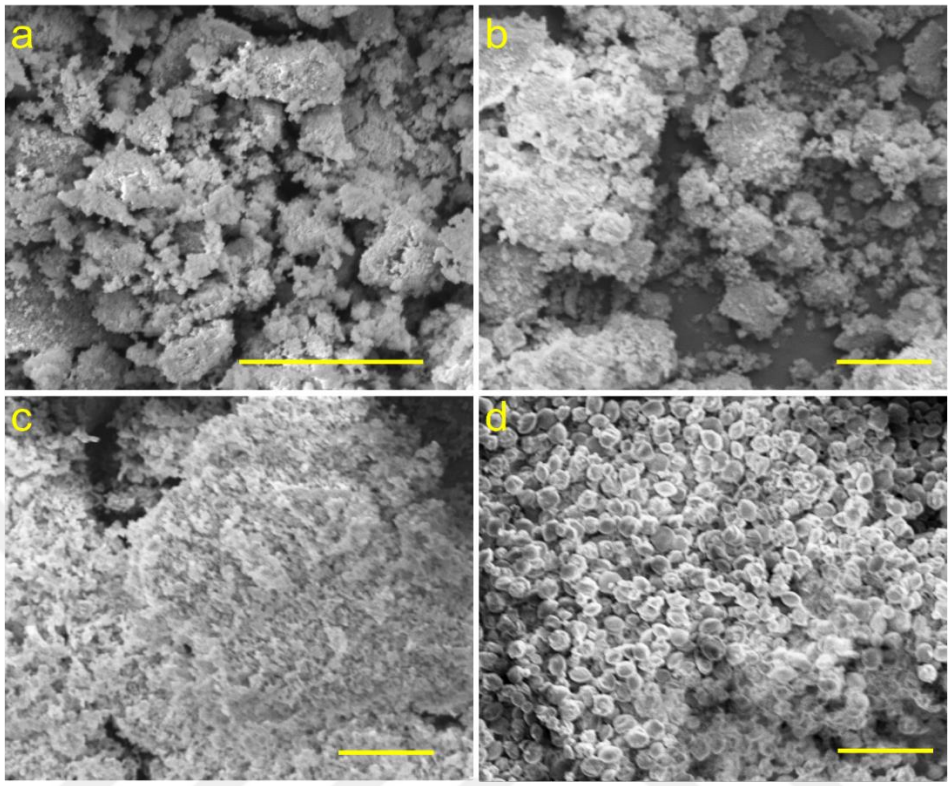

Figure 4.3: SEM micrographs of (a) **[Co–Fe]**, (b) **[Co–Co]**, (c) **[Co–Ni]** and (d) **[Zn–Ni]**. Scale bar: yellow (10 µm).

EDX elemental analysis revealed the atomic ratio of all the elements in the compound as shown in Table 4.1.

Table 4.1: The obtained chemical formula of the compounds derived from EDX elemental analysis and thermogravimetric analysis (TGA).

Compound	EDX Atomic %						TGA	
[M–M']	**M**	**M'**	**C**	**N**	**O**	**K**	**% Water molecule**	**Chemical Formula**
[Co–Fe]	2.91	2.01	58.5	28.28	7.43	0.1	26.58	$K_{0.1}Co_{2.9}[Fe(CN)_6]_2$ x $12H_2O$
[Co–Co]	11.46	–	39.53	42.84	4.75	0.63	30.12	$K_{0.1}Co_{2.9}[Co(CN)_6]_2$ x $14.5H_2O$
[Co–Ni]	5.40	5.26	41.41	42.28	5.38	–	15.55	$Co[Ni(CN)_4]$ x $2.3H_2O$
[Zn–Ni]	9.12	9.08	39.53	35.96	6.06	–	3.03	$Zn[Ni(CN)_4]$ x $0.4H_2O$

4.3.2.3 TGA

Thermogravimetric analysis was used to determine the number of water molecules contained in each compound (Figure 4.4). The loss of coordinated and non-coordinated water molecules is attributed to the thermal event from 30 ^{o}C to 175 ^{o}C, while the rest of the thermal decomposition at temperatures above 250 ^{o}C is due to the decomposition and reconstruction of the cyanide network to oxides.[97] The combination of TGA and EDX elemental analysis was used to determine the chemical formula of the compound as shown in Table 4.1.

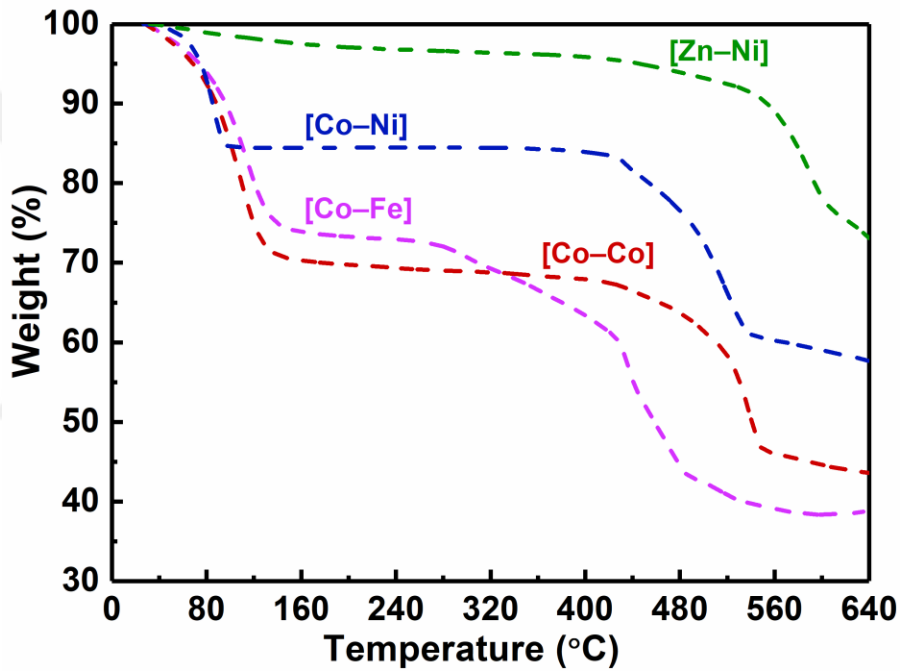

Figure 4.4: Thermogravimetric weight loss analysis.

4.3.2.4 CHN elemental analysis

CHN elemental analysis was used to ascertain the as-derived chemical formula of the compounds. As shown in Table 4.2, the elemental ratio of carbon, hydrogen and nitrogen revealed by CHN analysis accord with those calculated from the chemical formula.

Table 4.2: CHN elemental analysis of the synthesized compounds.

Compound	Chemical Formula	Calculated / Found (CHN)		
		%C	%N	%H
[Co–Fe]	$K_{0.1}Co_{2.9}[Fe(CN)_6]_2$ x $12H_2O$	17.69 / 17.19	20.61 / 19.52	2.94 / 2.84
[Co–Co]	$K_{0.1}Co_{2.9}[Co(CN)_6]_2$ x $14.5H_2O$	16.63 / 16.82	19.40 / 19.49	3.35 / 3.03
[Co–Ni]	$Co[Ni(CN)_4]$ x $2.3H_2O$	18.24 / 18.31	21.28 / 21.49	1.75 / 1.69
[Zn–Ni]	$Zn[Ni(CN)_4]$ x $0.4H_2O$	20.40 / 20.24	23.80 / 23.52	0.34 / 0.34

4.3.2.5 FTIR

Infrared spectroscopy was used to examine the chemical structure of the compounds. The peaks at around 3,400 cm^{-1} and 1,600 cm^{-1} are assigned to the OH stretching and bending vibrations, respectively (Figure 4.5a). The characteristic cyanide stretching vibrations (υ(CN)) appear for all the compounds in the region of 2,000–2,200 cm^{-1} (Figure 4.5b). The slight shift of the characteristic cyanide stretching (υ(CN)) vibrations of the compounds to higher wavenumbers compared to the precursor suggest the formation of a bridging cyanide network. The assignment of bands in the υ(CN) regions is listed in Table 4.3 according to the literature.[69], [112]–[117] The shift in υ(CN) to a higher frequency as we move from **[Co–Fe]** to **[Co–Ni]** indicates an increase in sigma donation from the CN group.

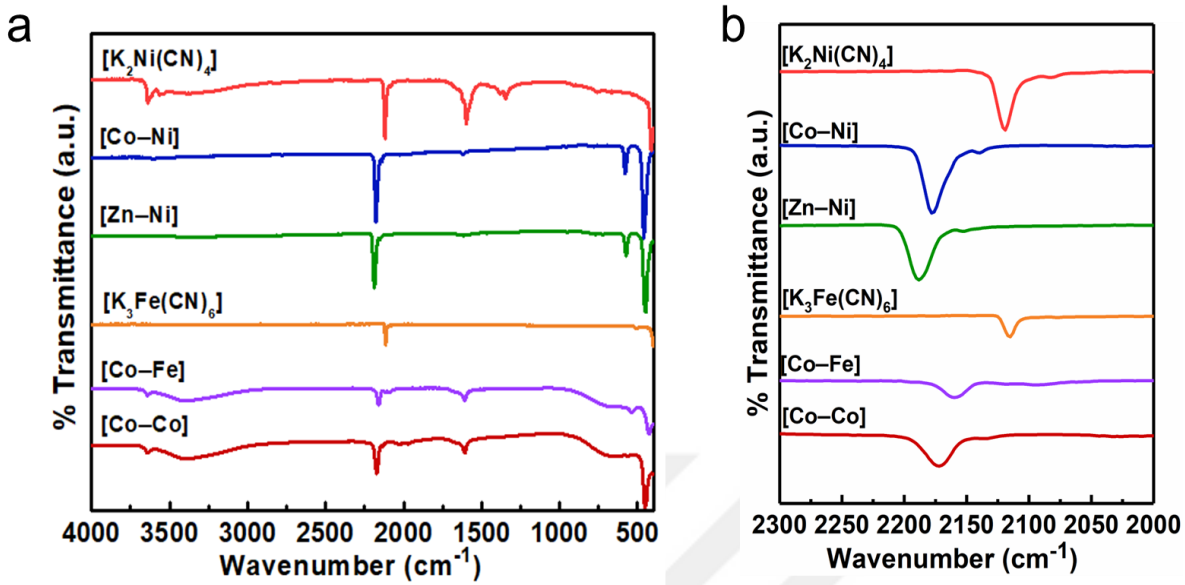

Figure 4.5: ATR-FTIR spectra showing (i) the precursor and the synthesized PBA compounds ranging from 4,000–400 cm^{-1} (ii) showing the υ(CN) region ranging from 2,300–2,000 cm^{-1}.

Table 4.3: Cyanide stretching frequencies, υ(CN), of the precursors and the synthesized compounds.

Compound	υ(CN) (cm^{-1})	Assignment*
$K_3Fe(CN)_6$	2115	Fe^{3+}–CN
[Co–Fe]	2162	Fe^{3+}–CN–Co^{2+}
	2117	Fe^{2+}–CN–Co^{3+}
	2098	Fe^{2+}–CN–Co^{2+}
[Co–Co]	2172	Co^{3+}–CN–Co^{2+}
	2133	Co^{2+}–CN–Co^{3+}
$K_2[Ni(CN)_4]xH_2O$	2119	Ni^{2+}–CN
[Co–Ni]	2177	Ni^{2+}–CN–Co^{2+}
	2141	Ni^{2+}–CN–Co^{3+}
[Zn–Ni]	2189	Ni^{2+}–CN–Zn^{2+}

*The assignments are listed in accordance with literature.[69], [112]–[117]

4.3.2.6 DR UV-vis

As shown in Figure 4.6, the bands below 400 nm are due to the ligand-to-metal charge transfer (LMCT) or metal-to-ligand charge transfer (MLCT), while the ones above 415 nm are assigned to the metal–to–metal charge transfer (MMCT). The well-established MMCT bands obtained in the visible region for all the cobalt-based compounds suggest efficient electron transfer between the metal sites.

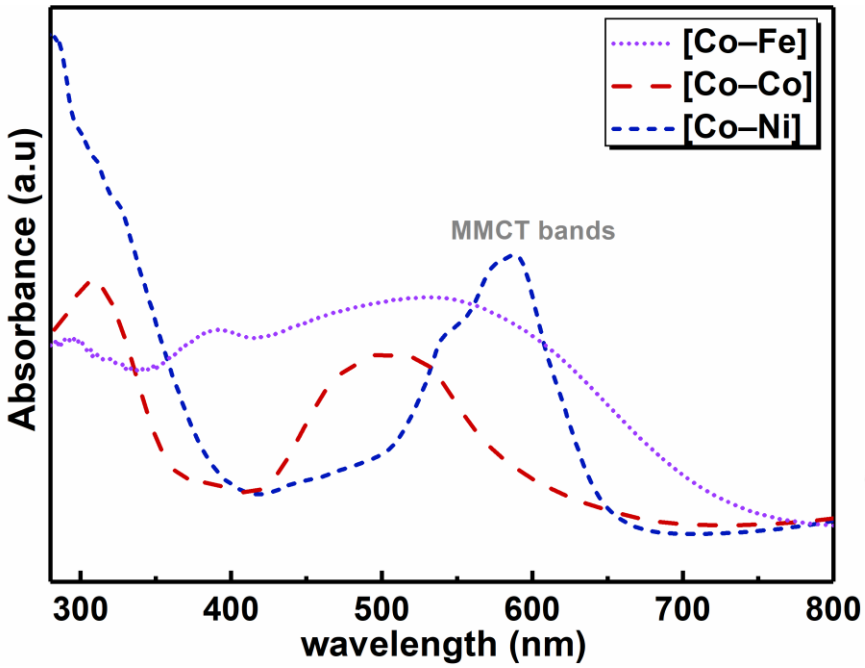

Figure 4.6: Diffuse reflectance UV-Vis spectra of **[Co–Ni]**, **[Co–Fe]** and **[Co–Co]**.

4.3.2.7 XRD

The diffraction patterns obtained from PXRD (Figure 4.7a) revealed the crystal structure of the synthesized compounds. The PXRD patterns of both **[Co–Fe]** and **[Co–Co]** display sets of diffraction peaks at 14.77º, 17.30º, 24.56º, 35.02º, and 39.30º which are ascribed to the (111), (200), (220), (400), and (420) reflection planes of a face-centered cubic structure, respectively.[101] The diffraction patterns of **[Co–Ni]** matched perfectly with the crystal structure of the standard L_1 phase layered $M(H_2O)_2[NiCN_4]\bullet xH_2O$ in the *Imma* space group (Figure 4.7b).[117] Each nickel site is coupled to four cyanide groups in this 2D layered structure, resulting in a square planar geometry. Each cobalt site is coordinated to four cyanide groups from the terminal nitrogen sites and two water molecules from the axial positions to reveal a trans-CoN_4O_2

coordination environment. The coordinated water molecules interact with non-coordinated water molecules via hydrogen bonding interaction.[118] This hydrogen bonding network beneath and above each layer creates a space volume or 2D channels with a distance of ~ 5.8 Å between the layers (Figure 4.7c), thereby allowing for easy diffusion of H_2O and H^+ between the layers making each layer accessible for the catalytic process.

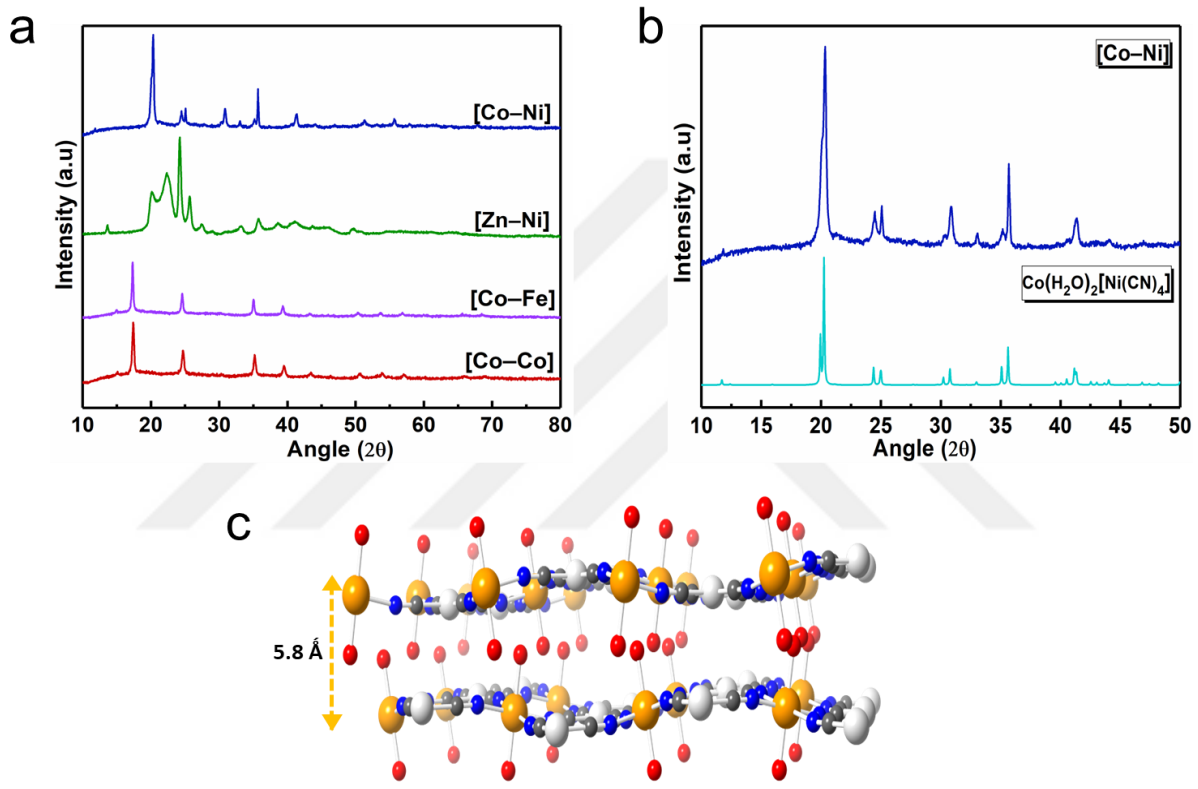

Figure 4.7: (a) PXRD patterns of the compounds (b) PXRD of the as-synthesized **[Co–Ni]** matched perfectly with a reference compound. (c) Side view showing the interlayer distance of the crystal structure of **[Co–Ni]**. Colour code: Co, orange; Ni, white; C, grey; N, blue; O, red. H atoms of H_2O are omitted for clarity. The reference compound is a standard L_1 phase layered $Co(H_2O)_2[NiCN_4]\cdot xH_2O$ in an *Imma* space group, and the crystal structures were created from cif. files deposited at CCDC.[117]

4.3.2.8 XPS

The chemical composition of the compounds and oxidation states of the transition metals was determined with XPS measurements. The XPS spectra of **[Co–Ni]** is shown in Figure 4.8, the presence of N 1s peak is due to the existence of the CN group, while the O1s signal is assigned to the coordinated water molecules and those in the interstitial sites/cavities. The absence of peaks in the 529–530 eV region of the O1s peak suggests no metal-oxide formation in the course of synthesis.[104] The obtained Co2p (~ 770 – 810 eV) and Ni2p (~ 845 – 880 eV) core level XPS spectra are deconvoluted into $2p_{3/2}$ and $2p_{1/2}$ due to spin-orbit coupling,[119] with a Shirley-type background by fitting. The Co2p peaks are well-fitted into Co^{2+} and Co^{3+}, the presence of Co^{2+} is supported by the presence of shake-up satellite peaks.[120] Unfortunately, the strong overlapping of Co and Ni Auger lines with the photoelectron peaks complicate the spectrum. Therefore in Co2p, weak Ni LMM and Co LMM Auger peaks are detected around 778 eV and 775 eV, respectively.[121]–[123] The $Ni2p_{3/2}$ and $Ni2p_{1/2}$ signals are fitted into one main peak assigned to Ni^{2+}. The absence of satellite peaks strongly supports that the Ni^{2+} is square planar with diamagnetic nature. Also, a plasmon energy loss related broad peak was observed between the main Ni2p peaks.

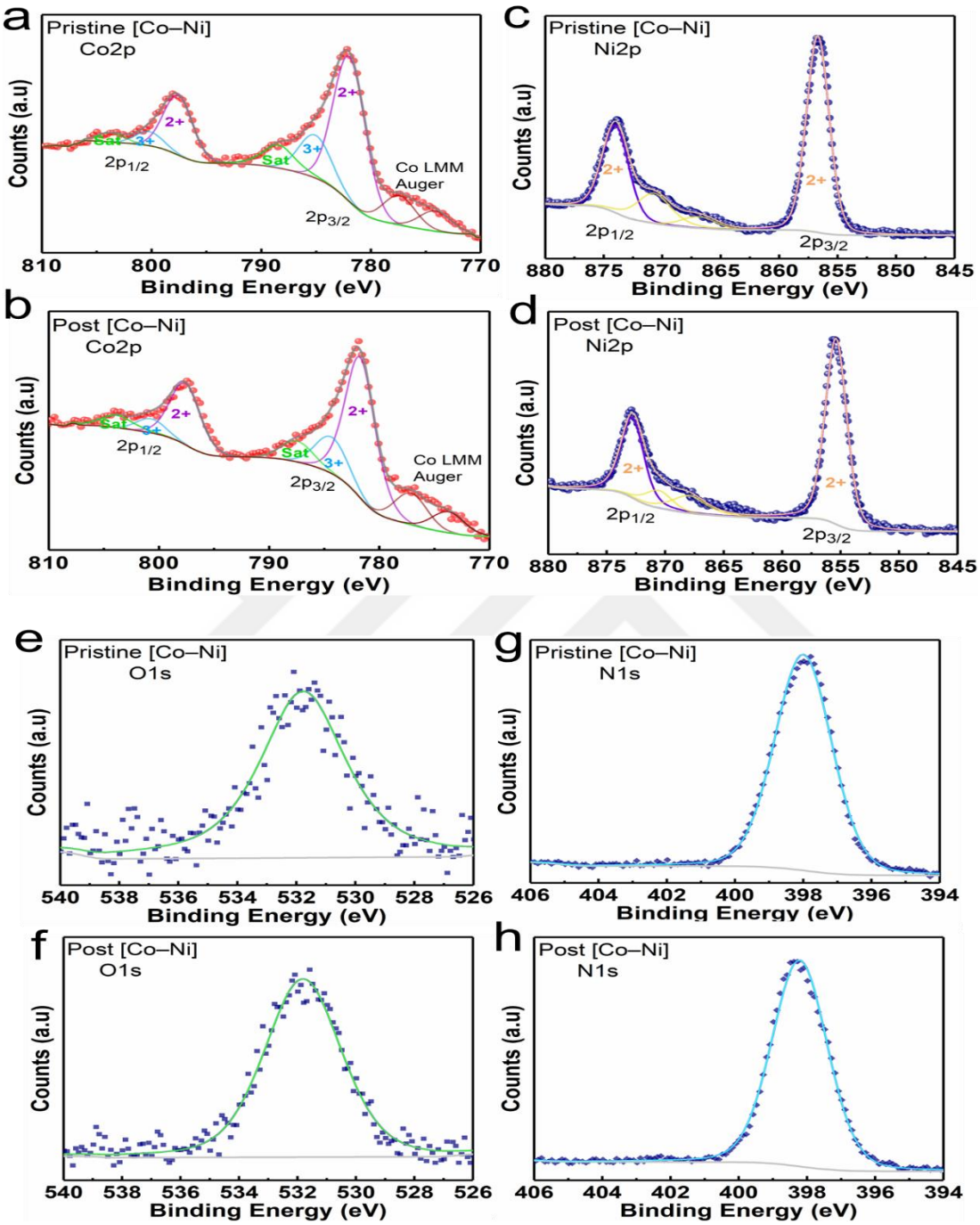

Figure 4.8: High-resolution XPS spectra of (a,b) Co2p, (c,d) Ni2p, (e,f) O1s, and (g,h) N1s from the pristine and post-catalytic samples **[Co–Ni]**.

[Zn–Ni] displayed Zn2p (~ 1016 – 1050 eV) and Ni2p (~ 845 – 880 eV) core level XPS peaks which also splits into $2p_{3/2}$ and $2p_{1/2}$ due to spin-orbit coupling (Figure 4.9).[119] Spin states of both Zn2p and Ni2p are fitted into one main peak assigned to 2+ oxidation state. The absence of satellite peaks strongly supports that the Zn^{2+} has a completely filled d-orbital and Ni^{2+} is square planar and diamagnetic. The existence of multiple small peaks at energies below $2p_{1/2}$ spin correspond to the plasmon energy loss features.[122]

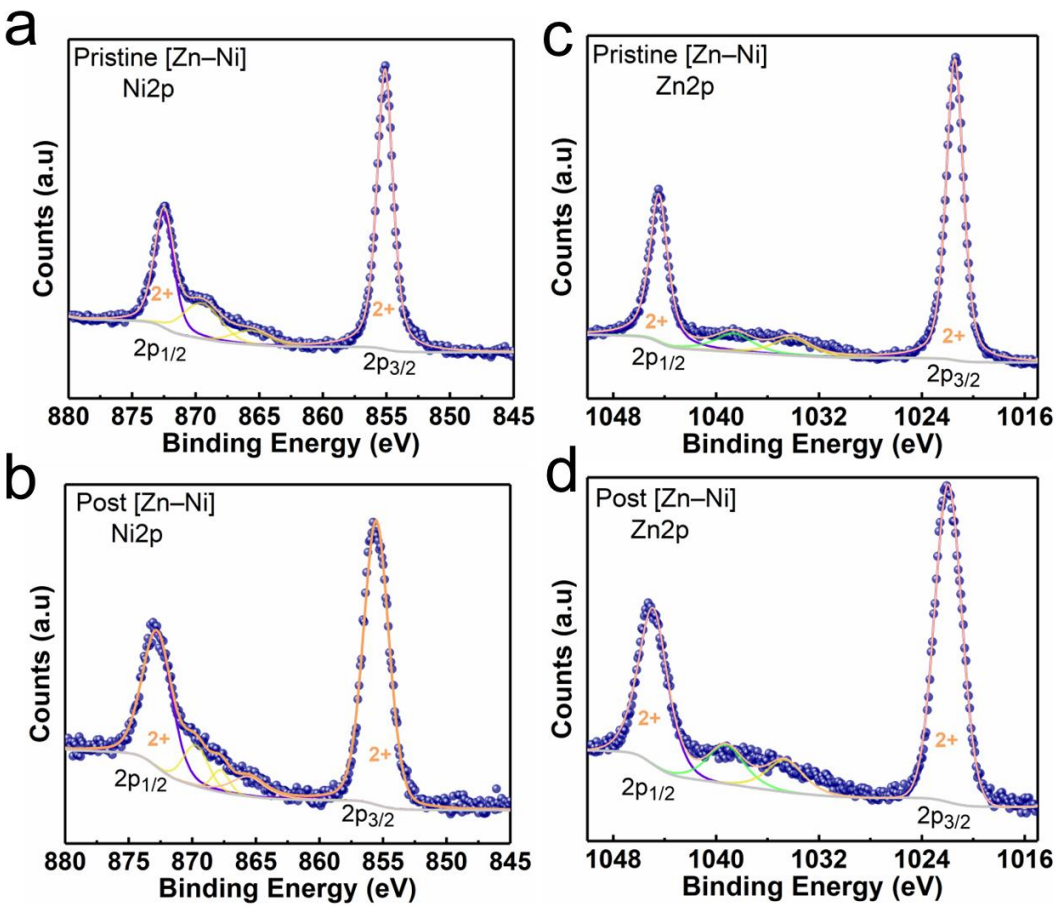

Figure 4.9: XPS curve-fitting results of (a,b) Ni2p, (c,d) Zn2p spectra from pristine and post **[Zn–Ni]** samples.

[Co–Fe] XPS spectra confirms the presence of Co2p (~ 770 – 810 eV) and Fe2p (~ 700 – 730 eV) signals which splits into $2p_{3/2}$ and $2p_{1/2}$ due to spin-orbit coupling (Figure 4.10).[119] The assignment of the Fe2p peaks are analyzed into Fe^{2+} and Fe^{3+}, likewise, the Co2p peak is divided

into Co^{2+} and Co^{3+} accordingly.[70] The strong shake-up satellite peaks in Co2p signals are due to the existence of Co^{2+}.[119]

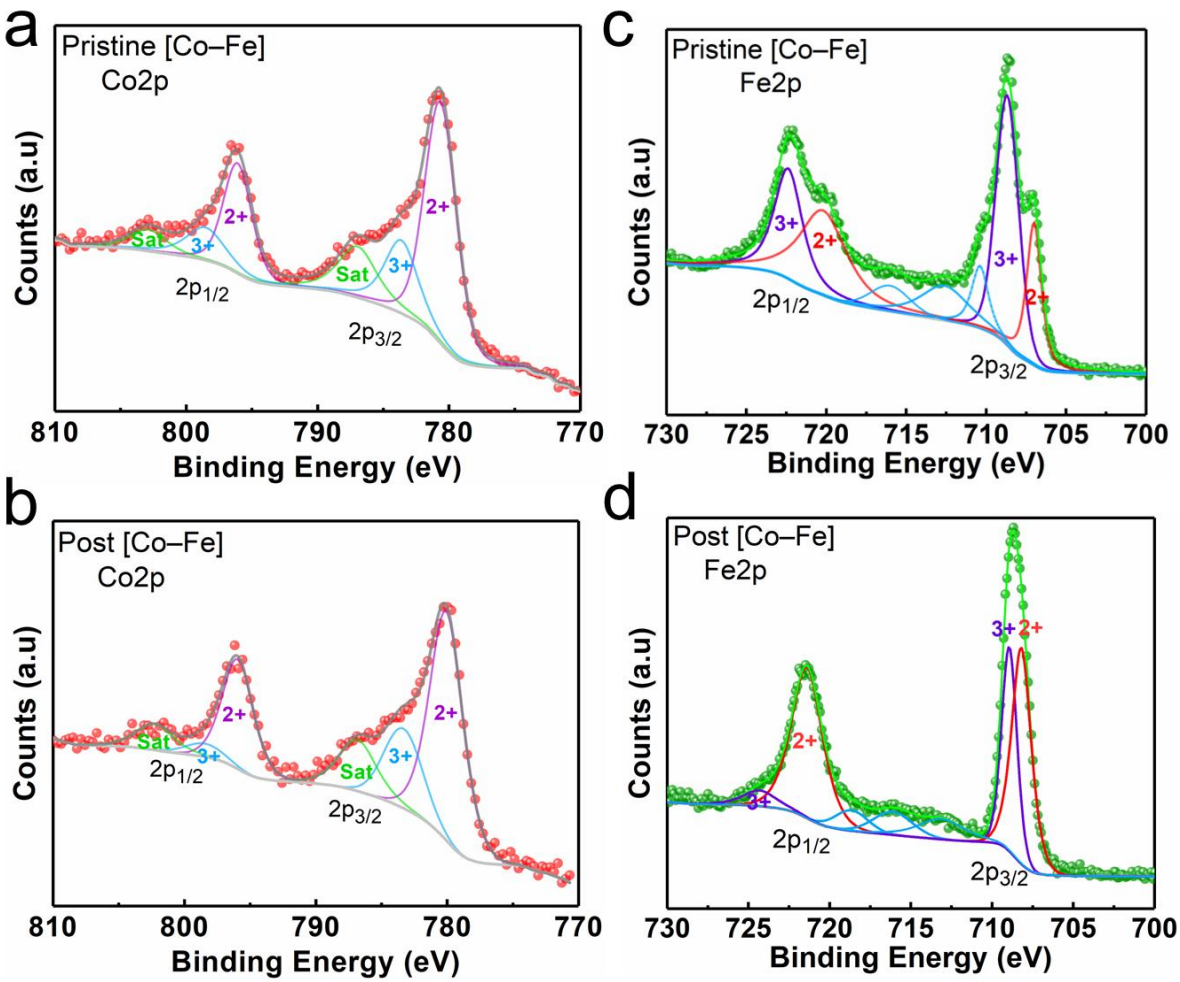

Figure 4.10: XPS curve-fitting results of (a,b) Co 2p, (c,d) Fe 2p spectra from pristine and post **[Co–Fe]** samples.

[Co–Co] displayed only the cobalt transition metal signal, Co2p peak (~ 770 – 810 eV), which also splits into $2p_{3/2}$ and $2p_{1/2}$ due to spin-orbit coupling(Figure 4.11).[119] Both the $Co2p_{3/2}$ and $Co2p_{1/2}$ peaks are a combination of Co^{2+} and Co^{3+} based on the spin-orbit splitting values. The multiple peaks located in the 770-780 eV range are attributed to the Co LMM Auger peaks.

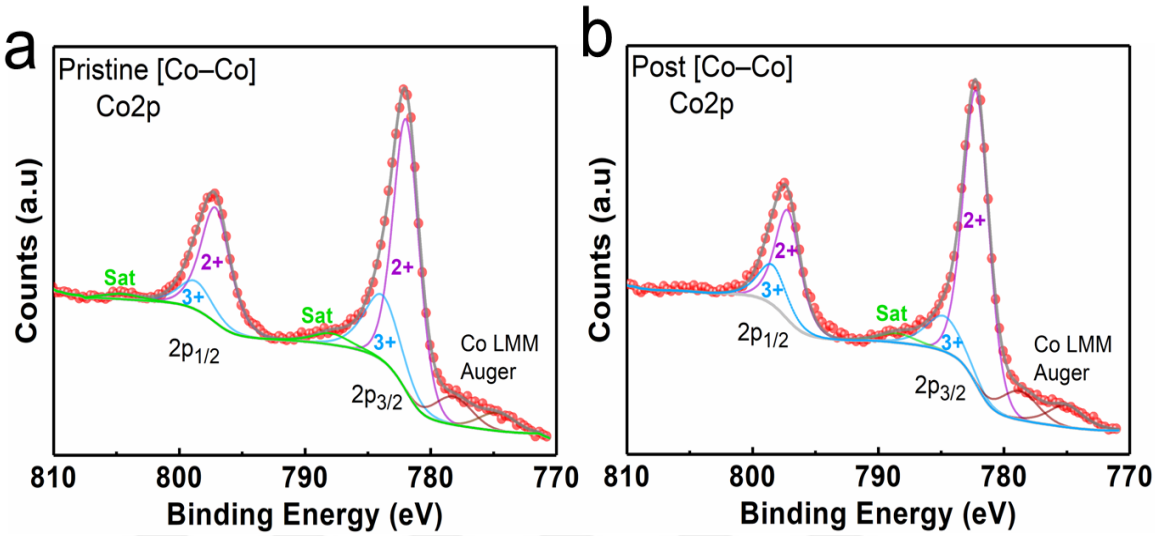

Figure 4.11: XPS curve-fitting results of Co2p peaks spectra from (a) pristine and (b) post **[Co–Co]** samples.

4.3.3 Photocatalytic HER

The photocatalytic hydrogen evolution experiments were performed in a three-component system consisting of the catalyst, $[Ru(bpy)_3]Cl_2$ as the photosensitizer, and ascorbic acid as the electron donor in an aqueous solution at pH 5. The layered **[Co–Ni]** displayed a remarkable HER activity of 4,229 μmol g^{-1} h^{-1}, which is ~20 and ~7 times higher than **[Co–Fe]** (216 μmol g^{-1} h^{-1}) and **[Co–Co]** (617 μmol g^{-1} h^{-1}), respectively (Figure 4.12). The $[Ru(bpy)_3]^{2+}$/ascorbate couple exhibits an HER activity of just 40 μmol g^{-1} h^{-1} under the same conditions, implying that the recorded photocatalytic HER performance is primarily due to the catalyst.

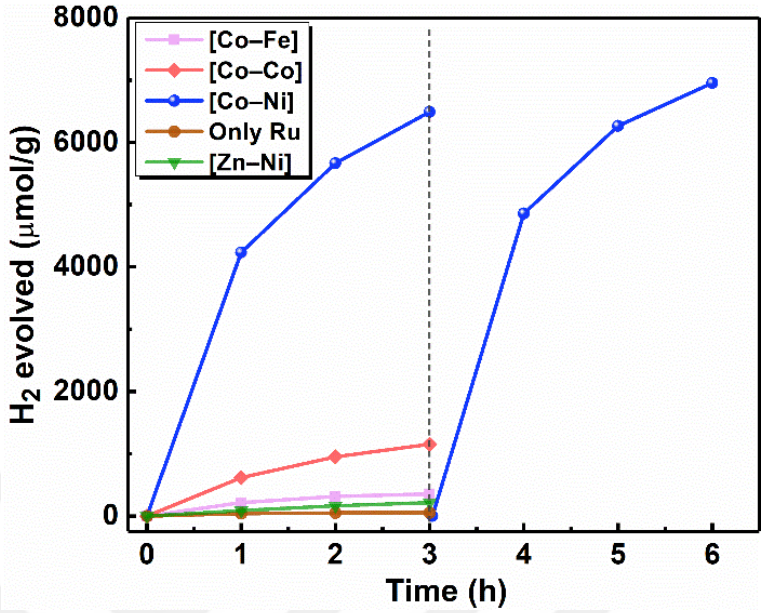

Figure 4.12: Photocatalytic HER activities of the compounds. Conditions: 10 mg Catalyst, 100 mM ascorbic acid, pH 5, (7.5 mg) 1 mM $[Ru(bpy)_3]Cl_2$, and 100 mW cm^{-2} white light source.

4.3.4 Surface Area Analysis

The significantly higher activity in **[Co–Ni]** is attributed to the 2D structure and multi-layered arrangement, which provides a larger surface area of contact for catalysis and boosts the number of active catalytic sites.[124] In order to probe and confirm the changes in surface area quantitatively, the surface concentration of catalytic cobalt sites is estimated from the plot of Co^{3+}/Co^{2+} reduction wave peak current (I) and the scan rate (ν) to evaluate the effect of morphology on the redox-active sites (Figure 4.13).[68] **[Co–Ni]** revealed an active surface concentration of 2.55 nmol cm^{-2}, which is ~ 36 and 6 times higher than **[Co–Fe]** (0.07 nmol cm^{-2}) and **[Co–Co]** (0.43 nmol cm^{-2}), respectively. These results confirm the effect of the decrease in dimensionality on the catalytic activity.

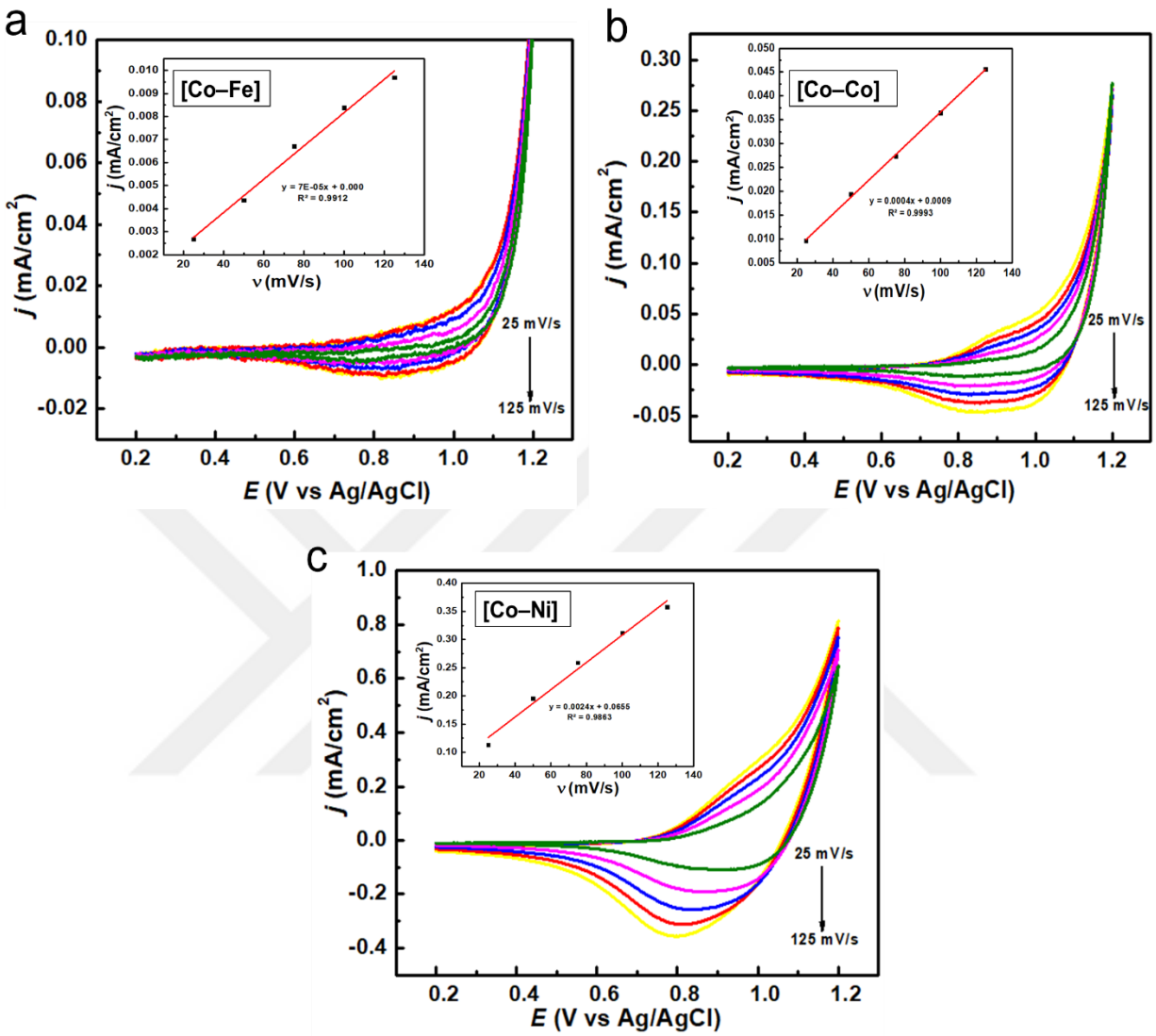

Figure 4.13: Cyclic voltammogram of (a) **[Co–Fe]**, (b) **[Co–Co],** and (c) **[Co–Ni]** recorded at different scan rate ranging from 25 – 125 mV s^{-1}. Inset: linear plot of the peak current (I) of Co^{3+}/Co^{2+} reduction wave versus scan rate (ν). Conditions: FTO (WE), Pt mesh (CE), Ag/AgCl (RE) in 0.1 M PBS (pH 7) containing 1 M KNO_3 as the supporting electrolyte.

4.3.5 Effect of Catalyst and Photosensitizer amount on Photocatalytic HER

Photocatalytic studies with varying amounts of the catalyst and Ru photosensitizer indicate that **[Co–Ni]** can reach a photocatalytic hydrogen evolution rate of as high as 30,029 μmol g^{-1} h^{-1} when 2 mg of catalyst and 7.5 mg $[Ru(bpy)_3]Cl_2$ is used (Figure 4.14). If all the cobalt sites are assumed to be active, a TON of 40 mol of H_2 per mol of catalyst is achieved in 1 hour. At this hydrogen

production rate, the H_2 bubbles evolved by **[Co–Ni]** in the solution were visibly observed in real-time. The list compiled in Table 4.4 indicates that **[Co–Ni]** as a cyanide-based catalyst candidate is also top-ranked when compared to other high-performing HER catalysts operating under different conditions reported in the literature.

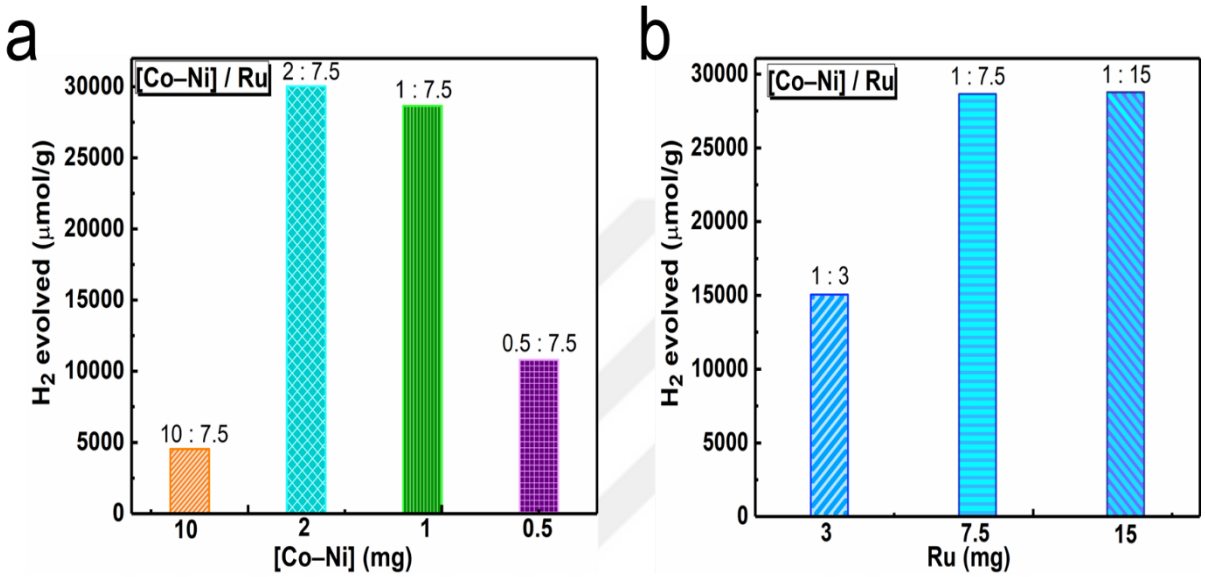

Figure 4.14: (a) The effect of the amount of catalyst on the photocatalytic HER performance of **[Co–Ni]** for 1 h. (b) The effect of the amount of Ru on the photocatalytic HER performance of **[Co–Ni]** for 1 h.

Table 4.4: Comparisons of the photocatalytic hydrogen evolution activities of various heterogeneous catalyst systems.

Catalyst	PS	Electron donor	Activity (μmol/g/h)	Ref
[Co–Ni]	Ru	Ascorbic Acid	30,029	This work
[Co–Fe]	Ru	Ascorbic Acid	216	This work
[Co–Co]	Ru	Ascorbic Acid	617	This work
PBA–TiO_2 Janus	–	TEOA	198	[70]
g-C_3N_4–Fe_2N nanocomposite	–	TEOA	88.7	[91]
Co_3O_4	Eosin Y	TEOA	5,552	[125]
Co_3O_4	–	Ethanol	2000	[126]
PBA/CdS	–	Lactic acid	57,288	[90]
$CoNiS_x$-CN	–	TEOA	2366	[127]
Co_2C nanoflakes	CdSe/CdS QDs	TEA	18,000	[62]
azine-based N_x-COFs	–	TEOA	782	[128]
CoP-CdS/g-C_3N_4	–	TEOA	23,536	[129]
MoS_2/RGO	[ZnTMPyP]4+	TEOA	2560	[130]
2D–2D SnS_2/TiO_2	–	methanol	652.4	[63]
ReS_2 NWs	–	Na_2S–Na_2SO_3	13,023	[131]
NiS/$Zn_xCd_{1-x}S$	–	Na_2S–Na_2SO_3	16,780	[132]
Ni_xCd_yS	–	Na_2S–Na_2SO_3	8,450	[92]
NiO	Eosin Y	TEOA	7,757	[125]
COF–Cobaloxime hybrid		TEOA	163	[133]

4.3.6 Effect of pH on Photocatalytic HER

The effect of pH on the photocatalytic HER performance of **[Co–Ni]** was investigated in a pH range of 2.6 – 10 when a constant amount of 2 mg catalyst and 7.5 mg ruthenium photosensitizer are used (Figure 4.15). The highest activity is attained at pH 5.0, followed by that at pH 4.0 (5,142 μmol g^{-1} h^{-1}). The decrease in photocatalytic HER activity at pH less than 4 is due to slower reductive quenching of excited Ru species by ascorbic acid, while the reason for the decline at pH greater than 5 is because the protonation of reduced Co(I) species is less-likely in basic media.[21], [134] A similar result is also obtained by the cobaloxime-based hydrogen evolution catalytic system in ascorbate solution in previous studies.[21], [135], [136] The similarity in the coordination spheres of cobalt sites in cobaloxime with **[Co–Ni]**, and the trend in pH-dependent activities suggest that both catalysts evolve hydrogen through a similar mechanism, which involves the reduction of cobalt site, the formation of a Co(III)-H species, and then the evolution of H_2.[51], [137]

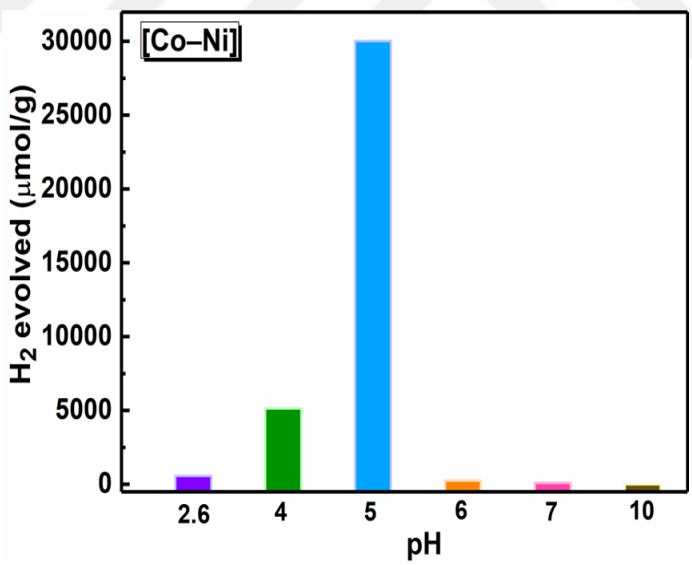

Figure 4.15: The effect of pH on the photocatalytic HER performance of **[Co–Ni]** (2 mg) for 1 h.

4.3.7 Band Alignment between $[Ru(bpy)_3]^{2+}$ and the Catalyst

The feasibility of the proposed system for photocatalytic water oxidation was further evaluated from the band alignment of the Ruthenium photosensitizer and **[Co–Ni]** (Figure 4.16c). To extract the band energy levels, the HOMO and LUMO levels of $[Ru(bpy)_3]^{2+}$ are obtained from literature,[138] and the band gap (2.49 eV) is similar to our UV-vis spectroscopy measurement

(Figure 4.16b). The reduction onset potential of the **[Co–Ni]** is estimated to be −0.37 V_{RHE} by LSV measurement (Figure 4.16a). Upon light illumination, Ru PS is excited, and the holes in the HOMO of Ru PS are consumed by ascorbic acid (oxidized to dehydroascorbic acid). At the same time, the electrons in the LUMO level of the PS are efficiently transferred to **[Co–Ni]** to activate it for the water reduction process.

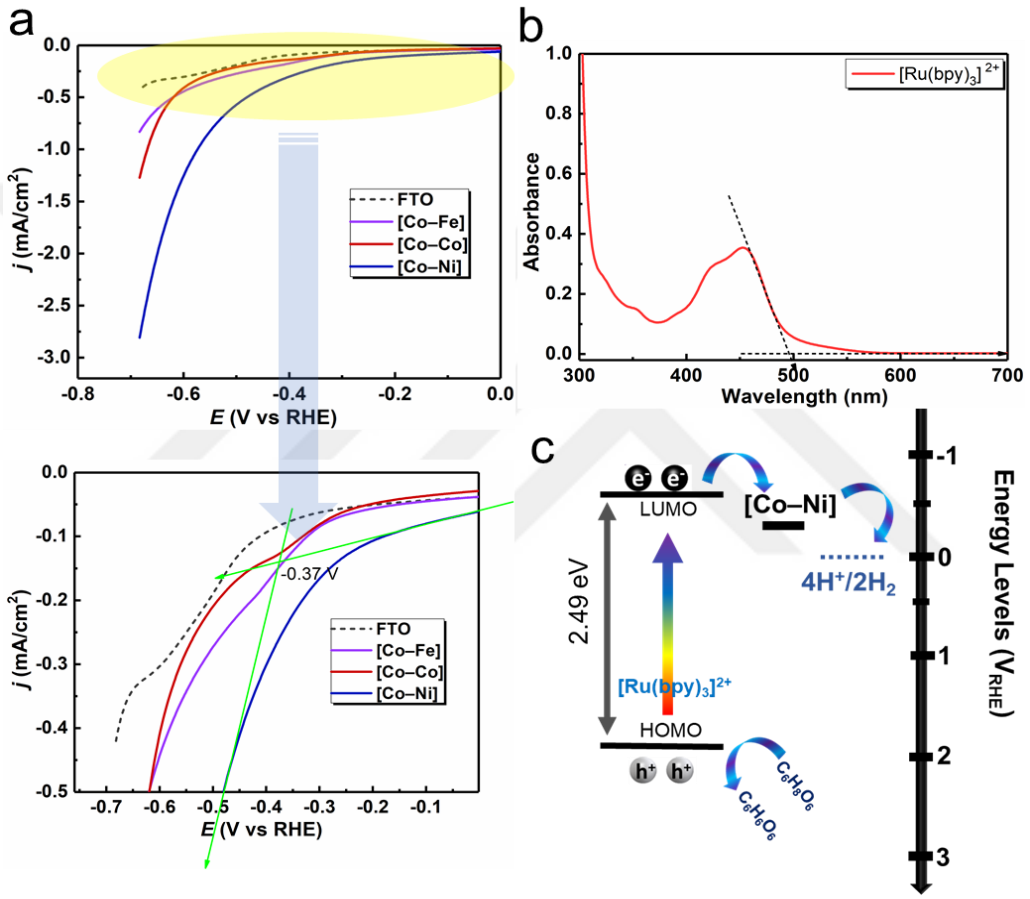

Figure 4.16: (a) LSV profiles and the zoomed onset potential of **[Co–Ni]**. (b) UV-Vis spectra of $[Ru(bpy)_3]^{2+}$ in ascorbic acid solution, showing the absorbance tail of around 500 nm. (c) Extracted energy band diagram of **[Co–Ni]** for the photocatalytic hydrogen reduction process, involving the electron transfer mechanism.

4.3.8 Control Experiment

We also performed photocatalytic studies on **[Zn–Ni]**, in which all cobalt sites in **[Co–Ni]** are replaced with Zn ions, in order to rule out the possibility of the role of nickel sites as catalytic sites. As expected, **[Zn–Ni]** exhibits a poor photocatalytic HER activity (87 μmol g^{-1} h^{-1}), almost similar

to the $[Ru(bpy)_3]Cl_2$/ascorbic acid couple, which confirms that the catalytic hydrogen evolution process takes place solely on cobalt sites (Figure 4.17a). The absence of MMCT bands in **[Zn–Ni]** suggests that there is no electron transfer between the Ni and Zn sites. The presence of the MMCT feature in the UV-Vis absorption profile of **[Co–Ni]**, however, suggests that nickel sites play a significant electronic role in enhancing the catalytic activity and stability due to efficient electronic communication with the cobalt sites (Figure 4.17b). The assignment of the bands in the visible region of **[Co–Ni]** to MMCT is confirmed by the absence of peaks in the same region of the UV-Vis spectra of the precursors (Figure 4.17c).

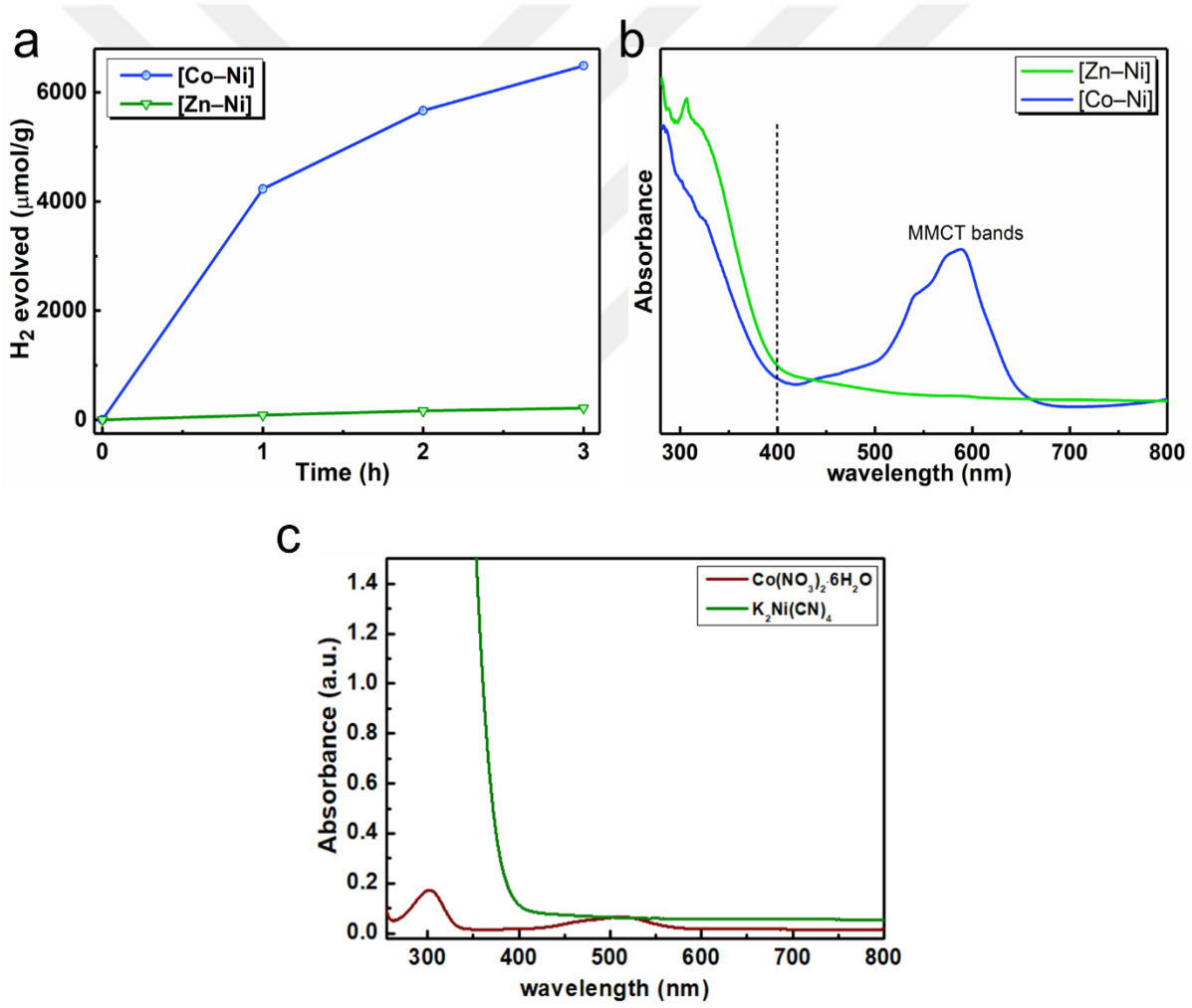

Figure 4.17: (a) Comparison of photocatalytic HER performance of **[Co–Ni]** and **[Zn–Ni]**. Conditions: 10 mg Catalyst, 100 mM ascorbic acid, pH 5, 1 mM $[Ru(bpy)_3]Cl_2$, and 100 mW cm^{-2} white light source. (b) Diffuse reflectance UV-Vis spectra of **[Co–Ni]** and **[Zn–Ni]**. (c) UV-Vis absorption spectra of 10 mM aqueous solution of $Co(NO_3)_2{\cdot}6H_2O$ and $K_2Ni(CN)_4$.

4.3.9 Post-Catalytic Characterization

The activity of **[Co–Ni]** remains essentially unchanged over a 6 h (3 h × 2 cycles) irradiation (Figure 4.12). The addition of only Ru PS into the reaction chamber after the first cycle does not yield an observable increase in the activity, thereby implying that the saturation in the activity is due to the consumption of ascorbic acid after the first hour of each cycle (Figure 4.18).

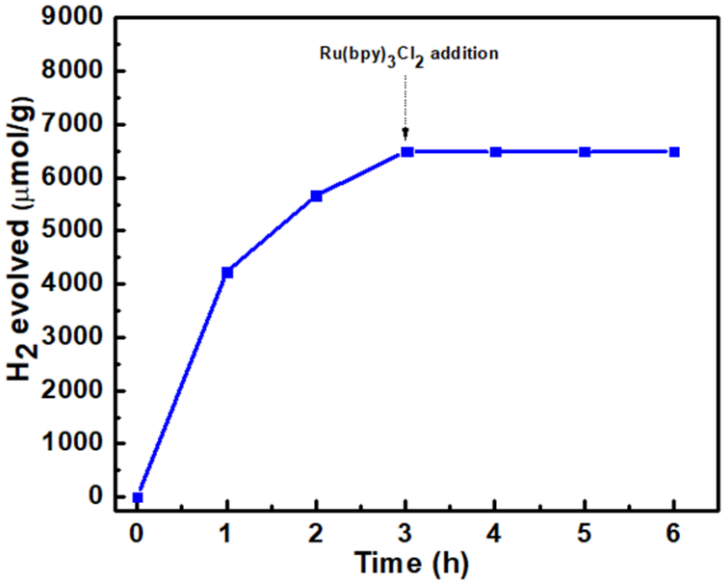

Figure 4.18: Photocatalytic HER activity of **[Co–Ni]** upon addition of only 1 mM $[Ru(bpy)_3]Cl_2$, into the reaction mixture after 3 hours of illumination.

After the photocatalytic HER study, post-catalytic FTIR, PXRD and XPS tests were carried out to establish the catalysts' stability. Post-catalytic PXRD analysis of **[Co–Ni]** revealed that the 2D structure is retained under photocatalytic conditions (Figure 4.19). There is no apparent change between the Co2p and Ni2p peaks of pristine and post-catalytic XPS signals of **[Co–Ni]** (Figure 4.8), indicating that the metal sites are intact after photocatalysis, and the absence of a peak in the 529–530 region of the O1s spectra rules out the possible transformation of cyanide-based structure into cobalt oxides. [70], [139] Similar results were also obtained for post **[Zn–Ni]**, **[Co–Fe]**, and **[Co–Co]** (Figure 4.9-4.11). Similarly, the FTIR spectra of all samples (Figure 4.20) remain unchanged after photocatalytic experiments. The sharp increase in the υ(CN) at 2,098 cm^{-1} for post-catalytic **[Co–Fe]** sample is due to the reduction of Fe^{3+} sites to Fe^{2+},[115] which is also reflected in the Fe 2p XPS signals.

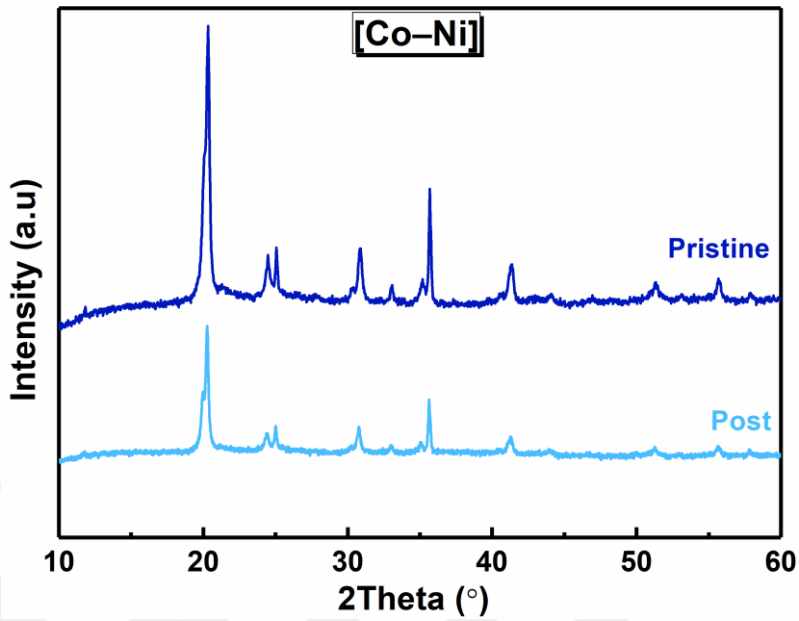

Figure 4.19: PXRD spectra of the pristine and post-catalytic samples of **[Co–Ni]**.

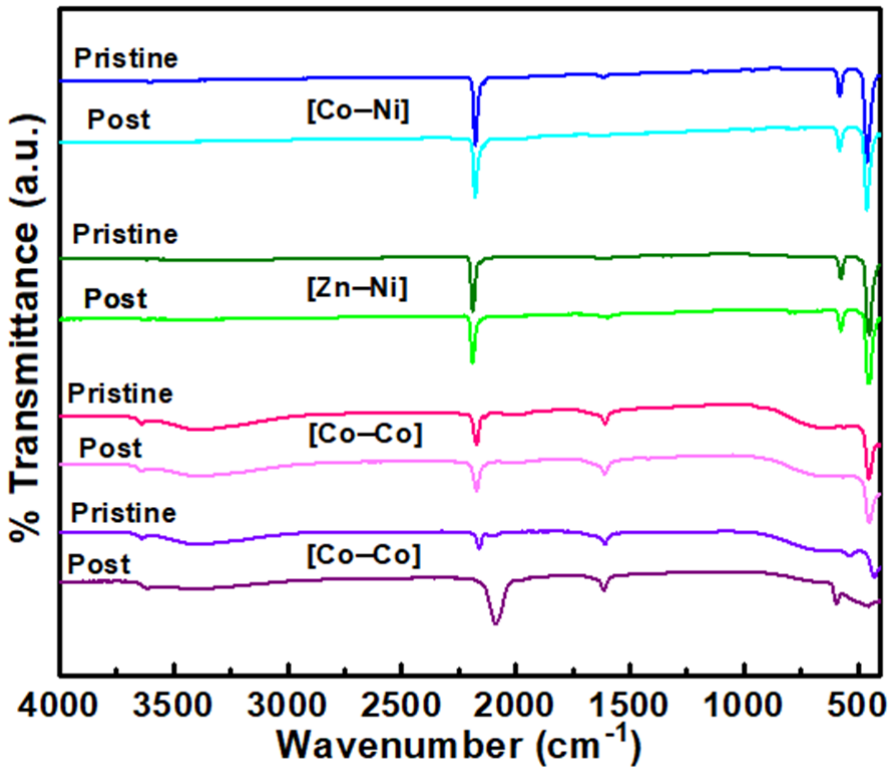

Figure 4.20: ATR-FTIR spectra of the pristine and post-catalytic samples of the compounds showing the full spectrum ranging from 4000 to 400 cm^{-1}.

4.3.10 Electrocatalytic HER

We performed hydrogen evolution studies also under electrocatalytic conditions. As shown in the LSV curve at pH 7 (Figure 4.21a), **[Co–Ni]** displays a better electrocatalytic performance, requiring an overpotential of 0.55 mV to achieve a current density of 0.8 mA cm^{-2}, which is comparably lower than **[Co–Co]** (0.65 mV) and **[Co–Fe]** (0.68 mV), suggesting an enhanced HER kinetics due to the high active surface-sites of **[Co–Ni]**. The enhancement in current density caused by the addition of TFA into the electrolyte solution (pH 1) signifies an increased H_2 evolution (Figure 4.21b).[54] Although the overall electrocatalytic performances are relatively low due to the reduced conductivity by the Nafion binder used in the electrode preparation and the loose physical interaction between the catalyst and the electrode surface, an activity trend, **[Co–Ni]** > **[Co–Co]** > **[Co–Fe]** is obtained similar to photocatalytic studies.

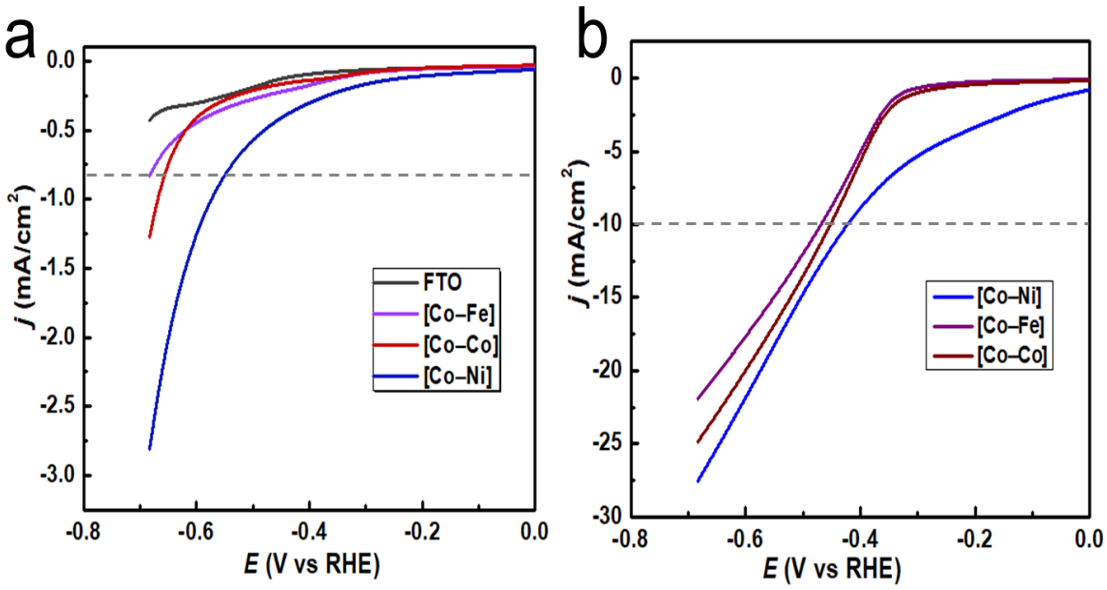

Figure 4.21: LSV curves of the compounds on a FTO electrode in 0.1 M KPi electrolyte at pH 7 at a scan rate of 50 mVs^{-1}. (b) LSV curve of the compounds on a FTO electrode upon addition of 10 mM Trifluoroacetic acid (TFA) into the 0. 1 M KPi electrolyte. Conditions: FTO (WE), Pt mesh (CE), Ag/AgCl (RE) in 0.1 M PBS (pH 7) containing 1 M KNO_3 as the supporting electrolyte. All the potentials are converted to RHE using the relation $E_{RHE} = E_{AgCl} + 0.059 \times pH + E^{\theta}_{AgCl}$, where E^{θ}_{AgCl} = 0.198 V vs NHE at T = 25 ºC.[140]

CHAPTER 5.

5.0 CONCLUSIONS

5.1 Summary

In summary, PBAs are a promising class of heterogeneous catalysts for OER and HER due to their simple synthetic methodology, impressive stability, tunable metal sites, and fast electron transfer from Fe to catalytic Co sites through the short cyanide bridge. Despite the progress in the application of PBAs as water splitting catalysts, the relationship between the activity and coordination environment of the active site is still lacking. Hence, our desire in this study is to understand how the synthetic tuning of the coordination environment of the catalytic sites affects the rational design of a highly-active PBA catalyst. This gap in the application of PBAs for water splitting was explored by using two strategies referred to as ligand-engineering and employing a 2D cyanide-based compound. The OER and HER catalytic activities were examined with photocatalysis using the well-established $[Ru(bpy)_3]^{2+}$ as the photosensitizer, and supporting electrochemical measurements were performed.

(i) Ligand-engineering: We showed that the intrinsic water oxidation activity of the regular Co−Fe PBA catalyst could be tuned by the coordination of bidentate pyridyl groups to the catalytic cobalt sites. Cobalt-mono(bipyridyl) precursors are reacted with hexacyanoferrate complex to prepare **[Cobpy−Fe]** and **[Cophen−Fe]**, which possess cobalt sites coordinated to pyridyl and −NC groups as well as water molecules. In **[Cobpy−Fe]** and **[Cophen−Fe]**, structures with lower dimensionality and less crystalline nature are observed compared to regular **[Co−Fe]**. These compounds also exhibit a higher number of Co sites compared to **[Co−Fe]**, which is reflected in their photocatalytic water oxidation activities. Due to the well-tuned electronic effect caused by the electron-withdrawing bidentate pyridyl groups, the photocatalytic activities of **[Cobpy−Fe]** and **[Cophen−Fe]** outperform **[Co−Fe]**. The electronic effect generated by bidentate pyridyl ligand coordination fosters water oxidation by (i) increasing the electrophilicity of the Co(IV)- oxo species to the nucleophilic attack of water through their strong π-accepting ability and (ii) sufficiently stabilizing the highly valent Co(IV) state by strong sigma donation and bidentate coordination.

Electronic structure calculations support experimental observations by confirming that the coordination of bidentate pyridyl groups to the catalytic cobalt sites can sufficiently lower the LUMO energy barrier required for the crucial O−O bond formation in water oxidation kinetics. In addition to this enhanced activity, another interesting finding in this work is that free coordination or aqua coordination on the catalytic cobalt sites in Co−Fe PBA is essential for water oxidation. Molecular **[Cobpy2−Fe]** and **[Cophen2−Fe]** compounds designed by reacting cobalt−bis(bipyridyl) with hexacyanoferrate precursor show no oxygen evolution since the coordination sphere of cobalt sites are entirely decorated with bipyridyl and cyanide groups. Furthermore, the complete inactivity of **[Cobpy2−Fe]** and **[Cophen2−Fe]** confirms that cyanide-bridged compounds are stable and do not release their cyanide groups during photocatalysis.

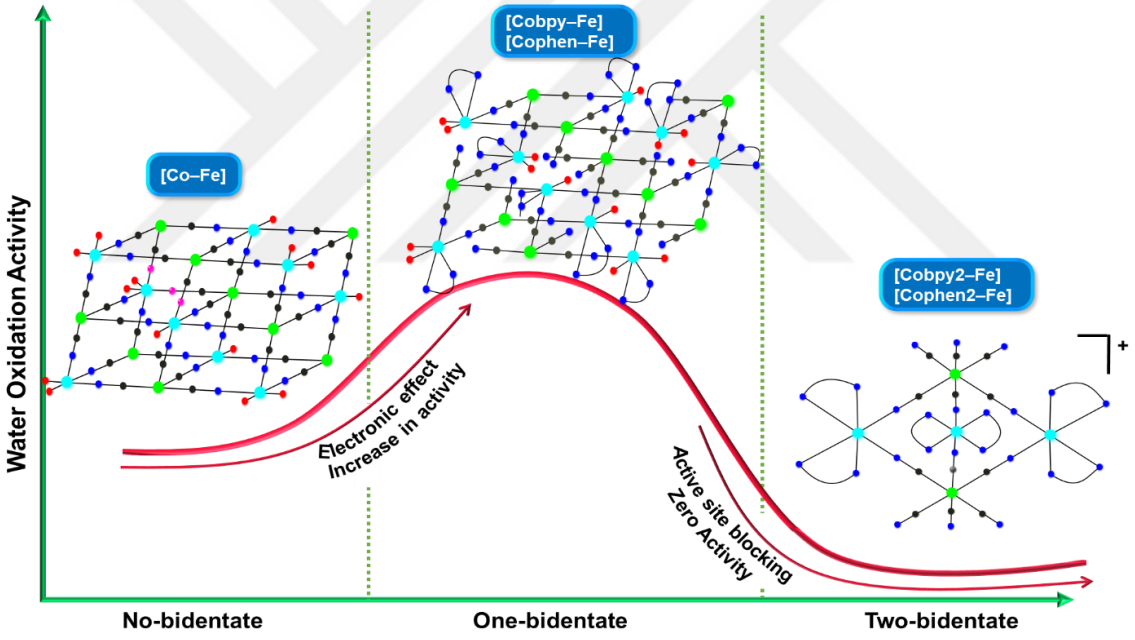

Figure 5.1: Schematic diagram showing the relationship between the well-defined ligand coordination environment and activity. Reprinted with permission from Ref. [70]. Copyright 2022. American Chemical Society.

(ii) Employing a 2D cyanide-based compound: We report for the first time a 2D layered **[Co–Ni]** that performs as an efficient and robust HER noble-metal-free catalyst. **[Co–Ni]** was synthesized with a high yield via one-step solution chemistry using a square planar tetracyanonickelate precursor, $[Ni(CN)_4]^{2-}$. **[Co–Ni]** offers a blend of merits of a cyanide-based network and the unique surface/electronic properties of a 2D architecture. Structural and

morphological characterization of **[Co–Ni]** reveals a trans-CoN_4O_2 coordination environment, in which all the cobalt sites are active due to coordination to two water molecules at the axial position, and the 2D layers are well spaced to allow easy access to H_2O and H^+ to al the catalytic cobalt sites. Correspondingly, the cyanide-bridge coordination provides stability and efficient electron transfer between the metal sites. Owing to these unique features of the coordination environment, **[Co–Ni]** exhibits activity as high as 30,029 μmol g^{-1} h^{-1}, which is much higher than 3D **[Co–Fe]** and **[Co–Co]**. **[Co–Ni]** also performs much better than most high-performing HER catalysts reported in the literature. **[Co–Ni]** displays excellent stability as it retains its activity during cycle experiments and post-catalytic studies reveal that the cyanide network is preserved after photocatalysis.

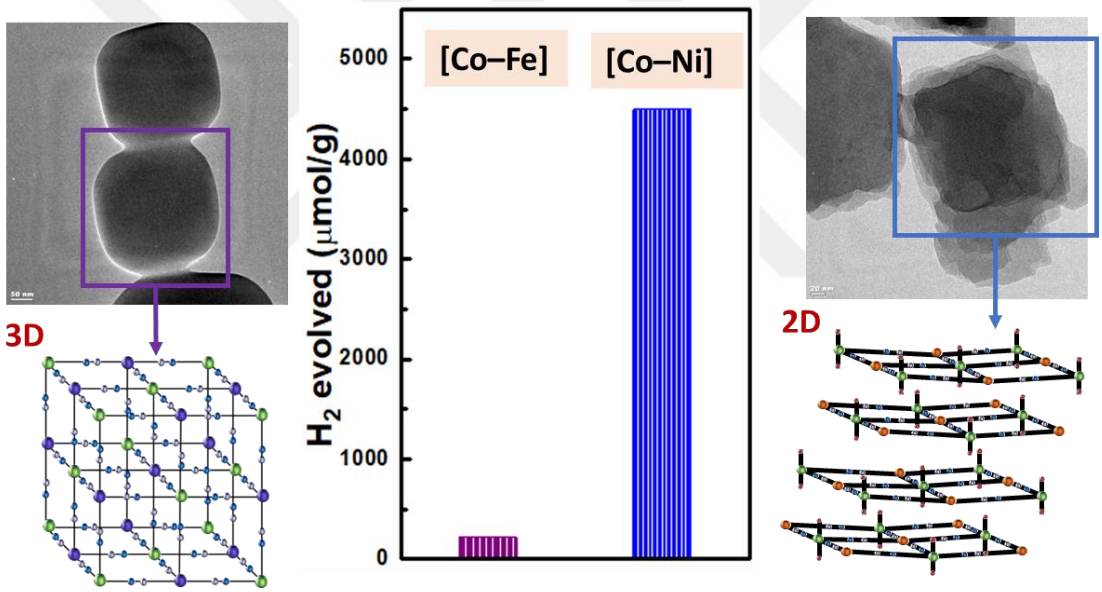

Figure 5.2: Schematic diagram showing the relationship in structure and catalytic activity by switching from 3D to 2D.

5.2 Remarks

Tuning the coordination environment of the catalytic sites using the ligand engineering approach is a strategic pathway to enhance the water oxidation activity of PBA, as the realistic TOF reaches up to 1.3 s^{-1}. Although this is still lower than OEC in natural PSII, which can exhibit TOF up to 400 s^{-1}, this is a record in a photocatalytic water oxidation study using PBAs. This study, thus, demonstrates that PBAs have the potential to reach higher TOF values for water oxidation. Furthermore, a TOF of 1.3 s^{-1} was achieved using a simple phenanthroline ligand, and this activity

could be superbly improved by using a higher donor-acceptor bidentate ligand and reducing the blocking effect of the ligands.

The limited number of surface-active sites and low conductivity, which are significant challenges that diminish the intrinsic catalytic activity of 3D PBAs, are solved by switching to 2D cyanide coordination compounds. There is a 36 times increase in the active surface area and an exceptional change in the surface electronic properties by transforming from 3D to 2D. Furthermore, a photocatalytic HER activity of 30,029 μmol g^{-1} h^{-1} exhibited by this 2D framework is the best ever recorded intrinsic photocatalytic activity in a cyanide framework without coupling with a semiconductor or decomposing the cyanide framework.

Overall, both of the above-mentioned strategies aim to explore the relationship between the catalytic activity of PBA and the structural coordination environment of the active site. Tuning the coordination environment around the catalytic sites by using structural parameters such as ligand-engineering and altering the dimensionality has further established cyanide-based catalysts as highly active non-noble catalysts for water splitting and provides a unique strategy for optimizing the activity of PB-based catalysts.

CHAPTER 6.

6.0 BIBLIOGRAPHY

[1] D. L. Ashford *et al.*, "Molecular Chromophore-Catalyst Assemblies for Solar Fuel Applications," *Chem. Rev.*, vol. 115, no. 23, pp. 13006–13049, 2015, doi: 10.1021/acs.chemrev.5b00229.

[2] J. K. Stolarczyk, S. Bhattacharyya, L. Polavarapu, and J. Feldmann, "Challenges and Prospects in Solar Water Splitting and CO_2 Reduction with Inorganic and Hybrid Nanostructures," *ACS Catal.*, vol. 8, no. 4, pp. 3602–3635, 2018, doi: 10.1021/acscatal.8b00791.

[3] S. Dutta, "Review on Solar Hydrogen: Its Prospects and Limitations," *Energy and Fuels*, vol. 35, no. 15, pp. 11613–11639, 2021, doi: 10.1021/acs.energyfuels.1c00823.

[4] P. Ganguly *et al.*, "2D Nanomaterials for Photocatalytic Hydrogen Production," *ACS Energy Lett.*, vol. 4, no. 7, pp. 1687–1709, 2019, doi: 10.1021/acsenergylett.9b00940.

[5] M. D. Kärkäs, O. Verho, E. V. Johnston, and B. Åkermark, "Artificial photosynthesis: Molecular systems for catalytic water oxidation," *Chem. Rev.*, vol. 114, no. 24, pp. 11863–12001, 2014, doi: 10.1021/cr400572f.

[6] Q. Wang and K. Domen, "Particulate Photocatalysts for Light-Driven Water Splitting: Mechanisms, Challenges, and Design Strategies," *Chem. Rev.*, vol. 120, no. 2, pp. 919–985, 2020, doi: 10.1021/acs.chemrev.9b00201.

[7] O. J. Guerra, J. Eichman, J. Kurtz, and B. M. Hodge, "Cost Competitiveness of Electrolytic Hydrogen," *Joule*, vol. 3, no. 10, pp. 2425–2443, 2019, doi: 10.1016/j.joule.2019.07.006.

[8] S. Anantharaj, S. R. Ede, K. Sakthikumar, K. Karthick, S. Mishra, and S. Kundu, "Recent Trends and Perspectives in Electrochemical Water Splitting with an Emphasis on Sulfide, Selenide, and Phosphide Catalysts of Fe, Co, and Ni: A Review," *ACS Catal.*, vol. 6, no. 12, pp. 8069–8097, 2016, doi: 10.1021/acscatal.6b02479.

[9] S. Han, Q. Yun, S. Tu, L. Zhu, W. Cao, and Q. Lu, "Metallic ruthenium-based

nanomaterials for electrocatalytic and photocatalytic hydrogen evolution," *J. Mater. Chem. A*, vol. 7, no. 43, pp. 24691–24714, 2019, doi: 10.1039/c9ta06178a.

[10] S. Chen *et al.*, "Mn-Doped RuO_2 Nanocrystals as Highly Active Electrocatalysts for Enhanced Oxygen Evolution in Acidic Media," *ACS Catal.*, vol. 10, no. 2, pp. 1152–1160, 2020, doi: 10.1021/acscatal.9b04922.

[11] E. Oakton *et al.*, "IrO_2-TiO_2: A High-Surface-Area, Active, and Stable Electrocatalyst for the Oxygen Evolution Reaction," *ACS Catal.*, vol. 7, no. 4, pp. 2346–2352, 2017, doi: 10.1021/acscatal.6b03246.

[12] Z. Li, Y. Yao, X. Gao, H. Bai, and X. Meng, "Interfacial charge transfer and enhanced photocatalytic mechanisms for Pt nanoparticles loaded onto sulfur-doped g-C_3N_4 in H_2 evolution," *Mater. Today Energy*, vol. 22, p. 100881, 2021, doi: 10.1016/j.mtener.2021.100881.

[13] J. P. McEvoy and G. W. Brudvig, "Water-splitting chemistry of photosystem II," *Chem. Rev.*, vol. 106, no. 11, pp. 4455–4483, 2006, doi: 10.1021/cr0204294.

[14] J. D. Blakemore, R. H. Crabtree, and G. W. Brudvig, "Molecular Catalysts for Water Oxidation," *Chem. Rev.*, vol. 115, no. 23, pp. 12974–13005, 2015, doi: 10.1021/acs.chemrev.5b00122.

[15] K. Kawakami, Y. Umena, N. Kamiya, and J. R. Shen, "Structure of the catalytic, inorganic core of oxygen-evolving photosystem II at 1.9 resolution," *J. Photochem. Photobiol. B Biol.*, vol. 104, no. 1–2, pp. 9–18, 2011, doi: 10.1016/j.jphotobiol.2011.03.017.

[16] K. N. Ferreira, T. M. Iverson, K. Maghlaoui, J. Barber, Iwata, and So, "Architecture of the Photosynthetic Oxygen-Evolving Center," *Science (80-.).*, vol. 303, pp. 1831–1838, 2004, doi: 10.1111/1467-8357.00184.

[17] E. M. Sproviero, J. A. Gascón, J. P. McEvoy, G. W. Brudvig, and V. S. Batista, "Quantum mechanics/molecular mechanics study of the catalytic cycle of water splitting in photosystem II," *J. Am. Chem. Soc.*, vol. 130, no. 11, pp. 3428–3442, 2008, doi: 10.1021/ja076130q.

[18] R. De Wijn and H. J. Van Gorkom, “The rate of charge recombination in Photosystem II,” *Biochim. Biophys. Acta - Bioenerg.*, vol. 1553, no. 3, pp. 302–308, 2002, doi: 10.1016/S0005-2728(02)00183-4.

[19] V. Artero, M. Chavarot-Kerlidou, and M. Fontecave, “Splitting water with cobalt,” *Angew. Chemie - Int. Ed.*, vol. 50, no. 32, pp. 7238–7266, 2011, doi: 10.1002/anie.201007987.

[20] D. Gust, T. A. Moore, and A. L. Moore, “Solar fuels via artificial photosynthesis,” *Acc. Chem. Res.*, vol. 42, no. 12, pp. 1890–1898, 2009, doi: 10.1021/ar900209b.

[21] M. Natali, “Elucidating the Key Role of pH on Light-Driven Hydrogen Evolution by a Molecular Cobalt Catalyst,” *ACS Catal.*, vol. 7, no. 2, pp. 1330–1339, 2017, doi: 10.1021/acscatal.6b03087.

[22] S. Yusuf and F. Jiao, “Effect of the support on the photocatalytic water oxidation activity of cobalt oxide nanoclusters,” *ACS Catal.*, vol. 2, no. 12, pp. 2753–2760, 2012, doi: 10.1021/cs300581k.

[23] S. Chakraborty, E. H. Edwards, B. Kandemir, and K. L. Bren, “Photochemical Hydrogen Evolution from Neutral Water with a Cobalt Metallopeptide Catalyst,” *Inorg. Chem.*, vol. 58, no. 24, pp. 16402–16410, 2019, doi: 10.1021/acs.inorgchem.9b02067.

[24] Y. J. Yuan, Z. T. Yu, D. Q. Chen, and Z. G. Zou, “Metal-complex chromophores for solar hydrogen generation,” *Chem. Soc. Rev.*, vol. 46, no. 3, pp. 603–631, 2017, doi: 10.1039/c6cs00436a.

[25] Y. Bai, K. Hippalgaonkar, and R. S. Sprick, “Organic materials as photocatalysts for water splitting,” *J. Mater. Chem. A*, vol. 9, no. 30, pp. 16222–16232, 2021, doi: 10.1039/d1ta03710b.

[26] F. E. Osterloh, “Inorganic materials as catalysts for photochemical splitting of water,” *Chem. Mater.*, vol. 20, no. 1, pp. 35–54, 2008, doi: 10.1021/cm7024203.

[27] R. Gueret *et al.*, “Challenging the $[Ru(bpy)_3]^{2+}$ Photosensitizer with a Triazatriangulenium Robust Organic Dye for Visible-Light-Driven Hydrogen Production in Water,” *ACS Catal.*, vol. 8, no. 5, pp. 3792–3802, 2018, doi: 10.1021/acscatal.7b04000.

[28] T. G. Ulusoy Ghobadi *et al.*, “A Noble-Metal-Free Heterogeneous Photosensitizer-Relay Catalyst Triad That Catalyzes Water Oxidation under Visible Light,” *Angew. Chemie*, vol. 130, no. 52, pp. 17419–17423, 2018, doi: 10.1002/ange.201811570.

[29] T. Oshima *et al.*, “An Artificial Z-Scheme Constructed from Dye-Sensitized Metal Oxide Nanosheets for Visible Light-Driven Overall Water Splitting,” *J. Am. Chem. Soc.*, vol. 142, no. 18, pp. 8412–8420, 2020, doi: 10.1021/jacs.0c02053.

[30] M. D. Brady, R. N. Sampaio, D. Wang, T. J. Meyer, and G. J. Meyer, “Dye-Sensitized Hydrobromic Acid Splitting for Hydrogen Solar Fuel Production,” *J. Am. Chem. Soc.*, vol. 139, no. 44, pp. 15612–15615, 2017, doi: 10.1021/jacs.7b09367.

[31] T. G. Ulusoy Ghobadi *et al.*, “A Robust, Precious-Metal-Free Dye-Sensitized Photoanode for Water Oxidation: A Nanosecond-Long Excited-State Lifetime through a Prussian Blue Analogue,” *Angew. Chemie*, vol. 132, no. 10, pp. 4111–4119, 2020, doi: 10.1002/ange.201914743.

[32] C. Förster and K. Heinze, “Photophysics and photochemistry with Earth-abundant metals-fundamentals and concepts,” *Chem. Soc. Rev.*, vol. 49, no. 4, pp. 1057–1070, 2020, doi: 10.1039/c9cs00573k.

[33] D. M. Arias-Rotondo and J. K. McCusker, “The photophysics of photoredox catalysis: A roadmap for catalyst design,” *Chem. Soc. Rev.*, vol. 45, no. 21, pp. 5803–5820, 2016, doi: 10.1039/c6cs00526h.

[34] O. S. Wenger, “Is Iron the New Ruthenium?,” *Chem. - A Eur. J.*, vol. 25, no. 24, pp. 6043–6052, 2019, doi: 10.1002/chem.201806148.

[35] C. K. Prier, D. A. Rankic, and D. W. C. MacMillan, “Visible light photoredox catalysis with transition metal complexes: Applications in organic synthesis,” *Chem. Rev.*, vol. 113, no. 7, pp. 5322–5363, 2013, doi: 10.1021/cr300503r.

[36] C. R. Bock *et al.*, “Estimation of excited-state redox potentials by electron-transfer quenching. Application of electron-transfer theory to excited-state redox processes,” *J. Am. Chem. Soc.*, vol. 101, no. 17, pp. 4815–4824, 1979, doi: 10.1021/ja00511a007.

[37] A. Juris, V. Balzani, P. Belser, and A. von Zelewsky, “Characterization of the Excited

State Properties of Some New Photosensitizers of the Ruthenium (Polypyridine) Family," *Helv. Chim. Acta*, vol. 64, no. 7, pp. 2175–2182, 1981, doi: 10.1002/hlca.19810640723.

[38] A. Kudo and Y. Miseki, "Heterogeneous photocatalyst materials for water splitting," *Chem. Soc. Rev.*, vol. 38, no. 1, pp. 253–278, 2009, doi: 10.1039/b800489g.

[39] F. A. Pasha, A. Poater, S. V. C. Vummaleti, T. de Bruin, J. M. Basset, and L. Cavallo, "Revisiting O–O Bond Formation through Outer-Sphere Water Molecules versus Bimolecular Mechanisms in Water-Oxidation Catalysis (WOC) by Cp*Ir Based Complexes," *Eur. J. Inorg. Chem.*, no. 15, pp. 2093–2100, 2019, doi: 10.1002/ejic.201800500.

[40] M. Murakami, D. Hong, T. Suenobu, S. Yamaguchi, T. Ogura, and S. Fukuzumi, "Catalytic mechanism of water oxidation with single-site ruthenium-heteropolytungstate complexes," *J. Am. Chem. Soc.*, vol. 133, no. 30, pp. 11605–11613, 2011, doi: 10.1021/ja2024965.

[41] L. Duan *et al.*, "A molecular ruthenium catalyst with water-oxidation activity comparable to that of photosystem II," *Nat. Chem.*, vol. 4, no. 5, pp. 418–423, 2012, doi: 10.1038/nchem.1301.

[42] A. Harriman, I. J. Pickering, J. M. Thomas, and P. A. Christensen, "Metal oxides as heterogeneous catalysts for oxygen evolution under photochemical conditions," *J. Chem. Soc. Faraday Trans. 1 Phys. Chem. Condens. Phases*, vol. 84, no. 8, pp. 2795–2806, 1988, doi: 10.1039/F19888402795.

[43] M. D. Kärkäs, E. V. Johnston, O. Verho, and B. Akermark, "Artificial photosynthesis: From nanosecond electron transfer to catalytic water oxidation," *Acc. Chem. Res.*, vol. 47, no. 1, pp. 100–111, 2014, doi: 10.1021/ar400076j.

[44] X. B. Han *et al.*, "Polyoxometalate-based cobalt-phosphate molecular catalysts for visible light-driven water oxidation," *J. Am. Chem. Soc.*, vol. 136, no. 14, pp. 5359–5366, 2014, doi: 10.1021/ja412886e.

[45] G. S. Hutchings *et al.*, "In situ formation of cobalt oxide nanocubanes as efficient oxygen evolution catalysts," *J. Am. Chem. Soc.*, vol. 137, no. 12, pp. 4223–4229, 2015, doi:

10.1021/jacs.5b01006.

[46] H. Tabe, A. Kitase, and Y. Yamada, “Utilization of core-shell nanoparticles to evaluate subsurface contribution to water oxidation catalysis of $[Co^{II}(H_2O)_2]_{1.5}[Co^{III}(CN)_6]$ nanoparticles,” *Appl. Catal. B Environ.*, vol. 262, p. 118101, 2020, doi: 10.1016/j.apcatb.2019.118101.

[47] E. P. Alsaç, E. Ülker, S. V. K. Nune, Y. Dede, and F. Karadas, “Tuning the Electronic Properties of Prussian Blue Analogues for Efficient Water Oxidation Electrocatalysis: Experimental and Computational Studies,” *Chem. - A Eur. J.*, vol. 24, no. 19, pp. 4856–4863, 2018, doi: 10.1002/chem.201704933.

[48] G. Zuo *et al.*, “Enhanced photocatalytic water oxidation by hierarchical 2D-Bi_2MoO_6@2D-MXene Schottky junction nanohybrid,” *Chem. Eng. J.*, vol. 403, no. July 2020, p. 126328, 2021, doi: 10.1016/j.cej.2020.126328.

[49] B. Limburg, E. Bouwman, and S. Bonnet, “Rate and Stability of Photocatalytic Water Oxidation using $[Ru(bpy)_3]^{2+}$ as Photosensitizer,” *ACS Catal.*, vol. 6, no. 8, pp. 5273–5284, 2016, doi: 10.1021/acscatal.6b00107.

[50] S. Fukuzumi, J. Jung, Y. Yamada, T. Kojima, and W. Nam, “Homogeneous and Heterogeneous Photocatalytic Water Oxidation by Persulfate,” *Chem. - An Asian J.*, vol. 11, no. 8, pp. 1138–1150, 2016, doi: 10.1002/asia.201501329.

[51] J. L. Dempsey, B. S. Brunschwig, J. R. Winkler, and H. B. Gray, “Hydrogen evolution catalyzed by cobaloximes,” *Acc. Chem. Res.*, vol. 42, no. 12, pp. 1995–2004, 2009, doi: 10.1021/ar900253e.

[52] N. Cheng *et al.*, “Platinum single-atom and cluster catalysis of the hydrogen evolution reaction,” *Nat. Commun.*, vol. 7, pp. 1–9, 2016, doi: 10.1038/ncomms13638.

[53] X. Y. Yu, Y. Feng, Y. Jeon, B. Guan, X. W. D. Lou, and U. Paik, “Formation of Ni–Co–MoS_2Nanoboxes with Enhanced Electrocatalytic Activity for Hydrogen Evolution,” *Adv. Mater.*, vol. 28, no. 40, pp. 9006–9011, 2016, doi: 10.1002/adma.201601188.

[54] W. R. Mcnamara, Z. Han, P. J. Alperin, W. W. Brennessel, P. L. Holland, and R. Eisenberg, “A Cobalt-Dithiolene Complex for the Photocatalytic and,” *J. Am. Chem. Soc.*,

vol. 133, no. Figure 2, pp. 15368–15371, 2011.

[55] D. Z. Zee, T. Chantarojsiri, J. R. Long, and C. J. Chang, “Metal-Polypyridyl Catalysts for Electro- and Photochemical Reduction of Water to Hydrogen,” *Acc. Chem. Res.*, vol. 48, no. 7, pp. 2027–2036, 2015, doi: 10.1021/acs.accounts.5b00082.

[56] J. C. Fontecilla-camps, A. Volbeda, C. Cavazza, and Y. Nicolet, “Structure / Function Relationships of [NiFe]- and [FeFe]-Hydrogenases,” *Chem. Rev.*, vol. 107, pp. 4273–4303, 2007.

[57] S. Ding *et al.*, “Hemilabile Bridging Thiolates as Proton Shuttles in Bioinspired H_2 Production Electrocatalysts,” *J. Am. Chem. Soc.*, vol. 138, no. 39, pp. 12920–12927, 2016, doi: 10.1021/jacs.6b06461.

[58] F. Gloaguen and T. B. Rauchfuss, “Small molecule mimics of hydrogenases: Hydrides and redox,” *Chem. Soc. Rev.*, vol. 38, no. 1, pp. 100–108, 2009, doi: 10.1039/b801796b.

[59] F. Gloaguen, J. D. Lawrence, and T. B. Rauchfuss, “Biomimetic hydrogen evolution catalyzed by an iron carbonyl thiolate,” *J. Am. Chem. Soc.*, vol. 123, no. 38, pp. 9476–9477, 2001, doi: 10.1021/ja016516f.

[60] Y. Oudart, V. Artero, and J. Pe, “[Ni(xbsms)Ru$(CO)_2Cl_2$]: A Bioinspired Nickel − Ruthenium Functional Model of [NiFe] Hydrogenase,” *Society*, vol. 45, no. 11, pp. 4334–4336, 2006.

[61] M. Chavarot-Kerlidou, P. Chenevier, and V. Artero, “Bio-Organometallic Systems for the Hydrogen Economy: Engineering of Electrode Materials and Light-Driven Devices,” *Bioorganometallic Chem. Appl. Drug Discov. Biocatal. Imaging*, pp. 273–304, 2015, doi: 10.1002/9783527673438.ch09.

[62] Q. Guo *et al.*, “Metallic Co_2C: A promising co-catalyst to boost photocatalytic hydrogen evolution of colloidal quantum dots,” *ACS Catal.*, vol. 8, no. 7, pp. 5890–5895, 2018, doi: 10.1021/acscatal.8b01105.

[63] L. Sun *et al.*, “Role of SnS_2 in 2D-2D SnS_2/TiO_2 Nanosheet Heterojunctions for Photocatalytic Hydrogen Evolution,” *ACS Appl. Nano Mater.*, vol. 2, no. 4, pp. 2144–2151, 2019, doi: 10.1021/acsanm.9b00122.

[70] C. Shi *et al.*, “Modular Construction of Prussian Blue Analog and TiO_2 Dual-Compartment Janus Nanoreactor for Efficient Photocatalytic Water Splitting,” *Adv. Sci.*, vol. 8, no. 7, pp. 1–8, 2021, doi: 10.1002/advs.202001987.

[65] K. R. Dunbar and R. A. Heintz, *Chemistry of transition metal cyanide compounds: Modern perspectives*, vol. 45. 2007.

[66] H. J. Buser, D. Schwarzenbach, W. Peter, and A. Ludi, “The Crystal Structure of Prussian Blue: $Fe_4[Fe(CN)_6]_3 \cdot xH_2O$,” *Inorg. Chem.*, vol. 16, no. 11, pp. 2704–2710, 1977.

[67] F. S. Hegner, J. R. Galán-Mascarós, and N. López, “A Database of the Structural and Electronic Properties of Prussian Blue, Prussian White, and Berlin Green Compounds through Density Functional Theory,” *Inorg. Chem.*, vol. 55, no. 24, pp. 12851–12862, 2016, doi: 10.1021/acs.inorgchem.6b02200.

[68] S. Pintado, S. Goberna-Ferrón, E. C. Escudero-Adán, and J. R. Galán-Mascarós, “Fast and persistent electrocatalytic water oxidation by Co-Fe Prussian blue coordination polymers,” *J. Am. Chem. Soc.*, vol. 135, no. 36, pp. 13270–13273, 2013, doi: 10.1021/ja406242y.

[69] S. Goberna-Ferrón, W. Y. Hernández, B. Rodríguez-García, and J. R. Galán-Mascarós, “Light-driven water oxidation with metal hexacyanometallate heterogeneous catalysts,” *ACS Catal.*, vol. 4, no. 6, pp. 1637–1641, 2014, doi: 10.1021/cs500298e.

[70] A. A. Ahmad, T. G. Ulusoy Ghobadi, M. Buyuktemiz, E. Ozbay, Y. Dede, and F. Karadas, “Light-Driven Water Oxidation with Ligand-Engineered Prussian Blue Analogues,” *Inorg. Chem.*, vol. 61, no. 9, pp. 3931–3941, 2022, doi: 10.1021/acs.inorgchem.1c03531.

[71] T. G. Ulusoy Ghobadi, E. Ozbay, and F. Karadas, “How to Build Prussian Blue Based Water Oxidation Catalytic Assemblies: Common Trends and Strategies,” *Chem. - A Eur. J.*, vol. 27, no. 11, pp. 3638–3649, 2021, doi: 10.1002/chem.202004091.

[72] N. R. De Tacconi, K. Rajeshwar, and R. O. Lezna, “Metal Hexacyanoferrates: Electrosynthesis, in Situ Characterization, and Applications,” *Chem. Mater.*, vol. 15, pp. 3046–3062, 2003.

[73] M. Aksoy, S. V. K. Nune, and F. Karadas, “A Novel Synthetic Route for the Preparation

of an Amorphous Co/Fe Prussian Blue Coordination Compound with High Electrocatalytic Water Oxidation Activity," *Inorg. Chem.*, vol. 55, no. 9, pp. 4301–4307, 2016, doi: 10.1021/acs.inorgchem.6b00032.

[74] Y. Yamada, K. Oyama, R. Gates, and S. Fukuzumi, "High catalytic activity of heteropolynuclear cyanide complexes containing cobalt and platinum ions: Visible-light driven water oxidation," *Angew. Chemie - Int. Ed.*, vol. 54, no. 19, pp. 5613–5617, 2015, doi: 10.1002/anie.201501116.

[75] P. A. Christensen, A. Harriman, P. Neta, and M. C. Richoux, "Photo-oxidation of water using Prussian Blue as catalyst," *J. Chem. Soc. Faraday Trans. 1 Phys. Chem. Condens. Phases*, vol. 81, no. 10, pp. 2461–2466, 1985, doi: 10.1039/F19858102461.

[76] M. Kaneko, N. Takabayahi, and A. Yamada, "Simultaneous Evolution of Hydrogen and Oxygen by Water Photolysis with Prussian Blue and Tris(2,2'-bipyridyl)Ruthenium(ii) Complex," *Chem. Lett.*, pp. 1647–1650, 1982.

[77] J. Guo *et al.*, "Efficient difunctional photocatalyst prepared: In situ from Prussian blue analogues for catalytic water oxidation and visible-light absorption," *Catal. Sci. Technol.*, vol. 8, no. 24, pp. 6375–6383, 2018, doi: 10.1039/c8cy01620h.

[78] F. S. Hegner, D. Cardenas-Morcoso, S. Giménez, N. López, and J. R. Galan-Mascaros, "Level Alignment as Descriptor for Semiconductor/Catalyst Systems in Water Splitting: The Case of Hematite/Cobalt Hexacyanoferrate Photoanodes," *ChemSusChem*, vol. 10, no. 22, pp. 4552–4560, 2017, doi: 10.1002/cssc.201701538.

[79] S. S. Akbari and F. Karadas, "Precious Metal-Free Photocatalytic Water Oxidation by a Layered Double Hydroxide-Prussian Blue Analogue Hybrid Assembly," *ChemSusChem*, vol. 14, no. 2, pp. 679–685, 2021, doi: 10.1002/cssc.202002279.

[80] S. S. Akbari, U. Unal, and F. Karadas, "Photocatalytic Water Oxidation with a CoFe Prussian Blue Analogue-Layered Niobate Hybrid Material," *ACS Appl. Energy Mater.*, vol. 4, no. 11, pp. 12383–12390, 2021, doi: 10.1021/acsaem.1c02188.

[81] T. G. U. Ghobadi *et al.*, "Strong Light–Matter Interactions in Au Plasmonic Nanoantennas Coupled with Prussian Blue Catalyst on $BiVO_4$ for Photoelectrochemical Water

Splitting," *ChemSusChem*, vol. 13, pp. 2577–2588, 2020, doi: 10.1002/cssc.202000294.

[82] G. Gundogdu, T. G. Ulusoy Ghobadi, S. Sadigh Akbari, E. Ozbay, and F. Karadas, "Photocatalytic water oxidation with a Prussian blue modified brown TiO_2," *Chem. Commun.*, vol. 57, no. 4, pp. 508–511, 2021, doi: 10.1039/d0cc07077g.

[83] B. M. Pires, F. S. Hegner, J. A. Bonacin, and J. R. Galán-Mascarós, "Ligand Effects of Penta- And Hexacyanidoferrate-Derived Water Oxidation Catalysts on $BiVO_4$ Photoanodes," *ACS Appl. Energy Mater.*, vol. 3, no. 9, pp. 8448–8456, 2020, doi: 10.1021/acsaem.0c01082.

[84] Z. Kap and F. Karadas, "Visible light-driven water oxidation with a ruthenium sensitizer and a cobalt-based catalyst connected with a polymeric platform," *Faraday Discuss.*, vol. 215, pp. 111–122, 2019, doi: 10.1039/c8fd00166a.

[85] T. G. Ulusoy Ghobadi *et al.*, "A Noble-Metal-Free Heterogeneous Photosensitizer-Relay Catalyst Triad That Catalyzes Water Oxidation under Visible Light," *Angew. Chemie - Int. Ed.*, vol. 57, no. 52, pp. 17173–17177, 2018, doi: 10.1002/anie.201811570.

[86] L. Han and J. R. Galán-Mascarós, "The positive effect of iron doping in the electrocatalytic activity of cobalt hexacyanoferrate," *Catalysts*, vol. 10, no. 1, pp. 1–7, 2020, doi: 10.3390/catal10010130.

[87] Y. Yamada, K. Oyama, T. Suenobu, and S. Fukuzumi, "Photocatalytic water oxidation by persulphate with a Ca^{2+} ion-incorporated polymeric cobalt cyanide complex affording O_2 with 200% quantum efficiency," *Chem. Commun.*, vol. 53, no. 24, pp. 3418–3421, 2017, doi: 10.1039/c7cc00199a.

[88] E. P. Alsaç, E. Ulker, S. V. K. Nune, and F. Karadas, "A Cyanide-Based Coordination Polymer for Hydrogen Evolution Electrocatalysis," *Catal. Letters*, vol. 148, no. 2, pp. 531–538, 2018, doi: 10.1007/s10562-017-2271-6.

[89] P. Acevedo Peña, D. Ramírez Ortega, D. Guerrero Araque, A. Hernández Gordillo, R. Zanella, and E. Reguera, "Boosting the photocatalytic hydrogen production of TiO_2 by using copper hexacyanocobaltate as co-catalyst," *Int. J. Hydrogen Energy*, vol. 46, no. 17, pp. 10312–10323, 2021, doi: 10.1016/j.ijhydene.2020.12.135.

[90] M. Zhang *et al.*, " Efficient Charge Migration in Chemically-Bonded Prussian Blue Analogue/CdS with Beaded Structure for Photocatalytic H 2 Evolution ," *JACS Au*, vol. 1, no. 2, pp. 212–220, 2021, doi: 10.1021/jacsau.0c00082.

[91] W. Qi *et al.*, "Prussian blue derived Fe_2N for efficiently improving the photocatalytic hydrogen evolution activity of g-C_3N_4 nanosheets," *Catal. Sci. Technol.*, vol. 9, no. 10, pp. 2571–2577, 2019, doi: 10.1039/c9cy00198k.

[92] X. Cao *et al.*, "Ni-doped CdS porous cubes prepared from prussian blue nanoarchitectonics with enhanced photocatalytic hydrogen evolution performance," *Int. J. Hydrogen Energy*, vol. 47, no. 6, pp. 3752–3761, 2022, doi: 10.1016/j.ijhydene.2021.11.016.

[93] E. Mamontova *et al.*, "Fashioning Prussian Blue Nanoparticles by Adsorption of Luminophores: Synthesis, Properties, and in Vitro Imaging," *ACS Inorg. Chem.*, 2020, doi: 10.1021/acs.inorgchem.9b03699.

[94] C. C. Su and S. M. Huang, "The formation of cobalt(II) halide complexes containing neutral bidentate ligands," *Transit. Met. Chem.*, vol. 9, no. 6, pp. 220–224, 1984, doi: 10.1007/BF01227124.

[95] K. Arun Kumar, M. Amuthaselvi, and A. Dayalan, "Cis-Bis(2,2′-bipyridine-K2 N,N′)dichloridocobalt(II) trihydrate," *Acta Crystallogr. Sect. E Struct. Reports Online*, vol. 67, no. 4, pp. 2–8, 2011, doi: 10.1107/S1600536811009251.

[96] I. Kani, Ö. Atlier, and K. Güven, "Mn(II) complexes with bipyridine, phenanthroline and benzoic acid: Biological and catalase-like activity," *J. Chem. Sci.*, vol. 128, no. 4, pp. 523–536, 2016, doi: 10.1007/s12039-016-1050-z.

[97] Q. Wang, N. Wang, S. He, J. Zhao, J. Fang, and W. Shen, "Simple synthesis of Prussian blue analogues in room temperature ionic liquid solution and their catalytic application in epoxidation of styrene," *Dalt. Trans.*, vol. 44, no. 28, pp. 12878–12883, 2015, doi: 10.1039/c5dt01762a.

[98] O. Sato, Y. Einaga, A. Fujishima, and K. Hashimoto, "Photoinduced Long-Range Magnetic Ordering of a Cobalt - Iron Cyanide," *Inorg. Chem.*, vol. 38, no. 12, pp. 4405–

4412, 1999.

[99] A. Bleuzen *et al.*, “Photoinduced ferrimagnetic systems in Prussian blue analogues $C^{(I)}_{(x)}Co_4[Fe(CN)_6]_{(y)}$ ($C^{(i)}$ = alkali cation). 1. Conditions to observe the phenomenon,” *J. Am. Chem. Soc.*, vol. 122, no. 28, pp. 6648–6652, 2000, doi: 10.1021/ja000348u.

[100] D. Li *et al.*, “Magnetic and optical bistability driven by thermally and photoinduced intramolecular electron transfer in a molecular cobalt-iron Prussian blue analogue,” *J. Am. Chem. Soc.*, vol. 130, no. 1, pp. 252–258, 2008, doi: 10.1021/ja0757632.

[101] H. Langhals, R. Ismael, and K. Polborn, “Crystal structure of,” *Zeitschrift fur Krist. - New Cryst. Struct.*, vol. 214, no. 1, pp. 35–37, 1999, doi: 10.1515/ncrs-1999-0122.

[102] C. P. Berlinguette, A. Dragulescu-Andrasi, A. Sieber, H. U. Güdel, C. Achim, and K. R. Dunbar, “A charge-transfer-induced spin transition in a discrete complex: The role of extrinsic factors in stabilising three electronic isomeric forms of a cyanide-bridged Co/Fe cluster,” *J. Am. Chem. Soc.*, vol. 127, no. 18, pp. 6766–6779, 2005, doi: 10.1021/ja043162u.

[103] K. E. Funck, M. G. Hilfiger, C. P. Berlinguette, M. Shatruk, W. Wernsdorfer, and K. R. Dunbar, “Trigonal-bipyramidal metal cyanide complexes: a versatile platform for the systematic assessment of the magnetic properties of prussian blue materials,” *Inorg. Chem.*, vol. 48, no. 8, pp. 3438–3452, 2009, doi: 10.1021/ic801990g.

[104] L. He *et al.*, “Mesoporous Nanostructured CoFe-Se-P Composite Derived from a Prussian Blue Analogue as a Superior Electrocatalyst for Efficient Overall Water Splitting,” *ACS Appl. Energy Mater.*, vol. 1, no. 8, pp. 3915–3928, 2018, doi: 10.1021/acsaem.8b00663.

[105] T. G. U. Ghobadi *et al.*, “Pushing the limits in photosensitizer-catalyst interaction via a short cyanide bridge for water oxidation,” *Cell Reports Phys. Sci.*, vol. 2, no. 2, p. 100319, 2021, doi: 10.1016/j.xcrp.2020.100319.

[106] A. Bencini and V. Lippolis, “1,10-Phenanthroline: A versatile building block for the construction of ligands for various purposes,” *Coord. Chem. Rev.*, vol. 254, no. 17–18, pp. 2096–2180, 2010, doi: 10.1016/j.ccr.2010.04.008.

[107] D. W. Crandell, S. Ghosh, C. P. Berlinguette, and M. H. Baik, “How a $[Co^{IV}\text{-}O]^{2+}$

Fragment Oxidizes Water: Involvement of a Biradicaloid $[Co^{II}\text{-}(\cdot O\cdot)]^{2+}$ Species in Forming the O-O Bond," *ChemSusChem*, vol. 8, no. 5, pp. 844–852, 2015, doi: 10.1002/cssc.201403024.

[108] M. Schilling and S. Luber, "Computational modeling of cobalt-based water oxidation: Current status and future challenges," *Front. Chem.*, vol. 6, no. APR, pp. 1–21, 2018, doi: 10.3389/fchem.2018.00100.

[109] B. M. Pires *et al.*, "Electrochemical water oxidation by cobalt-Prussian blue coordination polymer and theoretical studies of the electronic structure of the active species," *Dalt. Trans.*, vol. 48, no. 15, pp. 4811–4822, 2019, doi: 10.1039/c8dt04660c.

[110] K. Houk, *Orbital Interactions in Chemistry*, vol. 5, no. 8. 1986.

[111] A. Poater, F. Ragone, A. Correa, and L. Cavallo, "Comparison of different ruthenium-alkylidene bonds in the activation step with N-heterocyclic carbene Ru-catalysts for olefins metathesis," *Dalt. Trans.*, vol. 40, no. 42, pp. 11066–11069, 2011, doi: 10.1039/c1dt10959f.

[112] A. Azhar *et al.*, "Single crystal growth of two-dimensional cyano-bridged coordination polymer of $Co(H_2O)_2Ni(CN)_4{\bullet}4H_2O$ using trisodium citrate dihydrate," *Bull. Chem. Soc. Jpn.*, vol. 92, no. 7, pp. 1263–1267, 2019, doi: 10.1246/bcsj.20190054.

[113] D. F. Shriver and D. B. Brown, "The Environment of Interstitial," *Inorg. Chem.*, vol. 8, no. 1, pp. 42–46, 1968.

[114] E. J. Canto-Aguilar, M. A. Oliver-Tolentino, G. Ramos-Sánchez, and I. González, "Effect of the external metal on the electrochemical behavior of $M_3[Co(CN)_6]_2$ (M: Co, Ni, Cu, Zn), towards their use as anodes in potassium ion batteries," *Electrochim. Acta*, vol. 371, p. 137828, 2021, doi: 10.1016/j.electacta.2021.137828.

[115] O. Sato, Y. Einaga, T. Iyoda, A. Fujishima, and K. Hashimoto, "Cation-driven electron transfer involving a spin transition at room temperature in a cobalt iron cyanide thin film," *J. Phys. Chem. B*, vol. 101, no. 20, pp. 20–22, 1997, doi: 10.1021/jp9701451.

[116] O. Sato, T. Iyoda, A. Fujishima, and K. Hashimoto, "Photoinduced magnetization of a cobalt-iron cyanide," *Science (80-.).*, vol. 272, no. 5262, pp. 704–705, 1996, doi:

10.1126/science.272.5262.704.

[117] J. Rodríguez-Hernández, A. A. Lemus-Santana, C. N. Vargas, and E. Reguera, “Three structural modifications in the series of layered solids $T(H_2O)_2[Ni(CN)_4]\cdot xH_2O$ with T = Mn, Co, Ni: Their nature and crystal structures,” *Comptes Rendus Chim.*, vol. 15, no. 4, pp. 350–355, 2012, doi: 10.1016/j.crci.2011.11.004.

[118] Y. L. Qin, B. W. Yang, G. F. Wang, and H. Sun, “A cyanide-bridged heterometallic coordination polymer constructed from square-planar $[Ni(CN)_4]^{2-}$: Synthesis, crystal structure, thermal decomposition, electron paramagnetic resonance (EPR) spectrum and magnetic properties,” *Acta Crystallogr. Sect. C Struct. Chem.*, vol. 72, no. 7, pp. 555–560, 2016, doi: 10.1107/S2053229616009372.

[119] X. Xu, H. Liang, F. Ming, Z. Qi, Y. Xie, and Z. Wang, “Prussian Blue Analogues Derived Penroseite $(Ni,Co)Se_2$ Nanocages Anchored on 3D Graphene Aerogel for Efficient Water Splitting,” *ACS Catal.*, vol. 7, no. 9, pp. 6394–6399, 2017, doi: 10.1021/acscatal.7b02079.

[120] H. J. Niu *et al.*, “Prussian blue analogue-derived CoFe nanocrystals wrapped in nitrogen-doped carbon nanocubes for overall water splitting and Zn-air battery,” *J. Power Sources*, vol. 480, p. 229107, 2020, doi: 10.1016/j.jpowsour.2020.229107.

[121] Kratos Analytics., “Overlapping photoelectron lines and Auger features are a common issue in the analysis of complex materials. The standard approach of switching to an achromatic Mg X-ray source may become undesirable due to the introduction of X-ray satellites into the spe,” *High Energy Monochromatic X-Ray Source for XPS*, 2017. https://www.azom.com/article.aspx?ArticleID=14092 (accessed Apr. 13, 2022).

[122] A. Cano, I. Monroy, M. Ávila, D. Velasco-Arias, J. Rodríguez-Hernández, and E. Reguera, “Relevant electronic interactions related to the coordination chemistry of tetracyanometallates. An XPS study,” *New J. Chem.*, vol. 43, no. 46, pp. 18384–18393, 2019, doi: 10.1039/c9nj04173g.

[123] Thermo Fischer Scientific., “Cobalt X-ray photoelectron spectra, cobalt electron configuration, and other elemental information,” *Cobalt X-ray photoelectron spectra, cobalt electron configuration, and other elemental information*.

https://www.thermofisher.com/tr/en/home/materials-science/learning-center/periodic-table/transition-metal/cobalt.html (accessed Apr. 14, 2022).

[124] X. Chia and M. Pumera, "Characteristics and performance of two-dimensional materials for electrocatalysis," *Nat. Catal.*, vol. 1, no. 12, pp. 909–921, 2018, doi: 10.1038/s41929-018-0181-7.

[125] G. Yanalak, A. Aljabour, E. Aslan, F. Ozel, and I. H. Patir, "A systematic comparative study of the efficient co-catalyst-free photocatalytic hydrogen evolution by transition metal oxide nanofibers," *Int. J. Hydrogen Energy*, vol. 43, no. 36, pp. 17185–17194, 2018, doi: 10.1016/j.ijhydene.2018.07.113.

[126] P. A. Mangrulkar, M. M. Joshi, S. N. Tijare, V. Polshettiwar, N. K. Labhsetwar, and S. S. Rayalu, "Nano cobalt oxides for photocatalytic hydrogen production," *Int. J. Hydrogen Energy*, vol. 37, no. 13, pp. 10462–10466, 2012, doi: 10.1016/j.ijhydene.2012.01.112.

[127] L. Jiang, K. Wang, X. Wu, G. Zhang, and S. Yin, "Amorphous Bimetallic Cobalt Nickel Sulfide Cocatalysts for Significantly Boosting Photocatalytic Hydrogen Evolution Performance of Graphitic Carbon Nitride: Efficient Interfacial Charge Transfer," *ACS Appl. Mater. Interfaces*, vol. 11, no. 30, pp. 26898–26908, 2019, doi: 10.1021/acsami.9b07311.

[128] T. Banerjee, F. Haase, G. Savasci, K. Gottschling, C. Ochsenfeld, and B. V. Lotsch, "Single-Site Photocatalytic H_2 Evolution from Covalent Organic Frameworks with Molecular Cobaloxime Co-Catalysts," *J. Am. Chem. Soc.*, vol. 139, no. 45, pp. 16228–16234, 2017, doi: 10.1021/jacs.7b07489.

[129] P. Wang, T. Wu, C. Wang, J. Hou, J. Qian, and Y. Ao, "Combining Heterojunction Engineering with Surface Cocatalyst Modification to Synergistically Enhance the Photocatalytic Hydrogen Evolution Performance of Cadmium Sulfide Nanorods," *ACS Sustain. Chem. Eng.*, vol. 5, no. 9, pp. 7670–7677, 2017, doi: 10.1021/acssuschemeng.7b01043.

[130] Y. J. Yuan *et al.*, "Construction of a noble-metal-free photocatalytic H_2 evolution system using MoS2/reduced graphene oxide catalyst and zinc porphyrin photosensitizer," *J. Phys.*

Chem. C, vol. 121, no. 39, pp. 24452–24462, 2017, doi: 10.1021/acs.jpcc.7b08290.

[131] Q. Zhang *et al.*, "Highly Efficient Photocatalytic Hydrogen Evolution by ReS_2 via a Two-Electron Catalytic Reaction," *Adv. Mater.*, vol. 30, no. 23, pp. 1–7, 2018, doi: 10.1002/adma.201707123.

[132] X. Zhao *et al.*, "An Efficient, Visible-Light-Driven, Hydrogen Evolution Catalyst NiS/$Zn_xCd_{1-x}S$ Nanocrystal Derived from a Metal–Organic Framework," *Angew. Chemie - Int. Ed.*, vol. 57, no. 31, pp. 9790–9794, 2018, doi: 10.1002/anie.201805425.

[133] K. Gottschling *et al.*, "Rational Design of Covalent Cobaloxime-Covalent Organic Framework Hybrids for Enhanced Photocatalytic Hydrogen Evolution," *J. Am. Chem. Soc.*, vol. 142, no. 28, pp. 12146–12156, 2020, doi: 10.1021/jacs.0c02155.

[134] A. Reynal, E. Pastor, M. A. Gross, S. Selim, E. Reisner, and J. R. Durrant, "Unravelling the pH-dependence of a molecular photocatalytic system for hydrogen production," *Chem. Sci.*, vol. 6, no. 8, pp. 4855–4859, 2015, doi: 10.1039/c5sc01349f.

[135] M. Natali, R. Argazzi, C. Chiorboli, E. Iengo, and F. Scandola, "Photocatalytic hydrogen evolution with a self-assembling reductant-sensitizer-catalyst system," *Chem. - A Eur. J.*, vol. 19, no. 28, pp. 9261–9271, 2013, doi: 10.1002/chem.201300133.

[136] A. Xie, Z. H. Pan, M. Yu, G. G. Luo, and D. Sun, "Photocatalytic hydrogen production from acidic aqueous solution in BODIPY-cobaloxime-ascorbic acid homogeneous system," *Chinese Chem. Lett.*, vol. 30, no. 1, pp. 225–228, 2019, doi: 10.1016/j.cclet.2018.05.003.

[137] M. Razavet, V. Artero, and M. Fontecave, "Proton electroreduction catalyzed by cobaloximes: Functional models for hydrogenases," *Inorg. Chem.*, vol. 44, no. 13, pp. 4786–4795, 2005, doi: 10.1021/ic050167z.

[138] T. Chen *et al.*, "Two anionic Ni(II) porphyrinic metal−organic frameworks: Syntheses, flexibility and roles in visible-light photocatalytic CO_2 reduction to CO in the $Ru(bpy)_3Cl_2$/TEA/CH_3CN system," *J. Solid State Chem.*, vol. 287, p. 121340, 2020, doi: 10.1016/j.jssc.2020.121340.

[139] L. Tian, J. L. Zhu, L. Chen, B. An, Q. Q. Liu, and K. L. Huang, "Synthesis and

characterization of α-cobalt hydroxide nanobelts," *J. Nanoparticle Res.*, vol. 13, no. 8, pp. 3483–3488, 2011, doi: 10.1007/s11051-011-0269-3.

[140] S. Niu, S. Li, Y. Du, X. Han, and P. Xu, "How to Reliably Report the Overpotential of an Electrocatalyst," *ACS Energy Lett.*, vol. 5, no. 4, pp. 1083–1087, 2020, doi: 10.1021/acsenergylett.0c00321.

CHAPTER 7.

7.0 APPENDIX

7.1 Turn Over Frequency (TOF) Calculations

7.1.1 Lower bound TOF (TOF_{lb})

The TOF_{lb} was calculated by assuming that **all the cobalt sites** in the compounds are active in catalysis. The method of the calculation is given below:

10 mg of catalyst was used, therefore:

$$mass\ of\ Co\ in\ catalyst = \%\ mass\ of\ Co\ in\ catalyst \times 10\ mg$$

(eq. S1)

$$moles\ of\ Co\ in\ catalyst = \frac{mass\ of\ Co\ in\ catalyst}{molecular\ weight\ of\ Co}$$

(eq. S2)

After determining the moles of cobalt present in the catalyst, the TOF and TON were calculated as follows:

$$Turn\ over\ number(TON) = \frac{moles\ of\ O_2/H_2\ evolved\ from\ photocatalysis}{moles\ of\ cobalt\ in\ catalyst}$$

(eq. S3)

$$TOF = \frac{TON}{reaction\ time}$$

(eq. S4)

7.1.2 Upper bound TOF (TOF_{ub})

The TOF_{ub} was calculated by assuming that **only the surface cobalt sites** in the compounds are active in catalysis. The method of the calculation is given below:

First, the surface concentration (Γ) of active cobalt sites is from the electrochemical linear dependence between the peak current (I) of the Co^{3+}/Co^{2+} reduction wave and the scan rate (ν).[68]

Then, the surface concentration of cobalt sites in 10 mg catalyst was obtained using the relation below:

$$= \frac{surface\ concentation\ (nmol/cm^2)\ \times catalyst\ eletrode\ area\ (cm^2)}{catalyst\ mass\ loading\ on\ electrode\ surface\ (mg)} \times 10\ mg$$

(eq. S5)

$$Turn\ over\ number(TON) = \frac{moles\ of\ O_2/H_2\ evolved\ from\ photocatalysis}{cobalt\ surface\ concetration\ in\ 10\ mg\ catalyst\ (nmol)}$$

(eq. S6)

The TOF was calculated using the same expression as eq. S4.